EXPERIMENTAL AND ANALYTICAL STRATEGIES TO ASSESS THE

SEISMIC PERFORMANCE OF AUXILIARY POWER SYSTEMS IN

CRITICAL INFRASTRUCTURE

EXPERIMENTAL AND ANALYTICAL STRATEGIES TO ASSESS THE

SEISMIC PERFORMANCE OF AUXILIARY POWER SYSTEMS IN

CRITICAL INFRASTRUCTURE

By AHMED GHITH, B.Sc., M.Sc.

A Thesis Submitted to the School of Graduate Studies in Partial Fulfilment of the

Requirements for the Degree Doctor of Philosophy

McMaster University
© Copyright by Ahmed Ghith
April 2020

McMaster University Doctor of Philosophy (2020) Hamilton, Ontario

TITLE: Experimental and analytical strategies to assess the seismic performance of axillary power systems in critical infrastructure

AUTHOR: Ahmed Ghith, B.Sc., M.Sc. (Cairo University)

SUPERVISOR: Drs. Michael J. Tait and Wael El-Dakhakhni

PAGES: xvi, 186

Abstract

The performance of nonstructural components in critical infrastructure, such as nuclear power plants (NPPs), has been primarily based on experience and historical data. This topic has been attracting increased interest from researchers following the Fukushima Daiichi nuclear disaster in 2011. This disaster demonstrated the importance of using batteries in NPPs as an auxiliary power system, where such systems can provide the necessary power to mitigate the risk of serious accidents. However, little research has been conducted on such nonstructural components to evaluate their performance following the post-Fukushima safety requirements, recommended by several nuclear regulators worldwide [e.g., Nuclear Regulatory Commission (NRC), and Nuclear Safety Commission (NSC)]. To address this research gap, this dissertation investigates the lateral performance of an auxiliary battery power system (ABPS) similar to those currently existing/operational in NPPs in Canada. The ABPS was experimentally tested under displacement-controlled quasi-static cyclic fully-reversed loading that simulates lateral seismic demands. Due to the presence of sliding batteries, the ABPS was then tested dynamically under increased ground motion levels on a shake table. The experimental results demonstrated that the design guidelines and fragility curves currently assigned to battery rack systems in the FEMA P58 pre-standards do not encompass all possible failure mechanisms.

A 3D numerical model was also developed using OpenSees software. The model was validated using the experimental results. The model results showed that

the lateral performance of ABPS with different configurations (i.e. different lengths, tiers, and seismic categories) is influenced by the capacity of the L-shaped connection between the side rails and the end rail. However, the model was not able to predict all the damage states from the dynamic experimental tests, since the rocking/sliding/impact behavior of the batteries is a highly complex nonlinear problem by nature and beyond the scope of this study. The model presented is limited to the assessment of the lateral performance of different ABPS statically.

This dissertation demonstrated the difference between the observed behavior of laboratory-controlled lateral performance tests of ABPSs operational/existing in NPPs and the behavior of ABPSs found in the literature that relied on limited historical and experience data. Finally, this dissertation laid the foundations for the need to further investigate the behavior of other safety-related components in NPPs and assess their compliance with new post-Fukushima design requirements.

Dedication

to the A Family

Acknowledgment

In the name of Allah the most merciful and the most compassionate

First, I would like to express my deepest gratitude to Amira, Alma, and Adam (the A Family) for always being there for me, and for your support and love throughout the years. You have always been my anchor and the main pillar in my life that I know I could rely on through this journey. You have been there for me during the best times, and during the toughest, darkest times. I just hope that Allah will help to repay some of this dept.

I would also like to express my deep appreciation to my supervisors Drs. Wael El-Dakhakhni and Michael Tait. I will be forever grateful for your support, advice, and mentorship through the years. I would like to thank you for helping me to be a better version of myself, and for shaping the person I will be for the rest of my life.

I would also like to extend my appreciation to my committee members Drs. John Luxat, Mohamed Ezzeldin, and Dimitrios Konstantinidis. I want to thank you for all your time, effort, and advice through every meeting, and every step of this journey.

The experimental work would have not been possible without the help of Kent Wheeler and Paul Heerema. I know I can't thank you enough for every advice you gave me, and how to solve the experimental puzzle.

I would also like to thank all my friends who helped me through both the academic and non-academic life. I would like to give special thanks to Ahmed Elsayed, Yasser El-Anany, Mohamed Yasser, Omar Nasser, Ahmed Yossri, Maysara Gheith, Ahmed Yassin, Mohamed Elsefy, Shady Salem, Tarek Elhashimy. If it weren't for you, I would have not come out of this journey.

Finally, there are no words that could describe my sincere gratitude to my parents Hatem and Hanan. Everything I do in my life is the result of their love and guidance, and I would dedicate all that I have done, and all that I will do to them. Their selfless love is and will always be the main pillar while overcoming whatever life has to offer.

Co-Authorship

This thesis has been prepared in accordance with the regulations for a sandwich thesis format or as a compilation of research papers stipulated by the faculty of graduate studies at McMaster University. This research presents experimental and analytical work carried out solely by Ahmed Ghith. Advice and guidance were provided for the whole thesis by the academic supervisors Dr. Wael El-Dakhakhni and Dr. Michael Tait. Dr. Mohamed Ezzeldin provided comments and edits to papers reported in Chapter 2 and Chapter 3. Information presented from outside sources, which has been used towards analysis or discussion, has been cited where appropriate; all other materials are the sole work of the author. This thesis consists of the following manuscripts in the following chapters:

Chapter 2

Ghith, A., Ezzeldin, M., Tait, M., and El-Dakhakhni W. (2019). "Performance of Battery Rack Auxiliary Power Systems under FEMA 461 Quasi-Static Seismic Loading Protocol." Accepted for publication in Structures, April 2020.

Chapter 3

Ghith, A., Ezzeldin, M., Tait, M., and El-Dakhakhni, W. (2019). "Shake Table Seismic Performance Assessment of Auxiliary Battery Power Systems using the FEMA 461 Protocol." Journal of Structural Engineering, 145(8), 04019080.

Chapter 4

Ghith, A., Tait, M., and El-Dakhakhni, W. (2019). "Opensees Modeling of ABPS." to be submitted.

TABLE OF CONTENTS

List of Figures

List of Tables

<div align="center">

CHAPTER 1

1. INTRODUCTION

</div>

1.1. BACKGROUND AND MOTIVATION

Auxiliary Battery Power Systems (ABPSs) are a reliable backup power solution. For example, ABPS is used in hospitals to avoid fatal consequences after the loss of power (Zhitkov et al. 2000). ABPS can also be coupled with emergency diesel generators to prevent the loss of offsite power in Nuclear Power Plants (NPPs) (NAIIC 2011). As such, ensuring that the ABPS remains functional during and after major earthquakes is critically important, as the failure of the ABPS has a direct contribution to the failure of the NPP in terms of increasing the Core Damage Frequency (CDF) (Choun et al. 2004).

The importance of the ABPS was highlighted during the Fukushima Daiichi nuclear accident. The NPP was hit by an earthquake of magnitude 9.0 followed by a tsunami one hour later. The earthquake triggered the safe shut down sequence as designed, followed by an interruption in the offsite power supply. Consequently, the emergency diesel generators started to supply power to the NPP, however, the tsunami flooded the basement of the NPP. Only the ABPS in the basement of Unit 3 remained unflooded due to its higher elevation. This ABPS was used to supply power to the entire NPP for 8 hours until it finally ran out of power and the meltdown of the working units of the NPP started (Tepco Inc. 2011).

Following the disaster, the Japanese government formed an independent committee to investigate the Fukushima Daiichi nuclear accident. This committee reported that the recorded accelerations of the earthquake were within design limits of the NPP (NAIIC 2011), except for Units 2, 3, and 5 where the recorded accelerations were found to be higher than the design limits by 30% in the period range 0.2 to 0.3 sec. Moreover, the tsunami was reported to be within the updated guidelines of the International Atomic Energy Agency (IEAE). However, neither the owner (i.e., Tepco inc.) nor the regulators ensured the compliance of the seawall height with the updated IEAE guidelines and recommendations. This was mainly attributed to the myth of *complete safety* adopted by Japan (Nöggerath et al. 2011).

Consequently, major regulators worldwide (e.g., the Nuclear Regulatory Commission (NRC) in the United States and the Nuclear Safety Commission (NSC) in Canada) declared that all NPPs should be reassessed following the Beyond Design Basis Events (BDBE) design requirements. BDBE is a new design methodology to ensure the existence of a safety margin between the NPP and the safety-related components, and the Design Basis Event (DBE).

As such, the possible failure modes of the ABPS need to be accurately described, and the corresponding demands need to be carefully assessed. However, Fujisaki et al. (2014) have shown that independent experimental testing to assess the seismic performance of these ABPS is limited as relevant standards (Telcordia Technologies 2002; IEEE 2005, 2013) indicated that the design earthquake levels of these systems are assessed by individual manufacturers. The first study published

on the failure of the ABPS was by Johnson et al. (1999). The previous authors presented fragility data for different ABPS found in NPPs with different installation conditions, using data from a historical database called SQUG (1999). The authors used a binary system to evaluate the failure of different ABPS based on different installation requirements, neglecting different damage states. Afterward, Porter (2009) updated these fragility curves by adding additional data from the Generic Equipment Ruggedness Spectra (GERS) database (EPRI 1991). The previous authors presented fragility curves for good and deficient installation conditions, neglecting different poor installation conditions unlike Johnson et al. (1999). Neither study described the different damage states nor assess the corresponding demands. In addition, these studies relied on limited historical and experimental data.

Other studies have been performed on NPP safety-related nonstructural components. For example, (Lin et al., 2012; Kim et al., 2012; Lai et al., 2013) studied the performance of electrical cabinets and developed the in-cabinet response spectra to be used in the design procedure of in-cabinet components (i.e. relays). Additional studies have been performed on cable tray systems such as (Choun et al., 2008; Huang et al., 2017) to assess possible failure modes and their corresponding demands through fragility curve analysis. Moreover, Huang, et al. (2017) have shown that the amplification factor (also known as resonance factor) is underestimated in the design code (ASCE, 2016).

Similar nonstructural components used for different purposes in other facilities, such as steel storage racks, have been also extensively assessed. For example, Hancock (1985) studied the steel storage rack column behavior and possible torsional buckling subjected to lateral loading. Other studies (Aguirre 2005; Gusella et al. 2018) used experimental tests to describe the beam-column connections, while Gusella et al. (2019) used modeling techniques. Krawinkler (1978) investigated the lateral behavior of the steel storage racks using cyclic load testing protocols, whereas Chen et al. (1980) used shake table dynamic testing. Further studies by Filiatrault et al. (2006) developed a design methodology for steel storage racks to be used as part of the performance-based seismic design approach. In addition, Filiatrault et al. (2008) studied the enhancement of the lateral behavior of steel storage racks using base isolation techniques through the reduction in the life endangerment by falling of content. However, industrial steel storage racks and ABPS used in NPPs have different configurations, dimensions, and material properties, moreover, steel storage racks and ABPS are designed for different earthquake levels. As such, studies on steel storage racks cannot be implemented for ABPS. Hence, there is a need to experimentally investigate modern ABPS used in NPPs in a laboratory-controlled environment.

Moreover, due to the existence of a wide variety of ABPS, numerical simulation presents a reliable alternative as long as the model is robust and compares well with experimental data. To the best of the author's knowledge, the work by Berak and Marconi (2005) is the only published study describing the

development of a numerical model of an ABPS used in telecommunication application that is validated through experimental testing. However, ABPSs used in different critical infrastructure have different configurations, dimensions, and material properties, thus the numerical model by Berak and Marconi (2005) cannot be expanded to account for ABPS used in NPPs.

1.2. RESEARCH OBJECTIVES AND IMPETUS

The main scope of this dissertation is to examine the failure behavior of ABPS operational/existing in NPPs through the investigation of the possible different damage states and the corresponding demand levels. The results of this dissertation also highlight the difference between the failure performance of ABPS presented in the literature that relies on outdated historical data and experience, and the damage states observed from laboratory-controlled tests of modern rack systems. In order to achieve this scope intermediate objectives were adopted:

- Experimental investigation of the ABPS to examine the lateral behavior and connection behavior

- Experimental investigation of possible damage states of the ABPS and their corresponding demands.

- Development of a nonlinear finite element model for the ABPS that is validated using experimental results.

- Investigation of other ABPSs by the same manufacturer.

The evaluation of the hysteretic response of ABPS under quasi-static controlled testing showed that the use of serrated strut nuts affected the lateral performance of the ABPS. Moreover, the test results showed that the capacity of the ABPS is limited by the behavior of the L-shaped connection between the end rail and the side rails. Dynamic shake table testing was also performed in order to observe the behavior of the sliding batteries. Dynamic test results have shown the need to further update fragility curves found in the literature to account for new damage states produced by the use of advanced assembly techniques. The experimental results were used to validate a 3D detailed OpenSees model (McKenna 2016) for the ABPS. The numerical model showed that the capacity of different configurations of the ABPS with different seismic categories, by the addition of extra braces, is delimited by the consistent use of the L-shaped connection. Finally, this dissertation demonstrated the difference between the observed behavior of laboratory-controlled lateral performance tests of ABPSs operational/existing in NPPs and the behavior of ABPS found in literature that relied on limited historical and experience data. Hence, similar laboratory-controlled tests should be performed to assess the behavior of other safety related components in NPPs.

1.3. ORGANIZATION OF THE DISSERTATION

The dissertation was written in a sandwich thesis format consisting of three journal articles. As such, every chapter consists of a self-contained introduction and

literature review. As a result, some overlap exists between different chapters, particularly in the introduction, literature review, and experimental results. The dissertation is comprised of five chapters:

- Chapter 1 presents the motivational research gap and objectives of the dissertation as well as background information on ABPS in NPPs.

- Chapter 2 presents the quasi-static experimental program, rack configuration, test setup, and loading protocol. The cyclic behavior of the rack was analyzed in terms of the overall and component deformations, as well as member strains. A mechanistic model calibrated using the experimental data was presented which aims to highlight the need to account for assembly techniques in new relevant design codes.

- Chapter 3 presents the shake table experimental program, rack configuration, test setup, and loading protocol. An extensive discussion was presented to investigate the shake table test results and define possible dynamic damage states and their corresponding demands. These results were then utilized to develop fragility curves to highlight the difference between the laboratory tested data and the fragility curves found in the literature.

- Chapter 4 focuses on the development of a finite element model for the ABPS using the OpenSees platform. The numerical model was validated using the experimental results from both the shake table and the quasi-static

tests. Limitations of the model are described. The lateral performance of other configurations of ABPS provided by the same manufacturer is investigated.

- Chapter 5 presents the dissertation summary, major contribution, and recommendations for future work.

1.4. REFERENCES

Aguirre, C. (2005). Seismic behavior of rack structures. Journal of Constructional Steel Research, 61(5), 607-624.

ASCE. 2010. Seismic design loads for buildings and other structures. ASCE/SEI 7. Reston, VA: ASCE.

Berak, Elzbieta G., and Marconi Communications. 2005. "Modal testing and finite element analysis of a battery rack for seismic applications." Journal of the IEST 48 (1).

Chen, C. K., Scholl, R. E., & Blume, J. A. (1980). Earthquake simulation tests of industrial steel storage racks. In Proceedings of the Seventh World Conference on Earthquake Engineering, Istanbul, Turkey (pp. 379-386).

Choun, Young-Sun, In-Kil Choi, and Jeong-Moon Seo. 2004. "Improvement of seismic safety of nuclear power plants by increase of equipment seismic capacity." 13th world conference on earthquake engineering. Vancouver, B.C., Canada.

Choun Young-Sun, Choi In-Kil and Seo Jeong-Moon (2088). Improvement of the seismic safety of existing nuclear power plants by an increase of the component seismic capacity: A case study. Nuclear Engineering and Design. - 6: Vol. 238. - pp. 1410- 1420.

EPRI. 1991. Generic Seismic Ruggedness of Power Plant Equipment. Oakland, CA: Electric Power Research Institute (EPRI) NP-5223-SL Revision 1.

Filiatrault, A., Bachman, R. E., & Mahoney, M. G. (2006). Performance-based seismic design of pallet-type steel storage racks. Earthquake Spectra, 22(1), 47-64.

Filiatrault, A., Higgins, P. S., Wanitkorkul, A., Courtwright, J. A., & Michael, R. (2008). Experimental seismic response of base isolated pallet-type steel storage racks. Earthquake Spectra, 24(3), 617-639.

Fujisaki, E., S. Takhirov, Q. Xie, and K. Mosalam. (2014). "Seismic vulnerability of power supply: Lessons learned from recent earthquakes and future horizons of research." In Proc., 9th Int. Conf. of Structural Dynamics. Porto, Portugal: European Association for Structural Dynamics, Univ. of Porto.

Gusella, F., Lavacchini, G., & Orlando, M. (2018). Monotonic and cyclic tests on beam-column joints of industrial pallet racks. Journal of Constructional Steel Research, 140, 92-107.

Gusella, F., Orlando, M., & Spinelli, P. (2019). Pinching in steel rack joints: numerical modeling and effects on structural response. International Journal of Steel Structures, 19(1), 131-146.

Hancock, G. J. (1985). Distortional buckling of steel storage rack columns. Journal of Structural Engineering, 111(12), 2770-2783.

Huang, B., W. Lu, and K. M. Mosalam. 2017. "Shaking table tests of the cable tray system in nuclear power plants." J. Perform. Constr. Facil. 31 (4): 04017018. https://doi.org/10.1061/(ASCE)CF.1943-5509 .0001009.

IEEE. (2005). IEEE recommended practice for seismic design of substations. IEEE 693. New York: IEEE.

IEEE. (2013). IEEE standard for qualification of Class 1E vented lead acid storage batteries for nuclear power generating stations. IEEE 535. New York: IEEE.

Johnson, Gayle S., Robert E. Sheppard, Marc D. Quilici, Stephen J. Eder, and Charles R. Scawthorn. 1999. *Seismic reliability assessment of critical facilities: a handbook, supporting documentation, and model code provisions.* Technical Report MCEER-99-0008, Oakland, California: MCEER.

Kim Min Kyu, Choi In-Kil and Seo Jeong-Moon (2012). A shaking table test for an evaluation of seismic behavior of 480 V MCC. Nuclear Engineering and Design. pp. 341-355.

Krawinkler, H. (1978). Experimental study on seismic behavior of industrial storage racks. International Specialty Conference on Cold-Formed Steel Structures.

Lai, Z.-Y., J.-F. Chai, F.-R. Lin, M.-Y. Chen, and P.-F. Chou. (2013). "Experimental Study for MCCs in Taiwan Lungmen Nuclear Power Plant."

In Proceedings of 22nd International Conference on Structural Mechanics in Reactor Technology, San Francisco, CA, 18–23 August 2013: vol: 4: 2840–2849. Raleigh, NC: IASMiRT.

Lin, F. R., Chai, J. F., Lai, Z. Y, Chang, K. C., Liao, W. I., Chou, L. P. and Huang, C. C., (2012), Experimental Study of Seismic Qualification of In-cabinet Equipment in NPP, Transaction of 15th World Conference on Earthquake Engineering.

McKenna, F. F. (2016). Open System for Earthquake Engineering Simulation. Version 2.5.0. University of California, Berkeley, CA,2000. Retrieved from http://opensees.berkeley.edu.

NAIIC, The Fukushima Nuclear Accident Independent Investigation Commission. 2011. The National Diet of Japan.

Nöggerath, Johannis, Robert J. Geller, and Viacheslav K. Gusiakov. 2011. "Fukushima: The myth of safety, the reality of geoscience." *Bulletin of the Atomic Scientists* 67 (5): 37-46.

Porter, Keith. 2009. *Fragility of Battery Racks.* Washington, D.C.: Federal Emergency Management Agency (FEMA) FEMA P-58 /BD-3.9.26.

SQUG. 1999. *Electronic Earthquake Experience Database User's Guide: eSQUG EPRIWEB Site.* Palo Alto, CA: EPRI, TR-113705.

Telcordia Technologies. 2002. Network equipment-building system (NEBS) requirements: Physical protection. Specification GR-63-CORE. Bridgewater, NJ: Telcordia Technologies.

Tepco Inc. (2011). "Fukushima Nuclear Accident Analysis Report." Interim Report, Tokyo.

Zhitkov, O.M., A.G. Garganev, and A.G. Azarov. 2000. "Application of the uninterruptible power supply systems in medicine." *Modern Technique and Technologies* 216-217.

CHAPTER 2

2. PERFORMANCE OF BATTERY RACK AUXILIARY POWER SYSTEMS UNDER FEMA 461 QUASI-STATIC SEISMIC LOADING PROTOCOL

2.1. ABSTRACT

The performance of nonstructural components in nuclear power plants (NPPs), which is primarily based on experience and historical data, has been attracting increased interest from researchers following the Fukushima Daiichi nuclear disaster in 2011. This disaster demonstrated the importance of using batteries in NPPs as an auxiliary power system, where such systems can provide the necessary power to mitigate the risk of serious accidents. However, little research has been conducted on such nonstructural components (e.g., auxiliary battery power systems) to evaluate their performance following the post-Fukushima safety requirements, recommended by several nuclear regulators worldwide [e.g., Nuclear Regulatory Commission (NRC), and Nuclear Safety Commission (NSC)]. To address this research gap, the current study investigates the lateral performance of an auxiliary battery power system similar to those currently existing/operational in NPPs in Canada. The rack system was experimentally tested under displacement-controlled quasi-static cyclic fully-reversed loading that simulates lateral seismic demands, following the FEMA 461 guidelines "Interim testing protocol for determining the seismic performance

characteristics of structural and nonstructural components". Following a brief summary of the experimental program, the test results are presented in terms of the rack hysteretic response, damage sequence, stiffness degradation, ductility capacity, member strains, and local deformations. Subsequently, a simplified mechanistic model and a concentrated plasticity model in OpenSees have been developed and calibrated using the experimental results. The experimental and modeling results show that without detailed modeling of the rack system connections (i.e., L-shaped connection and sliding nuts), incorrect performance prediction of such systems may result. The findings of the current study can be utilized, within the next generation of performance-based seismic design approaches, to enhance the robustness and improve the reliability of damage state predictions of auxiliary battery power systems in critical facilities.

2.2. INTRODUCTION

Auxiliary Battery Power Systems (ABPS) together with emergency diesel generators are key risk mitigation strategies necessary to ensure the safety and resilience of the Nuclear Power Plants (NPPs) after the failure of their offsite power supply (NAIIC, 2011). As such, failure of ABPS significantly contributes to the overall failure probability of NPPs within fault and event tree analyses, including NPPs (Choun, et al., 2004), and subsequently, they are required to remain functional during and after extreme events (e.g. earthquakes).

The importance of ABPS in NPPs was demonstrated during the Fukushima Daiichi nuclear disaster in 2011. During this disaster, an earthquake of magnitude 9.0 occurred off the coast of Tōhoku, Japan. Although the largest ever recorded in Japan, most of the accelerations recorded at the Fukushima Daiichi site were still within the design limits of the NPP, with the exception of the accelerations recorded in the basement of 3 out of 6 units (i.e., units 2, 3 and 5), which were reported to be higher than the design limits in the period range 0.2 to 0.3 sec by approximately 30% (Hirano, et al., 2012; Wang, et al., 2013). As such, the earthquake triggered the planned safe shutdown sequence. Moreover, the earthquake caused an outage in the offsite power supply to the NPP (i.e., common cause failure) and subsequently prompted the operation of the auxiliary power systems as designed. Approximately one hour later, however, a tsunami, with waves as high as 15 m (Tepco Inc., 2011), reached the NPP causing flooding in the basement of the reactor building. This basement contained all the auxiliary power systems, including the emergency diesel generators and the ABPS. Later on, only ABPS in Unit 3 of the NPP remained unflooded due to their location at a higher elevation, without any clear description of the earthquake-induced damage. As such, this ABPS was able to maintain power to all working units for eight hours before a meltdown eventually started (Tepco Inc., 2011).

Consecutively, the Nuclear Accident Independent Investigation Commission (NAIIC) appointed by the National Diet of Japan (2011) reported that "*NAIIC has verified that at the time the Great East Japan Earthquake occurred,*

15

the structure of the Fukushima Daiichi Nuclear Power Plant was not capable of withstanding the effects of the earthquake or the tsunami. Nor was the nuclear power plant prepared to respond to a severe accident. In spite of the fact that Tokyo Electric Power Company (TEPCO) and the regulators were aware of the risk from such natural disasters, neither had taken steps to put preventive measures in place. This was the fundamental reason for the accident; it could have been prevented if these matters had been attended to appropriately."

This finding was mainly related to the oversight of the Japanese regulators and Tepco Inc. to International Atomic Energy Agency (IAEA) guidelines and recommendations regarding the risks associated with possible earthquakes and resulting tsunamis (Funabashi, et al., 2012), and the design concepts based on experience and outdated historical data were more favorable (Funabashi, et al., 2012). More specifically, the effects of an earthquake, within the NPP design limits, followed by a tsunami, might have been prevented if proper risk mitigation strategies (e.g. updated earthquake predictions and increasing the seawall height) were adopted as initially recommended by the IAEA (NAIIC, 2011). Such multi-hazard environment demonstrated that relying on experience and outdated design concepts and data can eventually lead to catastrophic consequences (Funabashi, et al., 2012). To address this issue, most regulators (e.g. the Nuclear Regulatory Commission (NRC) in the United States and the Nuclear Safety Commission (NSC) in Canada) required Beyond-Design-Basis-Events (BDBE) analysis. In part, this type of analysis ensures that safety-related components in NPPs (e.g.

ABPS) have sufficient safety margins between the event causing their failure and the Design-Basis-Events (DBE).

To facilitate the adoption of the BDBE analysis concept, there is a pressing need to quantify the performance of key safety-related equipment under extreme events and associated possible failure modes. For example, researchers have studied the performance of electrical cabinets and determined their failure modes and in-cabinet components (i.e., relays) design limits (Lin, et al., 2012; Kim, et al., 2012; Lai, et al., 2013). Additional research was conducted, which involved the investigation of cable tray systems using fragility curves analysis to quantify possible failure modes, and later on, promote the adoption of the BDBE design guidelines (Choun, et al., 2008; Huang, et al., 2017). Focusing on ABPS, initially, Johnson, et al. (1999) investigated the failure of ABPS used in NPPs through a fragility analysis. The same authors provided a failure dataset based on different in-situ conditions (e.g., anchoring, battery spacers, and longitudinal braces). Subsequently, Porter (2009) evaluated the failure of ABPS as part of the ATC58 project included in the background documents of the FEMA P-58 (2012). In this project, collapse fragility curves of ABPS, based on rack conditions (i.e., well or deficient installation), were presented.

Failure of ABPS can have a significant impact on the probability of failure of the NPP in terms of the Core Damage Frequency (CDF), Choun et al. (2008) has shown that failure of ABPS has 9% contribution to overall CDF, and as such, relying on outdated historical (SQUG, 1999) and experience-based data (EPRI,

1991), requires further exploration prior to being adopted in the BDBE design requirements. Several researchers (Sato, et al., 2011; Cosenza, et al., 2015; Huang, et al., 2017) have indicated that some nonstructural components should not be evaluated based on experience or historical data due to the use of new configurations. For example, Huang, et al., (2017) presented the failure modes of cable tray systems under shake table testing and demonstrated that current relevant standards [i.e., ASCE 7-16 (2016)] clearly underestimate the component amplification factor (i.e., also known as resonance factor), which accounts for response amplification of attached nonstructural components, thus resulting in lower spectral demand, and eventually leading to unsafe design limits.

The lateral behavior of steel storage racks has been extensively studied. For example, Hancock (1985) studied experimentally and numerically the behavior of steel storage rack columns when subjected to uniform compression stresses in order to investigate the possible distortional buckling behavior. Other studies have been performed to assess the beam-column connections using experimental tests (e.g., Aguirre, 2005; Gusella, et al., 2018) and different modeling techniques (e.g., Gusella, et al., 2019). Research has also been carried out to investigate the overall lateral behavior of steel storage racks under quasi-static cyclic (e.g., Krawinkler, 1978) and shake table dynamic (e.g., Chen, et al., 1980) tests. Other researchers, for example Yin et al. (2018) investigated the overall response of different steel storage racks with spine bracings using speed-lock bolts. Further studies by Filiatrault et al. (2006) have investigated the development of a design procedure to

assess the performance of steel storage racks as part of the performance-based seismic design approach. While additional studies (e.g., Filiatrault, et al., 2008) have investigated the use of a base isolation system for steel storage racks to reduce the life endangerment by falling of content. However, since ABPS and other steel storage racks have different design configurations, results from these steel storage racks studies cannot be implemented for ABPS and further experimental research studies on the ABPS are still needed. Specifically, the ABPS is comprised of continuous horizontal beams connected to the columns and the end rails using sliding nuts and L-shaped connections, while the aforementioned steel storage racks are comprised of single span beams welded to connectors in order to facilitate their connections with perforated vertical columns. Although, ABPS use solid sections, while steel storage racks use perforated sections, both systems use C-channeled cross sections for the columns, which are prone to warping and torsional deformations. Warping and torsional behavior of the columns of steel storage racks have been studied in literature. For example, Bernuzzi et al. (2014) studied the effect of warping induced stresses on the lateral capacity of steel storage rack columns. Further studies have been performed by Bernuzzi et al. (2017) to investigate the effect of warping on the lateral capacity of loaded steel storage racks using pushover analyses. Recently, Bernuzzi et al. (2015a; 2015b) proposed new design approaches for steel storage racks to account for the warping influence of the columns.

Due to the existence of a wide variety of ABPS that are being used for various applications as mentioned earlier, research is still needed to evaluate the performance of these systems with different configurations. For this reason, Ghith et al. (2019) subjected an ABPS (i.e., three tiers and one step) to a progressively increasing loading intensity applied by a shake table and fragility tests were developed based on the experimental results at different damage states. However, experimentally investigating every ABPS is unrealistic as it is typically a time consuming and expensive performance assessment approach. As such, analytical models of nonstructural components in NPPs present a relatively inexpensive alternative, compared to experimental tests, that can be used to assess the performance of these components under various loading conditions. Although several models were developed in previous studies for other components, including electrical cabinets and in-cabinet response spectra (e.g. (Gupta, et al., 2002; Rustogi, et al., 2004; Cho, et al., 2011; Koo, et al., 2010), few similar studies have been conducted on ABPS. To the best of the authors' knowledge, Berak and Marconi Communications, (2005) is the only publicly available study that reported an experimentally validated numerical model for ABPS used in telecommunication applications. The same authors presented a numerical finite element model that was validated using experimental static pull and sine sweep tests. This finite element model could be used in evaluating the modal properties of ABPS used in telecommunication applications. Ensuring that the natural frequency of the ABPS is higher than 6 Hz is accepted to claim that such ABPS used in telecommunication

applications could withstand NEBS (2002) Zone 4 earthquake (i.e. telecommunication standard) without structural or functional damage (Berak, et al., 2005). However, no research has been done to develop an experimentally validated model to simulate ABPS for nuclear applications. Moreover, ABPS used in different industrial applications have different configurations and different design limits. As such, the numerical model presented by Berak (2005) can not be extended to ABPS used in nuclear applications.

The main objective of the current study is to present the experimental results of an ABPS similar to those installed in several existing/operational electrical substations and NPPs in Canada. Although one configuration of ABPSs was recently tested under shaking table dynamic testing protocol (Ghith, et al., 2019) as discussed earlier, the current study evaluates the behavior of a different configuration of ABPSs (i.e., two tiers and one step) under a displacement-controlled quasi-static fully-reversed cyclic loading protocol. The study first presents a description of the test setup and instrumentation, and also provides information about the loading protocol used, following the FEMA 461 guidelines "*Interim testing protocol for determining the seismic performance characteristics of structural and nonstructural components*". The results are presented in terms of the ABPS hysteretic response, damage sequence, stiffness degradation, and ductility capacity. The effects of using the unsymmetrical bracing system are investigated in terms of member strains and 3D behavior of the ABPS. Subsequently, a mechanistic model of the ABPS system, based on stiffness matrix

formulation, is developed and validated using the experimental results. Following the mechanistic model development and validation, the current study further develops a concentrated plasticity (spring) model in OpenSees to simulate the hysteretic response of ABPS. Finally, the experimental and numerical hysteretic responses are compared in terms of the most relevant characteristics, including the initial stiffness, peak load, and pinching behavior at different drift levels.

2.3. EXPERIMENTAL PROGRAM

2.3.1. ABPS Configuration

The experimental investigation was performed on an ABPS [more information on the tested ABPS (RDB type) can be found at (C&D Technologies, 2012)] in a quasi-static manner in the longitudinal direction, considering the typical back-to-back installation condition used in similar studies (Johnson, et al., 1999; Porter, 2009), as shown in Fig. 2.1. This ABPS type can also accommodate different types of batteries, supplied by the same manufacturer, that are currently used in a wide range of applications (e.g. telecommunication and oil & coal industries), including NPPs (C&D Technologies, 2012). The supplied rack is designed according to seismic design requirements of UBC (1994) with peak ground acceleration of 0.45g. According to UBC (1994), nonstructural components are designed to remain elastic (i.e., $R_w = 1$).

The manufacturer offers several seismically qualified ABPS. Using the same steel frame, performance upgradability from one ABPS class to another is

carried out through the installation of additional longitudinal bracing elements (C&D Technologies, 2012). In the current study, the selected ABPS was the EP1 class with two-tier (levels) and a single step battery housing configuration, as shown in Fig. 2.1. The columns and beams of the ABPS were constructed of different sizes of C-channel cross-sections, with dimensions of 76.2x50.8x76.2x3.3 mm (3x2x3x0.13 in) and 41.6x41.6x2.54 mm (1.64x1.64x0.1 in), respectively, whereas the braces were rectangular in cross-section with dimensions of 38.1x5.08 mm (1.5x0.2 in), further information on the ABPS component dimesions could be found in table 2.1. The unassembled ABPS comprised of several panels (i.e., 4 panels), each contained two columns that were welded to two transverse beams, as shown in Fig. 2.2. Longitudinal beams (i.e., side rails and supporting rails) were then connected to these panels using serrated strut nuts (i.e., friction sliding nuts), where all the associated bolts were torqued to the manufacturer's recommended values prior to testing. Finally, the end rails were connected to the side rails via L-shaped connections and serrated strut nuts, as shown in Fig. 2.1. Actual batteries were replaced with concrete blocks due to laboratory safety reasons, to avoid cracking of the actual batteries and a potential acid spill. Concrete blocks were used to provide the weight of batteries on the rack, where the dimensions and mass of each block were 217x265x464 mm and 65.8 kg, respectively. The end battery was made from built-up steel sections to also have the same dimensions and weight of the actual battery. Two load cells were also used at each end battery (i.e., four load

cells in total) to measure the force transferred directly to the end rail, as shown in Fig. 2.1.

The bottom transverse beam had a longer bottom flange with dimensions of 152x50.8x152x3.3 mm (6x2x6x0.13 in), thus acting as a base plate that was welded to the vertical column. The base plate had two anchor holes, one hole under each column, as shown in Fig. 2.1. The ABPS was anchored to a rigid reinforced concrete platform using post-installed anchors (i.e., anchor holes were drilled after curing of the reinforced concrete platform). More specifically, undercut type anchors, known for their high performance under seismic loads, were designed using Hiliti Profis software (Hiliti co. 2017). Lateral loads were determined following the IEEE 693-2018 (2018) high design seismic loads. Undercut type anchors were designed following CSA A23.3 (2014) anchor design requirements, and the governing failure mode was determined to be combined normal and shear forces. The anchors were designed to fail in a ductile manner as recommended by IEEE 693 (2018). HDA-P M12x125/30 (Hilti Inc.) anchor type was selected. Installation process followed CSA A23.3 (2014) and the manfacturer's recommended guidelines. Post-tensioned high strength steel bolts were used to connect the reinforced concrete platform to the labsoratory structural floor, as shown in Fig. 2.2.

2.3.2. Test Setup

As shown in Fig. 2.1, the lateral cyclic displacement was applied horizontally to the batteries on the top tier in the longitudinal direction. The lateral cyclic displacement was applied using a hydraulic actuator, with a capacity of 500 kN and a maximum stroke of 250 mm in both directions. The actuator was connected to a rigid reaction frame and was allowed to rotate freely in all directions through the use of rotational swivels at both ends. The actuator was attached to the ABPS through a double angle horizontal loading beam using a loading plate. The loading plate was designed to have enough clearance to the end rail throughout the test. The horizontal loading beam was welded to the end batteries, as shown in Fig. 2.2. An additional load-control vertical hydraulic actuator was used to support the weight of the horizontal actuator, which was mainly used to minimize the influence of any additional vertical loads from the horizontal actuator on the ABPS throughout the test.

2.3.3. Instrumentation

Eight displacement transducers (D1 to D8) were used to measure the deformations at the top of the columns in the loading direction, where D1 to D4 are shown in Fig. 2.2 for illustration. Eight additional displacement transducers (D9 to D16), also shown in Fig. 2.2, were used to measure the deformations of the columns at the bottom tier. As shown in Fig. 2.2, each column was connected to two longitudinal side rails, one at each tier, through serrated strut nuts. As such, sixteen

displacement transducers (D17 to D32) were used to measure the relative sliding deformations between the columns and these longitudinal side rails, where D22 and D28 are shown in Fig. 2.1 for illustration. Due to the unsymmetrical bracing configuration of the ABPS, four displacement transducers (D33 to D36) were used to measure the ABPS deformations perpendicular to the loading direction.

The tension deformations of the anchors were measured using a linear displacement transducer at each anchor (D37 to D44), only D38 is illustrated in Fig. 2.1. Since the anchors used were smaller than the holes in the ABPS, this permitted the ABPS to slide relative to the anchors. As such, eight displacement transducers (D45 to D52) were used to measure such sliding relative to the concrete platform, as shown in Fig. 2.1. The end rail is connected to the side rails using serrated strut nuts (i.e., friction sliding nuts), as such, four displacement transducers (D53 to D56) were used to measure the relative deformation between the sie rails and the end rails, as shown in Fig. 2.1.

Four strain gauges (S1 to S4) were used to monitor the strains of the braces at their midpoints, as shown in Fig. 2.1. To capture the strains in the columns, two strain gauges were mounted on each column of the eight columns (S5 to S20). In each column, one strain gauge (e.g. S5) was mounted vertically in the longitudinal direction, while the other strain gauge (e.g. S6) was mounted horizontally in the longitudinal direction, as shown in Fig. 2.1. Moreover, four strain gauges (S21 to S24) were used to measure the axial strain in the side rail at each end, as shown in Figs. 2.1 and 2.2. Refere to appendix A for for full list of instrumentation used.

2.3.4. Loading Protocol

In the current study, the FEMA 461 (2007) quasi-static testing protocol was adopted. According to this protocol, a 40% increase in the displacement amplitude of the top row of batteries was used for the first 12 cycles to reach a displacement of 14.1 mm, with a corresponding drift of 1.18% [i.e. this predicted yield drift was based on a preliminary numerical model (not presented herein (CSI 2009))]. Beyond this drift level, a constant increase in the amplitude of 4.26 mm (i.e. 0.3x14.1 mm) was used until the end of the test, as per the FEMA 461 guidelines. The ABPS was loaded at each displacement level twice, whereas the ABPS was subjected to 65 quasi-static fully reversed cycles in total, as shown in Fig. 2.3. The test was terminated at cycle 65 (i.e. degradation to 64% of the ABPS ultimate strength) due to the failure of the L-shaped connection between the end and side rails, as will be discussed later.

2.4. EXPERIMENTAL RESULTS

2.4.1. Overall Hysteretic Response

Figure 4 shows the load-displacement response of the ABPS in both directions. At early loading stages (i.e., after 0.16% drift), the braces started buckling elastically, due to their low Euler buckling load (i.e., 1 kN). Afterward, the L-shaped connection between the end and side rails started to rotate inelastically around the serrated strut nuts, as shown in Fig. 2.5a. The inelastic response of the L-shaped connection relative to the side rail is shown in the bottom right corner of

Fig. 2.4. This behavior continued to develop until yielding of the braces occurred, due to excessive buckling, at a displacement of 22.7 mm (i.e., Cycle 30 corresponding to 2.17% drift). The test progressed to reach a displacement of 40 mm in both directions with a corresponding drift ratio of 3.33% (i.e., Cycle 38). Beyond this drift level, the lateral load started to plateau until the test was terminated due to the failure of the L-shaped connection between the end rail and the side rail in addition to an excessive deformation in the end rail (shown in Fig. 2.5) at Cycle 65 reaching a maximum displacement of 99 mm and 96 mm in the push and pull directions, respectively. More specifically, the L-shaped connection and the end rail was not able to secure the batteries in place in the pull direction, where the batteries would topple off the ABPS beyond this drift level.

In cycles 63 and 65 (corresponding to 94 and 99 mm, respectively), the ABPS sustained almost the same load in the push direction, as shown in the top left corner of Fig. 2.4. However, in the pull direction of cycle 64, the end rail was severely deformed, which led to the failure of the L-shaped connection at a displacement of 94 mm in Cycle 65 in the pull direction. As such, the ABPS was incapable of reaching the prescribed displacement (99 mm) of Cycle 65 in the pull direction. In addition, the end rail also failed to carry the same load in Cycle 65 (i.e., 18 kN) compared to Cycles 63 and 64 (i.e., 28 kN), as shown in Fig. 2.4.

Although the main reason to use the serrated strut nuts (i.e., friction sliding nuts) was to make the in-situ formation of ABPS more feasible, as per the manufacturer's claim, these nuts can also be used to enhance the performance of

ABPS. Specifically, (Butterworth, et al., 2000; MacRae, et al., 2010) have reported similar behavior (i.e., sliding/gap/pinching) for steel moment-resisting frames with friction connections to be used as means for energy dissipation. Moreover, Terentiuk et al. (2012) also reported similar behavior for steel frames with friction insulated panels.

2.4.2. Stiffness and Ductility Response

The initial stiffness of the ABPS (K_o) in each direction was evaluated as the ratio between the maximum applied load of the first cycle and the corresponding displacement. It should be noted that the columns of the ABPS had a C-channel cross-section with flanges parallel to the direction of loading, as shown in Figs. 2.1 and 2.2. In addition, due to the anchoring procedure provided by the manufacturer and the direction the columns were oriented during testing, as shown in Fig. 2.6, the columns were able to rotate in the pull direction but remained restrained against rotation in the push direction due to bearing against the rigid platform. This contributed to a difference in the initial stiffness of the ABPS in each direction, where the initial stiffness of the ABPS in the pull direction (i.e., K_o=2.4 kN/mm) was approximately half its counterpart in the push direction (i.e., K_o=5.18 kN/mm).

The secant stiffness (K_i) was calculated at each displacement level as the ratio between the maximum ABPS load and the corresponding displacement. The secant stiffness (K_i) was normalized to the initial stiffness (K_o), as an indicative measure to the damage level of the rack (Adams, et al., 1975; Adams, et al., 1978),

as shown in Fig. 2.6. As can be seen in this figure, the lateral stiffness of the ABPS reached 25% of the initial stiffness at Cycles 9 (0.08% drift) and 10 (0.11% drift) in both the push and pull directions, respectively. By the end of the test (i.e., 8.33% drift), the ABPS secant stiffness reached 4% and 8% of the initial stiffness in both the push and pull directions, respectively. This difference in the normalized secant stiffness of the rack, between the push and pull directions, might be attributed to the use of columns (i.e., c-channel cross-sections) with eccentric connections to longitudinal beams (i.e., side rails) and bracings. This performance led the columns to experience excessive torsional (i.e., warping) deformations in one direction compared to the other.

Ductility is another metric to evaluate the seismic response characteristic of a system, which is typically used to provide more economic seismic designed structures (Babaei, 2015). To quantify the ductility of the rack, a bilinear idealization of the envelope of the hysteretic load-displacement relationship was utilized following the Eurocode 8-03 (2003) methodology. The idealization methodology described in this code is best used as this methodology does not specify a strength degradation limit compared to other methodologies (for example (Tong, et al., 2005; Valizadeh, et al., 2012)). As such, the ultimate displacement could be considered as the maximum displacement reached by the rack in each direction. While the yield load was assumed to be the maximum applied load. Subsequently, the yield displacement was determined from equating the area under the idealized load-displacement relationship to the area under the experimental

load-displacement envelope. It is worth mentioning that since the test was terminated due to the failure of end rail during the maximum pull cycle only, the ultimate displacement point could be defined for the pull direction (96 mm); however, in the push direction, the ultimate displacement was assumed as the maximum achieved displacement (99 mm). Figure 2.7 shows the idealized bilinear curves for both the push and pull directions. The difference between the experimental results and the idealized bilinear curve is attributed to the excessive nonlinear deformations observed in the experimental testing during the buckling of the braces, the rotation of the L-shaped connection, the deformation of the serrated nuts and the torsional (i.e., warping) behavior of the columns. The figure shows that the yield strength of the ABPS was 21 and 28 kN for the push and pull directions, respectively. In addition, the unsymmetrical boundary condition (partially fixed in push and hinged in pull) resulted in different yielding displacements of 43 mm and 71 mm in the push and pull directions, respectively. Therefore, the ductility capacity of the ABPS was 2.3 and 1.32 in the push and pull directions, respectively. These ductility capacities should be carefully considered as they appear to be relatively low compared to similar steel structures (i.e., braced steel frames) that have ductility estimates typically ranging from 2-5 (CSA S16-14, 2014). These low ductility capacities of the ABPS were mainly due to the local failure of the L-shaped connection and the excessive deformation of the end rail, which limited the lateral capacity of the ABPS, as previously discussed and shown in Fig. 2.5.

Based on the above results, neglecting this unsymmetrical stiffness and ductility behavior of the ABPS during the design stage may lead to an incorrect estimate of the overall seismic response of ABPS. Moreover, Priestley et al. (2007) argued that neither relying on the maximum absolute displacement or the average of the positive and negative displacements have enough valid justification to be used in the displacement-based design approach. As such, failure to carefully consider this unsymmetrical behavior during design may have a direct effect on the NPP overall CDF, as the failure of ABPS has a 9% contribution to the overall CDF, as mentioned earlier. To be on the conservative side, the lateral properties of the weaker side of the ABPS could be used to evaluate a lower bound CDF.

2.4.3. Member Strains

Figure 8 shows the buckling of the braces during the test, where braces 1 and 3 buckled during the pull direction cycles, whereas braces 2 and 4 buckled during the push direction cycles. Figure 2.9 shows the maximum and minimum measured strains for all braces at each displacement level. Figure 2.9a shows that brace 1 reached the yield strain (i.e., 1650micro-strain determined from material tension tests as will be discussed later) at a displacement level of 56 mm (i.e., Cycle 45 corresponding to 4.67 % drift), whereas Fig. 2.9b shows that brace 2 reached the yield strain at a displacement level of 22.7 mm (i.e., Cycle 29 corresponding to 1.84% drift). Also, Fig. 2.9c shows that brace 3 reached the yielding strain at a displacement level 90.7 mm (i.e. drift 7.34%), while Fig. 2.9d shows that brace 4

behaved elastically until the test was terminated. The different behaviors between braces 2 and 4 and braces 1 and 3 are attributed to the unsymmetrical behavior of the ABPS between push and pull directions, and the use of C-channel cross-section columns that experienced excessive torsional (i.e., warping) deformations in one direction compared to the other, as mentioned earlier.

The strains at the bottom of the columns were also monitored during testing, in both vertical and horizontal directions, as previously mentioned. Figures 2.10a and 2.10b show the maximum measured vertical strains in Columns 1 and 2, respectively, while Figs. 2.10c and 2.10d show the maximum measured horizontal strains in Columns 7 and 4, respectively. As shown in Fig. 2.10, all columns behaved elastically until the test was terminated.

The above results have shown that the bracing system of the ABPS behaved as intended; the early buckling of the bracing system resulted in an increased energy dissipation compared to the frames without braces. This intended behavior of the braces helped prevent the structural failure of the main ABPS elements (i.e., columns, side rails, and supporting rails), and after seismic events, this bracing system could be easily replaced, while replacing the end rail and accompanying connections without fully disassembling of the ABPS.

2.4.4. Twist Response

To better understand the 3D behavior of the ABPS, the relative deformation of the top of the columns was examined in terms of the twist response. Since there

is no clear diaphragm action to fix the rotation of all the column top points around the vertical axis, the twist of the rack is defined in both the direction of loading and perpendicular to the direction of loading independently, a schematic diagram of the twist response is shown in the bottom left corner of Fig. 2.11. As shown in the figure, the twist response in the direction of loading was calculated as the ratio of the relative displacements in the direction of loading between the columns in the South and North longitudinal directions of transverse frame 2 to the distance between these columns (431 mm). Conversely, the twist response perpendicular to the direction of loading was calculated as the ratio of the relative displacements perpendicular to the direction of loading between transverse frames 1 and 4 to the distance between these frames (3,201 mm), as shown in Fig. 2.11. As shown in Fig. 2.11, the ABPS experienced a significant twist response in the direction of loading compared to perpendicular to the direction of loading throughout the test. For example, the ABPS twist responses in the direction of loading were 3.31 and 3.09 degrees at displacement level of 31.2 mm in the push and pull directions, respectively, while the ABPS twist responses perpendicular to the direction of loading were only 0.05 and 0.13 degrees at the same displacement level. Eventually, the twist in the direction of loading increased as the test progressed, reaching a maximum value of 7.50 and 8.65 degrees in the push and pull directions, respectively. This significant twist response in the direction of loading is attributed to the presence of braces in the South frame only. As such, higher seismic grade racks provided by the same manufacturer (i.e., EP2) equipped with the symmetric

bracing system between the North and South longitudinal frames would not experience such high twist response in the direction of loading.

2.4.5. End Rail Deformations

As mentioned earlier, the test was terminated due to the failure of the L-shaped connection between the end and side rails during the pull direction of Cycle 65 at a displacement of 94 mm, as shown in Fig. 2.5. Figures 2.12 (a and b) show the damage sequence of the connection between the front end rail and the side rail in the South frame (Connection 2) (i.e., longitudinal frame with braces) at cycles 15 and 55, respectively, while Figs. 2.12 (c and d) show the deformation of the connection between the same front end rail and the side rail in the North frame (Connection 1) (i.e., longitudinal frame without braces) at the same cycles. It can be noticed from Fig. 2.12 that Connection 2 experienced more damage compared to Connection 1. This is mainly attributed to the longitudinal braces within the South frame of Connection 2 that reduced the overall ductility of this frame compared to the North frame. As such, the deformations in the North frame (Connection 1) were largely taken by the columns; however, deformations of the South frame were predominantly in Connection 2. To quantify this unsymmetrical behavior between both sides of the ABPS, Fig. 2.13 shows the maximum deformations of Connections 1 and 2 at each displacement level relative to the North and South frames, respectively. As shown in Fig. 2.13, the deformations of Connection 2 are almost twice those of Connection 1 throughout the test. Similar

observations were also noticed between the deformations of Connections 3 and 4 in the push direction but with lower values due to the unsymmetrical behavior between the push and pull directions, as mentioned earlier. The above results have shown that the overall ABPS capacity was mainly governed by the dominant failure mode of the L-shaped connection between the end and the side rails. Therefore, the installation of additional longitudinal braces to seismically upgrade the ABPS performance (e.g., from EP1 to EP2 class for this manufacturer), as mentioned earlier, might have a minimal effect on the ABPS overall capacity. However, upgrading the L-shaped connection, by changing dimensions or increasing thickness will directly affect the overall capacity of the ABPS.

2.4.6. Anchor Behavior

Previous studies (Johnson, et al., 1999; Porter, 2009), demonstrated that anchor failure is a common mode of failure in ABPS. As such, tension and sliding deformations of the anchors were monitored throughout the test in the current study. According to the manufacturer, the anchor's hole in the ABPS is 17.5 mm, while the used anchor was 12 mm. This allowed the columns to slide relative to their corresponding anchors. According to CSA S16-14 (2014), a larger anchor should have been used to avoid such large sliding deformations; however, the anchors used in the test met the ACI 318-14 (2014) and IEEE 693-2018 (2018) design limits. As such, the use of code sufficient anchors (i.e., not oversized anchors) facilitated a

direct comparison with the anchor failure mode already found in the literature (Johnson, et al., 1999; Porter, 2009).

Figure 14 shows these slip responses in the push and pull directions, where the maximum slip was at Column 3 in the push direction with a maximum deformation of 4.3 mm. The bottom right corner of Fig. 2.14 shows the change in the relative position of the columns at each displacement level. The relative positions of the columns were calculated as the average between the maximum and minimum deformation of each column at each displacement level as an indication of the sliding progress of the columns. As shown in Fig. 2.14, some columns experienced only slip in the push direction, which increased as the testing progressed. Column 2 experienced a maximum slip of almost 3 mm. The slip of the columns in one direction could also contribute to the unsymmetrical behavior of the ABPS during the push and pull directions. Figure 2.15 shows the maximum measured tension deformation of the anchors at each displacement level. As shown in Fig. 2.15, anchors 1 and 8 experienced the highest axial deformation demands reaching 0.82 and 1.13 mm, respectively. However, all anchors remained undamaged until the test was terminated at Cycle 65. Accordingly, although all these anchors were smaller in diameter than that recommended by the CSA S16-14 (2014), anchor failure mode, as reported in the literature (Johnson, et al., 1999; Porter, 2009) for similar battery ABPS systems used in NPPs, was not observed until the end of the test at Cycle 65. This could be attributed to several reasons

including the premature failure of the L-shaped connection and the configuration of the ABPS tested.

2.5.   SIMPLIFIED MECHANISTIC MODEL OF THE ABPS

A simplified mechanistic model was developed in the current study for the ABPS in order to facilitate the adoption of this system within the next editions of relevant building codes and design standards (e.g., IEEE-693, 2018). The simplified mechanistic model of the ABPS was developed using the stiffness matrix formulation method. In order to effectively simulate the performance of the ABPS, material properties had to be determined. For this reason, three tension tests were performed on three brace members to evaluate their properties according to the ASTM E8 (2016). According to these tests, Young's modulus and the yield strength of the steel material were found to be 216 GPa and 316 MPa, respectively.

A schematic diagram of the model is shown in the top left corner of Fig. 2.16. As shown in the figure, the end rail is simulated as a rigid bar supported on the North and South frames. The bilinear lateral responses of the North and the South frames were determined using a matrix formulation of a partially hinged base frame without and with bracings, respectively, as shown in the bottom right corner of Fig. 2.16. The base support rotational stiffness was calculated based on the bottom plate dimensions as shown in Fig. 2.6, assuming the base plate could uplift in the pull direction (i.e., fixed free beam) and is restrained from rotation in the push direction (i.e., fixed-hinged beam). The yield points of the North and South

frames were governed by the yielding of the beam and the tension bracing, respectively.

The lateral displacement in the experimental testing was measured at the center of mass of the batteries at the top tier, consequently, the average of the lateral response of the North and the South frames were evaluated and compared to the experimental results, as shown in Fig. 2.16. As can be seen in the figure, the developed model clearly overestimates the lateral behavior (i.e., initial stiffness and yielding properties) of the ABPS, as this model lacks explicit simulation of the local behavior of the ABPS connections (i.e., L-shaped connection and the serrated strut nuts).

Local deformations of the L-shaped connection between the front-end rail and the South frame prevented the full utilization of the lateral capacity of the ABPS. As such, neglecting to include the effect of the L-shaped connection leads to a discrepancy between the experimental findings and the developed model. To address this issue in the developed model, the bilinear behavior of the L-shaped connection was determined from first principles. The connection was modeled as a rotational hinge at the end of a vertical cantilever element, and assuming the load was applied at the free endpoint, thus the yield rotation and the yield force can be determined as follows

$$\theta_y = \frac{Z F_{ye} l_b}{3 E I_b} \qquad (1)$$

Where θ_y is the yield rotation, Z is the plastic modules of the L-shaped cross-section, F_{ye} is the material yield strength, l_b is the length of the L-shaped connection, E is the modulus of elasticity, and I_b is the moment of inertia of the L-shaped cross-section. As such, using the material properties and the above formulation the yield rotation and the yield force were determined to be 0.007 rad and 9.1 kN, respectively. The ultimate deformation of the L-shaped connection was determined from the experimental results to be 96 mm (i.e., the maximum deformation that caused the release of the nut from the end rail).

Furthermore, the difference between the experimental envelope and the developed model is also attributed to the negligence of the influence of the eccentric connection between the columns and the side rails. For example, Shi et al. (2018) studied the influence of eccentricity of rectangular beam-column connections. The eccentricity of the beam-column connection would cause additional unintended torsional deformations, which can result in the decrease of the elastic rotational stiffness of the eccentric rectangular beam-column connection to 30% of the concentric connection counterpart (Shi, et al., 2018). Moreover, the use of C-channeled cross sections for beams and columns, in the currently tested ABPS, will result in lower rotational stiffness compared to rectangular beams and columns. As such, in order to capture the reduced elastic rotational stiffness of the beam-column connection, rotational spring elements were added to the North and South frames at both ends of all the beams (i.e., side rails). Stiffness matrix formulation of a beam member with rotational springs at both ends was employed. Wang (2013) studied

the formulation of an updated stiffness matrix of a column element to account for the relative rotation between the column element and the supports due to the presence of rotational springs (i.e., partial fixation) at column ends. Similar results were also reported by Ihaddoudène et al. (2009). The rotational spring between the columns and the beams was developed to behave in a linear elastic manner, the stiffness of the rotational spring was calibrated in order to match the total model pushover curve against the envelope of the experimental results.

Superposition of the L-shaped connection model and the modified frame model was used to determine the bilinear responses of the South and the North frames. A schematic diagram of the model is shown in the bottom right corner of Fig. 2.17. Subsequently, the average responses of the North and South frame were evaluated and compared to the experimental results, as shown in Fig. 2.17. The rotational properties of the partially fixed connection of the South and North frames were calibrated, where it was found that the elastic rotational stiffness of the connection should be 2% of the fixed connection counterparts to achieve a good match against the experimental results. As such, the use of serrated strut nuts to facilitate the in-situ formation resulted in a reduction of the lateral stiffness of the ABPS. Moreover, the yielding of the L-shaped connection limited the full utilization of the higher yielding lateral load of the ABPS. Figure 2.17 shows the calibrated pushover model and the experimental envelope. It is postulated that the difference between the mechanistic model and the experimental results is attributed to the negligence of the coupling effect between the North and South frames as a

result of the transverse beams. As such, there is a significant need for comprehensive 3D models to account for the coupling effects between the North and South frames and the nonlinear behavior of the different connections. It is worth mentioning that the capacity of the ABPS was determined experimentally from the failure of the lip of the C-channel end rail bearing against the serrated strut nuts.

2.7. NUMERICAL MODEL OF THE ABPS

Nonlinear time history analysis and the corresponding nonlinear dynamic procedure have been considered a more desirable design approach in several standards (NIST, 2017) compared to the nonlinear static procedure. As such, a simplified nonlinear numerical model is developed in the current study using OpenSees and calibrated against the experimental hysteretic behavior of the ABPS. The concentrated plasticity (spring) approach is adopted, where the behavior of the ABPS is simulated using an elastic beam-column element and a zero-length rotational spring. The rotational spring followed the modified Ibarra-Medina-Krawinkler Deterioration (ModIMKPinching) Model with Pinched Hysteretic Response (Ibarra, et al., 2005). Parameters controlling the hysteretic behavior of the spring have been calibrated such that the overall cyclic behavior of the model closely matches the experimental hysteretic behavior of the ABPS. Specifically, the elastic beam-column element initial stiffness (k_{bc}) and the zero-length element stiffness (k_s) were determined based on

$$k_{bc} = \frac{n+1}{n} k_{ABPS} \qquad\qquad (2)$$

$$k_s = (n+1)k_{ABPS} \qquad\qquad (3)$$

where k_{ABPS} is the overall ABPS elastic stiffness, n is the modification factor to avoid numerical problems that is taken to be 10 as suggested by Ibarra and Krawinkler (2005). ModIMKPinching material model ignores the asymmetric behavior of the ABPS, as such, k_{ABPS} was taken as the average of the elastic stiffnesses of the ABPS from the experimental test in the push and pull directions. Cyclic degradation parameters were taken based on the recommended parameters by Ibarra and Krawinkler (2005). As shown in the experimental results, the ABPS did not undergo any post-capping behavior, as such the post-capping parameters are not considered herein.

Figure 18 compares the results of the numerical model with the experimental results of the tested ABPS. As shown in Fig. 2.18, the model is in good agreement with the experimental results. The model is capable of matching closely the post-yielding behavior of the ABPS; however, the model overestimates the ABPS response at the early stages of loading, as ModIMKPinching material model ignores the cyclic strain hardening feature present in steel structures (Ibarra and Krawinkler, 2005). Moreover, the pre-yielding maximum error was found to be 35% and 20 % for both pull and push directions, respectively, while the post-yielding error decreased to 16% and 8% for pull and push directions, respectively. This difference in the error in the pre-yielding response is caused by the

ModIMKPinching material model that ignores asymmetric hysteretic behavior. However, as discussed by Ibarra et al. (2005), the large inelastic cycles with significant deterioration are well simulated. In addition, Fig. 2.19 compares the individual experimental and numerical hysteresis loops at displacement levels of 48 mm, 65.25 mm, and 90.75 mm, respectively (i.e., 4%, 5.4%, and 7.6%, respectively). As shown in Fig. 2.19, the model is capable of predicting closely the hysteretic loading stiffness, the unloading stiffness, and the energy dissipation.

2.7. CONCLUSIONS

The current study presents the experimental results of an existing/operational ABPS. The ABPS was tested under a displacement-controlled quasi-static cyclic loading protocol, as per FEMA 461 guidelines, in the longitudinal direction. In total fully reversed 65 Cycles were performed reaching a maximum deformation of 99 mm (i.e., 8.33 % drift ratio). The experimental results were presented in terms of the rack's total displacement and the corresponding local component deformations and strains. A simplified mechanistic model was also developed and calibrated to facilitate the adoption of this ABPS within the future editions of relevant building codes and design standards.

The experimental results demonstrated that the test displacement response was mainly transferred to the ABPS through an L-shaped connection between the end rail and the side rail. This was due to the use of braces which reduced the ABPS lateral deformation, and therefore, most of the displacement demands were

transferred directly to this connection. The inelastic response of this connection significantly increased until the test was terminated due to its failure, followed by excessive buckling of the braces that eventually yielded. The local failure of the L-shaped connection prevented the full utilization of the ABPS lateral capacity and reduced the ABPS ductility capacity.

The simplified mechanistic model showed that incorporating local failure of the connection and rotational springs at the beam-column connections were essential in modeling the ABPS. The calibrated model also demonstrated that neglecting such behavior can lead to unrealistic response predictions. Therefore, the fact of complete safety of NPPs should be addressed, and the investigation of new design techniques should be performed.

Finally, a concentrated plasticity (spring) model in OpenSees was developed to simulate the hysteretic response of ABPS. The lateral behavior of the ABPS was simulated using an elastic beam-column element with a nonlinear zero-length rotational spring. The overall nonlinear lateral behavior of the ABPS was used to calibrate the material properties used in the model. The model was found to be in good agreement with the experimental results at different drift levels.

Although the differences between the experimental and model results can be considered acceptable given the complexity of such rack local failures caused by the impact of the sliding batteries against the end rail, advanced numerical models (e.g., using Mastan2, Midas, and SeismoStruct) are still needed to account for several complex behaviors, such the nonlinear behavior of the different

connections, warping and torsional effects of C-channeled cross-sections, coupling effects between North and South frames, and second-order effects.

Since the experimental testing was performed on a specific, but common, rack type, more research is required to investigate other seismically qualified racks. The developed model is also validated using the quasi-static experimental results of the current study. Further investigations should be carried out to develop and validate mechanistic models that are based on shake table results to better represent the ABPS under dynamic events.

The currently adopted test setup ignores higher mode effects. As such, research may still be needed to assess higher mode effects through experimental tests and numerical models.

2.8.   ACKNOWLEDGMENT

2.9.   REFERENCES

ACI 318-14. (2014). *Building code requirements for structural concrete.* ACI.

Adams, R., Cawley, P., Pye, C., & Stone, B. (1978). A vibration technique for non-destructively assessing the integrity of structures. *20*(2), 93-100. DOI: 10.1243/JMES_JOUR_1978_020_016_02

Adams, R., Walton, D., Flitcroft, J., & Short, D. (1975). Vibration testing as a nondestructive test tool for composite materials. American Society for Testing and Materials, Composite Reliability ASTM STP 580, 159-175.

Aguirre, C. (2005), Seismic behavior of rack structures. *Journal of Constructional Steel Research*, 61.

ASCE. (2016). *Minimum design loads for buildings and other structures.* Reston, VA: ASCE/SEI 7-16.

ASTM E8. (2016). *Standard Test Methods for Tension Testing of Metallic Materials.* AASHTO.

Babaei, M. (2015). The Economical Effect of Ductility Levels on Reinforced Concrete Frames Design. *American Journal of Civil and Structural Engineering, 2*(1).

Berak, E., & Marconi Communications. (2005). Modal testing and finite element analysis of a battery rack for seismic applications. *Journal of the IEST, 48*(1).

Bernuzzi, C., Gobetti, A., Gabbianelli, G., & Simoncelli, M. (2014). Warping influence on the resistance of uprights in steel storage pallet racks. *Journal of Constructional Steel Research*, *101*, 224-241.

Bernuzzi, C., Gobetti, A., Gabbianelli, G., & Simoncelli, M. (2015a). Unbraced pallet rack design in accordance with European practice–Part 1: Selection of the method of analysis. *Thin-Walled Structures*, *86*, 185-207.

Bernuzzi, C., Gobetti, A., Gabbianelli, G., & Simoncelli, M. (2015b). Unbraced pallet rack design in accordance with European practice–Part 2: Essential verification checks. *Thin-Walled Structures*, *86*, 208-229.

Bernuzzi, C., Di Gioia, A., Gabbianelli, G., & Simoncelli, M. (2017). Pushover analyses of hand-loaded steel storage shelving racks. *Journal of Earthquake Engineering*, *21*(8), 1256-1282.

Butterworth, J., & Clifton, C. (2000). Performance of hierarchical friction dissipation joints in moment resisting steel frames. *12ᵗʰ World Conference on Earthquake Engineering.*

C&D Technologies (2012). Flooded battery racks: selection guide for RDB & RDC series, standby battery racks. - Mississauga, ON, Canada: C&D Technologies.

C&D Technologies. (2007). *Standby battery rack assembly instructions: Applies to all RDB series packs.* Blue Bell, PA: C&D technologies.

C&D Technologies Inc. (2017). Retrieved from http://www.cdtechno.com.

Chen, C. K., Scholl, R. E., & Blume, J. A. (1980). Earthquake simulation tests of industrial steel storage racks. In *Proceedings of the Seventh World Conference on Earthquake Engineering, Istanbul, Turkey* (pp. 379-386).

Cho, S., Kim, D., & Chaudhary, S. (2011). A simplified model for nonlinear seismic response analysis of equipment cabinets in nuclear power plants. *Journal of Nuclear Engineering and Design, 241*, 2750-2757.

Choun, Y.-S., Choi, I.-K., & Seo, J.-M. (2004). Improvement of seismic safety of nuclear power plants by increase of equipment seismic capacity. *13th world conference on earthquake engineering.* Vancouver, B.C., Canada.

Choun, Y.-S., Choi, I.-K., & Seo, J.-M. (2008). Improvement of the seismic safety of existing nuclear power plants by an increase of the component seismic capacity: A case study. *Nuclear Engineering and Design, 238*(6), 1410-1420.

Cosenza, E., Di Sarno, L., Maddaloni, G., Magliulo, G., Petrone, C., & Prota, A. (2015). Shake table tests for the seismic fragility evaluation of hospital rooms. *Earthquake Engineering and Structural Dynamics, 44*(1), 23-40.

CSA group. (2014). *Design of concrete structures, CSA A23.3-14.*

CSA S16-14. (2014). *Design of steel structures.* Canadian Standard Association CSA.

CSI, C. (2009). SAP 2000; Integrated software for structural analysis and design, version 14. Berkeley, California, USA.

EPRI. (1991). *Generic Seismic Ruggedness of Power Plant Equipment.* Oakland, CA: Electric Power Research Institute (EPRI) NP-5223-SL Revision 1.

Eurocode 8. (2003). *Design of Structures for earthquake resistance- Part 1: General rules, seismic actions and rules for buildings.* Brussels.

FEMA 461. (2007). *Interim testing protocols for determining the seismic performance characteristics of structural and nonstructural components.* Federal Emergency Management Agency (FEMA).

FEMA P-58. (2012). *Seismic performance assessment of buildings.* Washington, DC: Federal Emergency Management Agency (FEMA).

Filiatrault, A., Higgins, P. S., Wanitkorkul, A., Courtwright, J. A., & Michael, R. (2008). Experimental seismic response of base isolated pallet-type steel storage racks. *Earthquake Spectra*, *24*(3), 617-639.

Filiatrault, A., Bachman, R. E., & Mahoney, M. G. (2006). Performance-based seismic design of pallet-type steel storage racks. *Earthquake Spectra*, *22*(1), 47-64.

Funabashi, Y., & Kitazawa, K. (2012). Fukushima in review: a complex disaster, a disastrous response. *Bulletin of the Atomic Scientists, 68*(2), 9-21.

Ghith, A., Ezzeldin, M., Tait, M., & El-Dakhakhni, W. (2019). Shake Table Seismic Performance Assessment of Auxiliary Battery Power Systems Using the FEMA 461 Protocol. *Journal of Structural Engineering*, *145*(8), 04019080.

Gupta, A., & Yang, J. (2002). Modified Ritz vector approach for dynamic properties of electrical cabinets and control panels. *Nuclear Engineering and Design*, 49-62.

Gusella, F., Orlando, M., Vignoli, A., & Thiele, K. (2018). Flexural Capacity of Steel Rack Connections The Component Method. *The Open Construction & Building Technology Journal*, *12*(1).

Gusella, F., Orlando, M., & Spinelli, P. (2019). Pinching in steel rack joints: numerical modeling and effects on structural response. *International Journal of Steel Structures*, *19*(1), 131-146.

Hancock, G. J. (1985). Distortional buckling of steel storage rack columns. *Journal of Structural Engineering*, *111*(12), 2770-2783.

Hirano, M., Yonomoto, T., Ishigaki, M., Watanabe, N., Maruyama, Y., Sibamoto, Y., Moriyama, K. (2012). Insights from review and analysis of the Fukushima Dai-ichi accident. *Nuclear Science and Technology, 49*, 1-17.

Huang, B., Lu, W., & Mosalam, K. (2017). Shaking table tests of the cable tray system in nuclear power plants. *Journal of Performance of Constructed Facilities*.

Ibarra, L. F., & Krawinkler, H. (2005). *Global collapse of frame structures under seismic excitations* (pp. 29-51). Berkeley, CA: Pacific Earthquake Engineering Research Center.

Ibarra, L. F., Medina, R. A., & Krawinkler, H. (2005). Hysteretic models that incorporate strength and stiffness deterioration. *Earthquake engineering & structural dynamics*, *34*(12), 1489-1511.

IEEE-693, P. E. (2018). *IEEE Recommended Practice for Seismic Design of Substations.* IEEE Std 693.

Ihaddoudène, A., Saidani, M., & Chemrouk, M. (2009). Mechanical model for the analysis of steel frames with semi rigid joints. *Journal of Constructional Steel Research, 65*, 631-640.

Johnson, G., Sheppard, R., Quilici, M., Eder, S., & Scawthorn, C. (1999). *Seismic reliability assessment of critical facilities: a handbook, supporting documentation, and model code provisions.* Oakland, California: MCEER.

Kim, M., Choi, I.-K., & Seo, J.-M. (2012). A shaking table test for an evaluation of seismic behavior of 480 V MCC. *Nuclear Engineering and Design*, 341-355.

Koo, K., Cho, S., Cui, J., & Kim, D. (2010). Seismic response prediction for cabinets of nuclear power plants by using impact hammer test. *Nuclear Engineering and Design*, 2500-2511.

Krawinkler, H. (1978). Experimental study on seismic behavior of industrial storage racks. *International specialty conference on Cold-formed Steel Structures.*

Lai, Z.-Y., Chai, J.-F., Lin, F.-R., Chen, M.-Y., & Chou, P.-F. (2013). Experimental study for MCCs in Taiwan Lungmen Nuclear Power Plant. *22nd SMIRT.* San Fransisco, USA.

Lin, F.-R., Chai, J.-F., Lai, Z.-Y., Chang, K., Liao, W., Chou, P.-F., & Huang, C.-C. (2012). Experimental study of seismic qualification of incabinet equipment in NPP. Lisboa: WCEE.

MacRae, G., Clifton, G., Mackinven, H., Mago, N., Butterworth, J., & Pampanin, S. (2010). The sliding hinge joint moment connection. *43*(3), 202-212.

NAIIC, T. F. (2011). The National Diet of Japan.

NIST (2017). Guidelines for nonlinear structural analysis for design of buildings: Part I – General, Applied technology council.

Porter, K. (2009). *Fragility of Battery Racks.* Washington, D.C.: Federal Emergency Management Agency (FEMA) FEMA P-58 /BD-3.9.26.

Priestley, M., Calvi, G., & Kowalsky, M. (2007). *Displacement-Based Seismic Design of Structures.* Pavia, Italy: IUSS Press.

Rustogi, S., & Gupta, A. (2004). Modeling the Dynamic Behavior of Electrical Cabinets and Control Panels: Experimental and Analytical Results. *130*(511-519).

Sato, E., Furukawa, S., KaKehi, A., & Nakashima, M. (2011). Full-scale shaking table test for examination of safety and functionality of base-isolated medical facilities. *Earthquake engineering and structural dynamics, 40*(13), 1435-1453.

Shi, Z., & Fan, J. (2018). Analytical investigation on effective elastic stiffness of eccentric steel beam-column joints. *Advances in Structural Engineering*, 125-137.

SQUG. (1999). *Electronic Earthquake Experience Database User's Guide: eSQUG EPRIWEB Site.* Palo Alto, CA: EPRI, TR-113705.

Telcordia Technologies. (2002). Network Equipment-Building System (NEBS) Requirements: Physical Protection Specification GR-63-CORE, Issue 2.

Tepco Inc. (2011). Fukushima Nuclear Accident Analysis Report. Interim Report, Tokyo.

Terentiuk, S., & Memari, A. (2012). In-Plane monotonic and cyclic racking load testing of structural insulated panels. *18*(4), 261-275.

Tong, X., Hajjar, J., Schultz, A., & Shield, C. (2005). Cyclic behavior of steel frame structures with composite reinforced concrete infill walls and partially restrained connections. *61*, 531-552.

Valizadeh, H., Sheidaii, M., & Showkati, H. (2012). Experimental investigation on cyclic behavior of perforated steel plate shear walls. *70*, 308-316.

Wang, Q., Chen, X., & Yi-chong, X. (2013). Accident like the Fukushima unlikely in a country with effective nuclear regulation: Literature review and proposed guidelines. *Renewable and Sustainable Energy Reviews, 17*, 126-146.

Wang, S. (2013). Model updating and parameters estimation incorporating flexible joints and boundary conditions. *Inverse Problems in Science and Engineering, 22*(5), 727-745.

Yin, L., Tang, G., Li, Z., Zhang, M., & Feng, B. (2018). Responses of cold-formed steel storage racks with spine bracings using speed-lock connections with

bolts   I: Static   elastic-plastic   pushover   analysis. *Thin-Walled*

Structures, *125*, 51-62.

Table 2.1 Member cross section dimensions

Member	shape	d mm (inch)	Bf1 mm (inch)	Bf2 mm (inch)	t mm (inch)
Column	C-channel	76 (3)	76 (3)	50 (2)	5 (0.2)
Side rail/ end rail/ supporting rail	C-channel	46 (1.64)	46 (1.64)	46 (1.64)	2.5 (0.1)
Girder	C-channel	76 (m)	50 (2)	50 (2)	5 (0.2)
Bottom girder	C-channel	152 (6)	50 (2)	101 (4)	5 (0.2)
Brace	rectangle	38 (1.5)	-	-	5 (0.2)
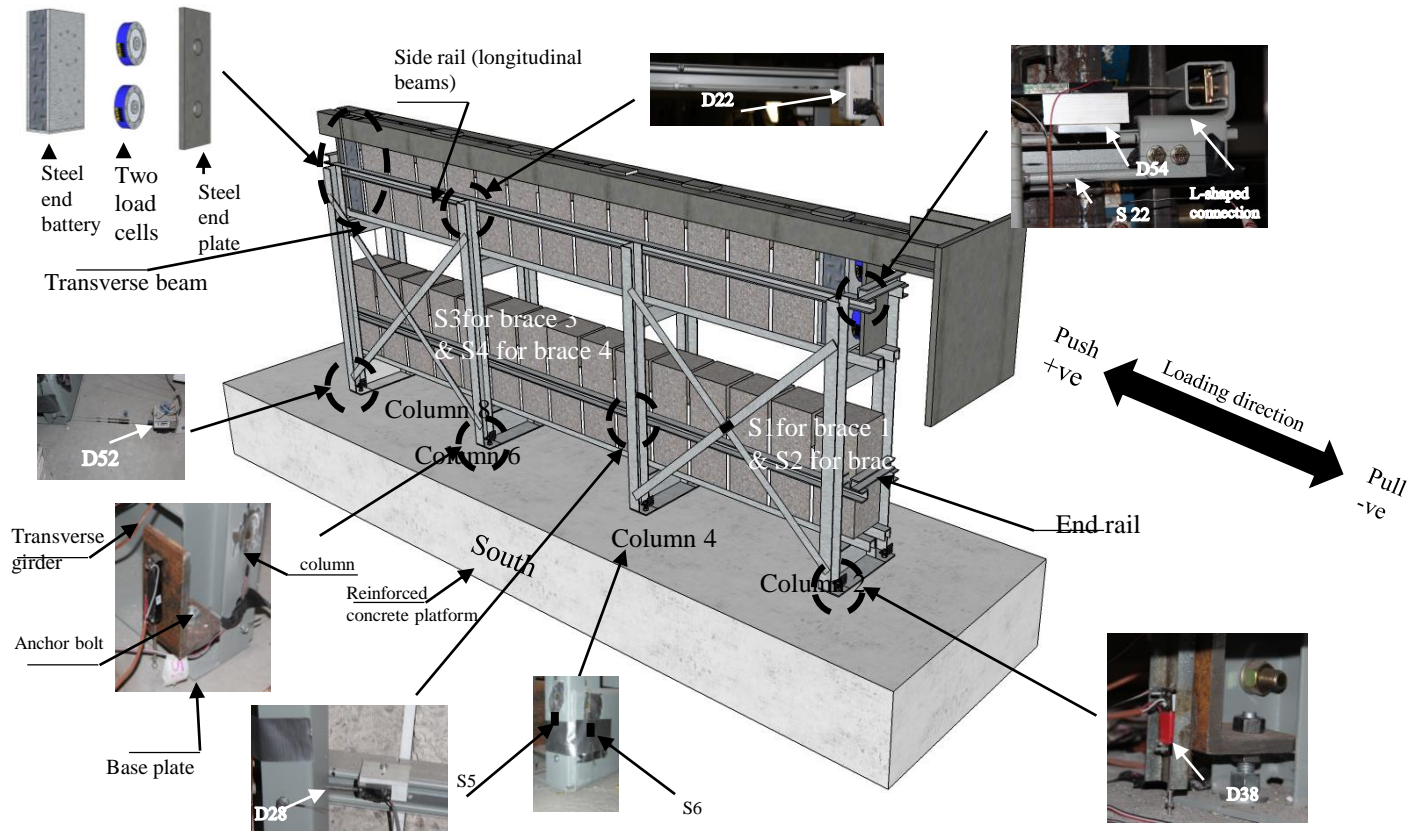
Figure 2.1: Rack configuration and instrumentation.
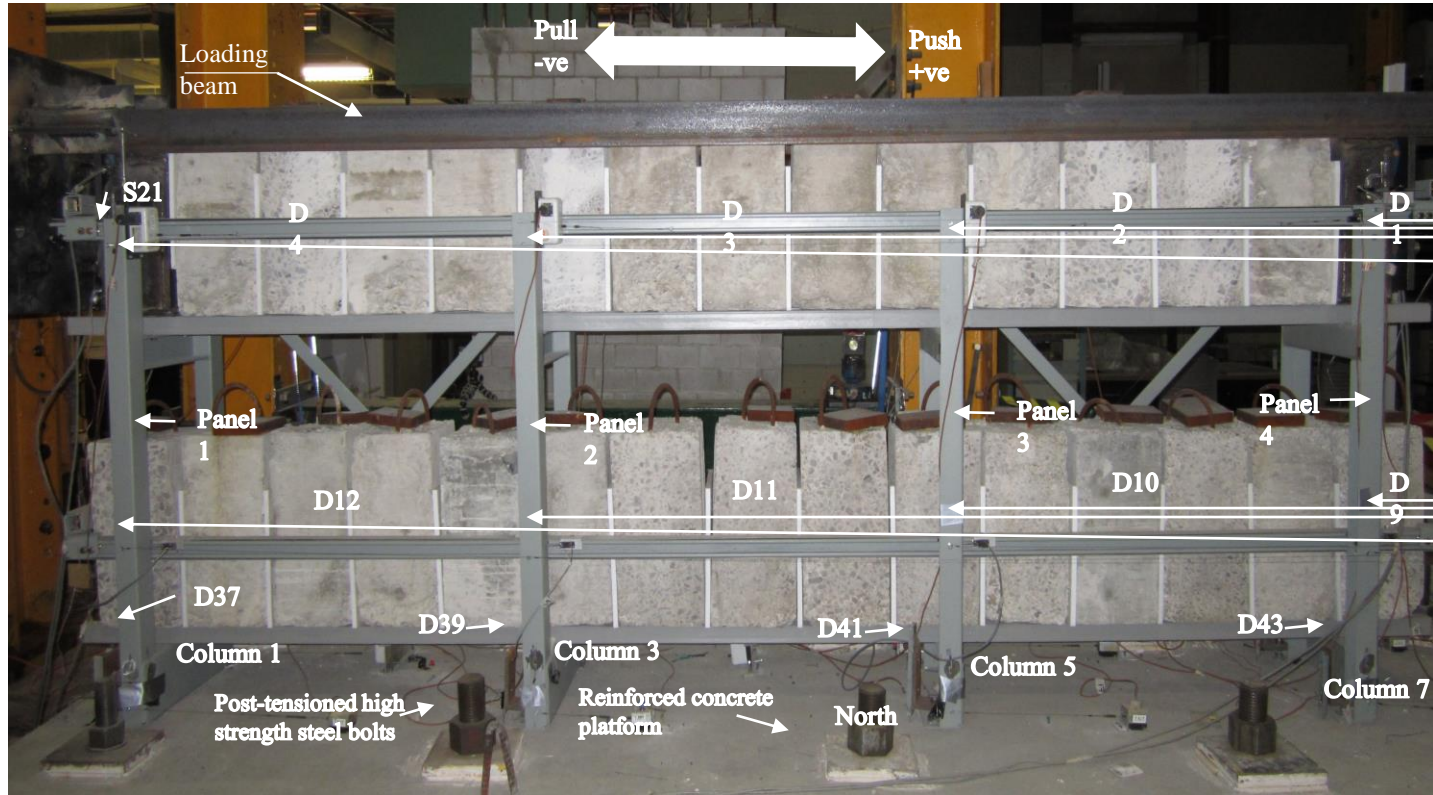
Figure 2.2: Test setup and instrumentation.
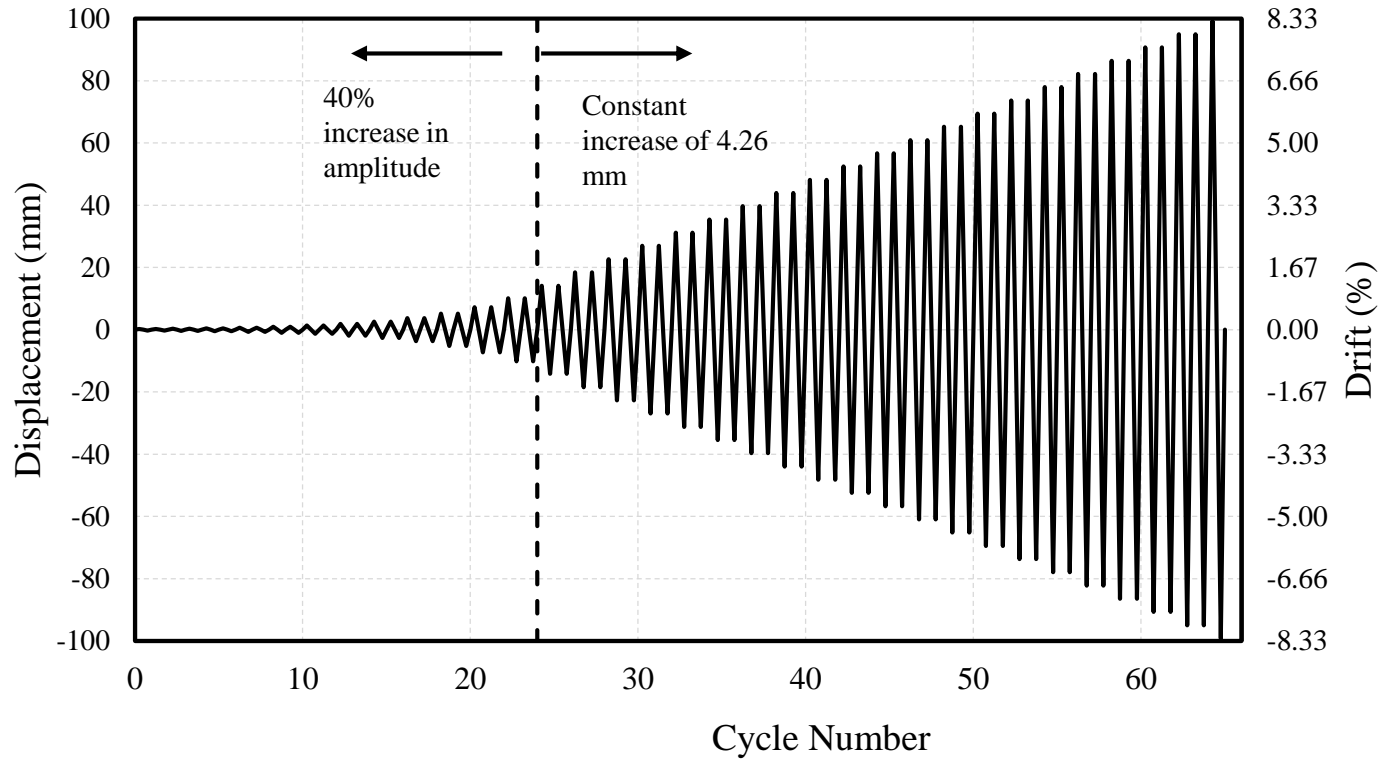
Figure 2.3: Loading protocol.
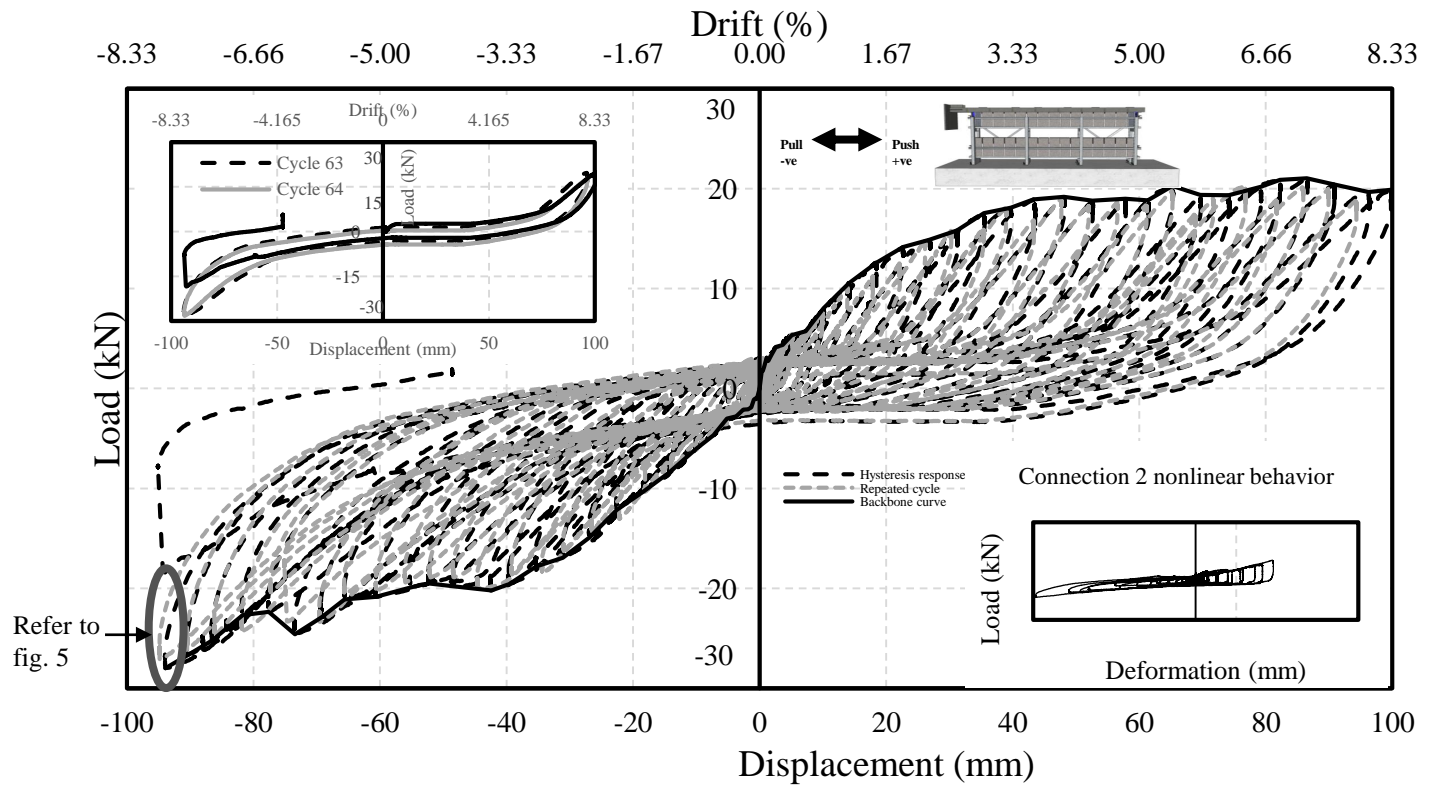
Figure 2.4: Load-displacement response of the rack.

(a)

(b)
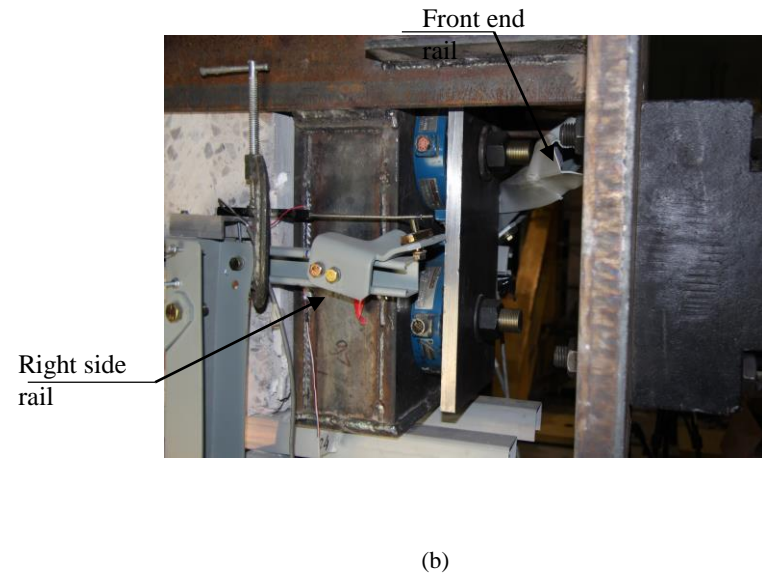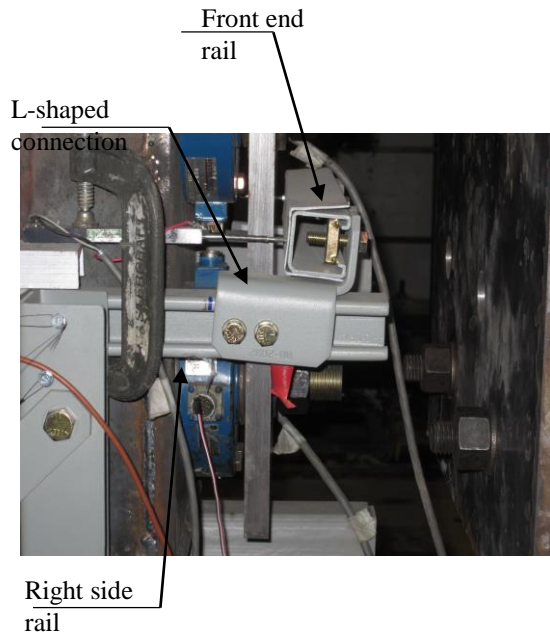
Figure 2.5: End Rail connection deformation: (a) Inelastic rotation of L-shaped connection around sliding nuts to side rail; (b) Failure of end rail.
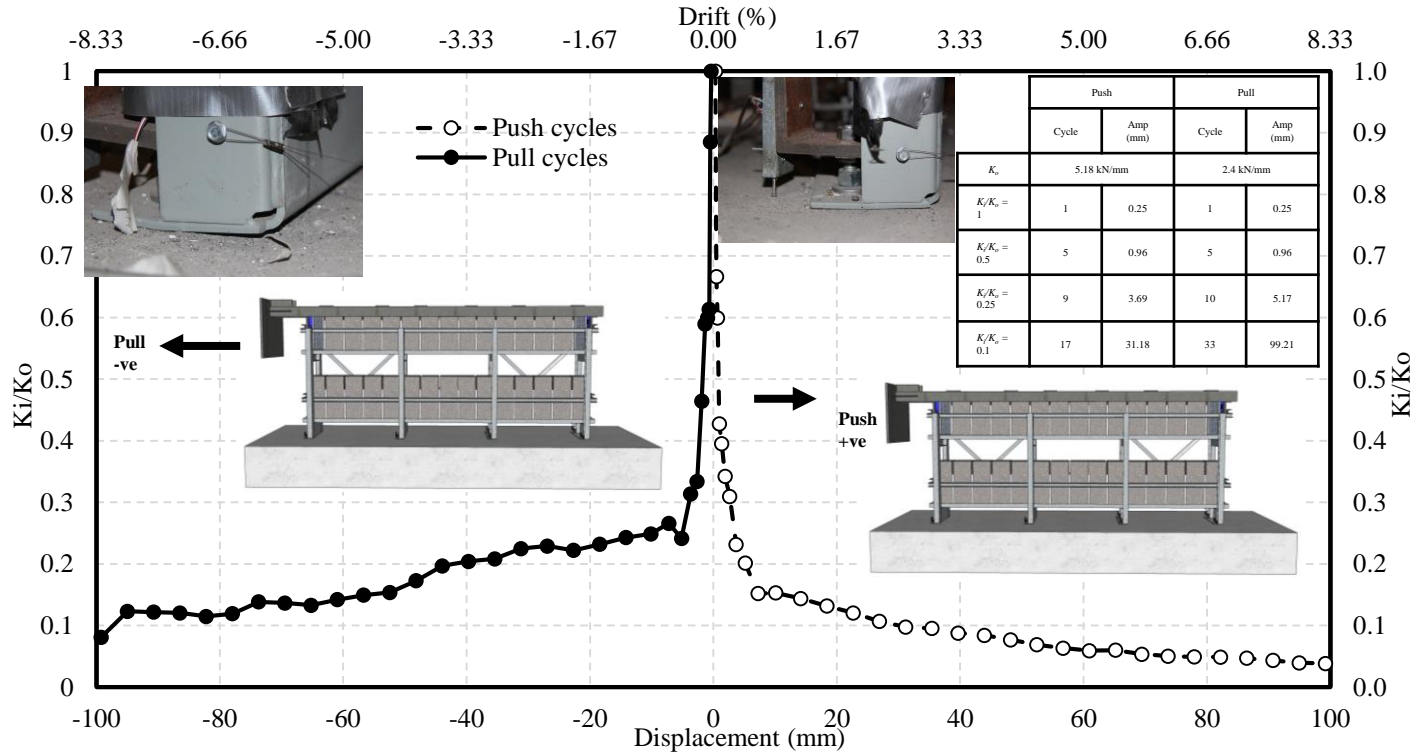
Figure 2.6: Stiffness degradation.
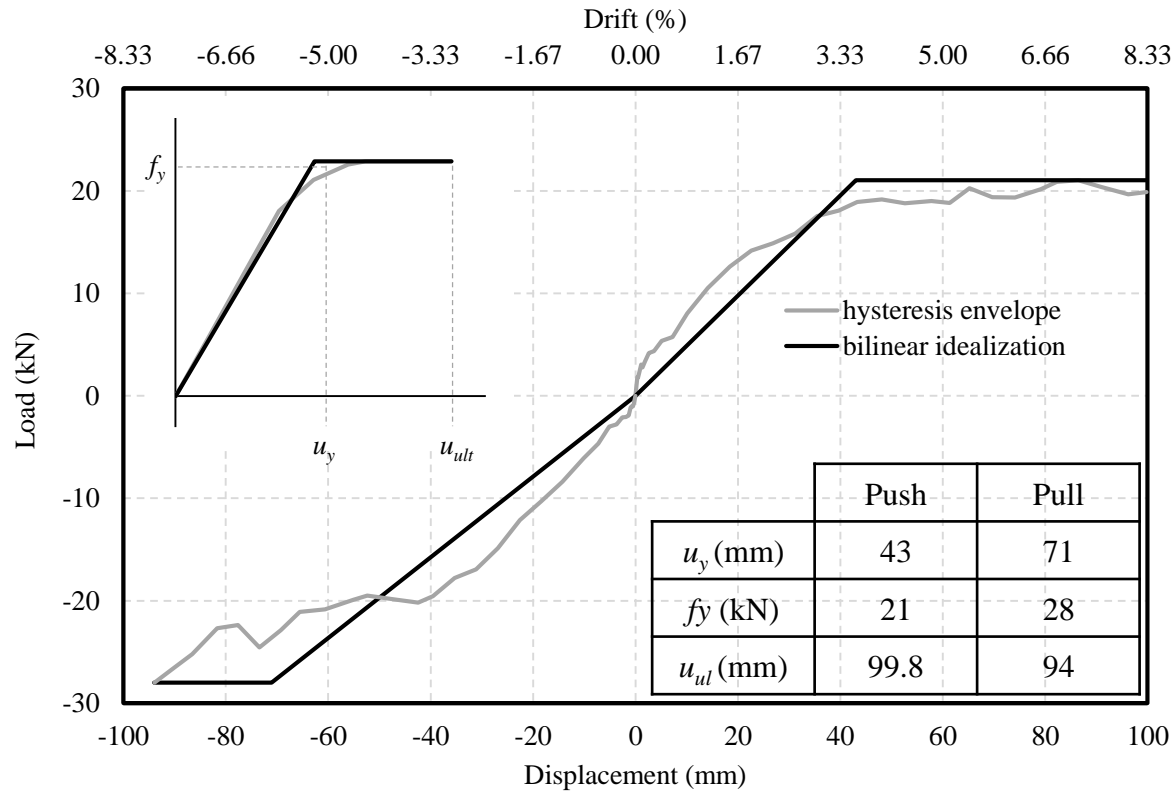
Figure 2.7: Bilinear idealization of the envelope of the hysteretic behavior.
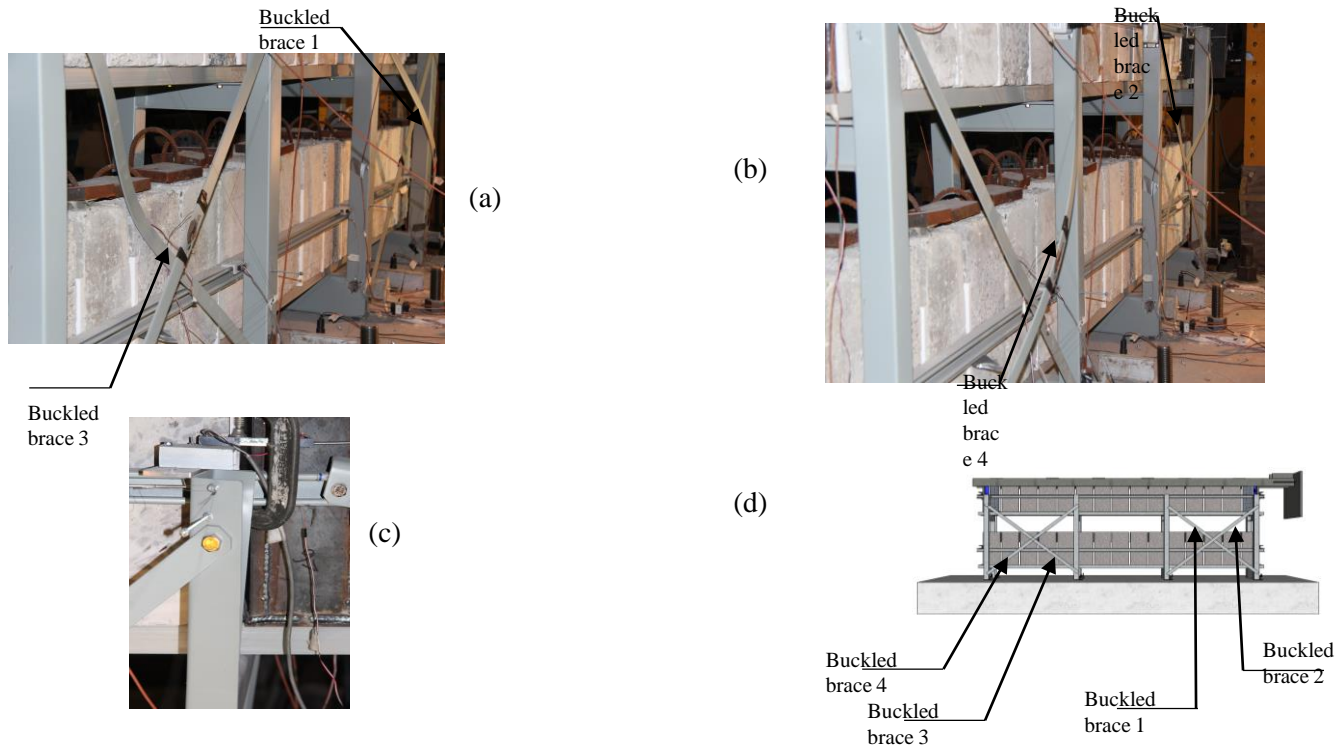
Figure 2.8: Buckling of the braces in compression: (a) buckling of braces 1 and 3; (b) buckling of braces 2 and 4; (c) local torsional deformation of the column; (d) rack braces configuration.
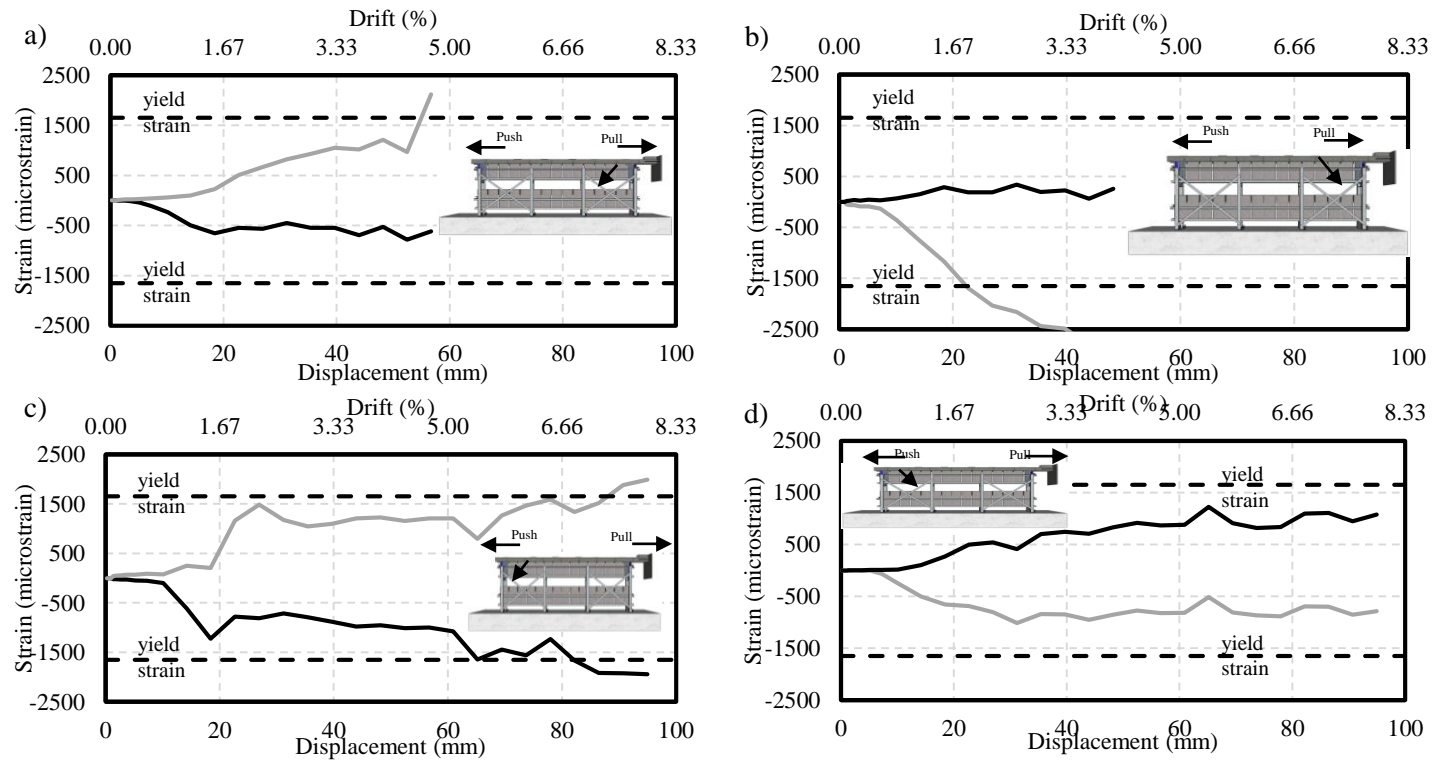
Figure 2.9: Brace strain; (a) brace 1; (b) brace 2; (c) brace 3; (d) brace 4.
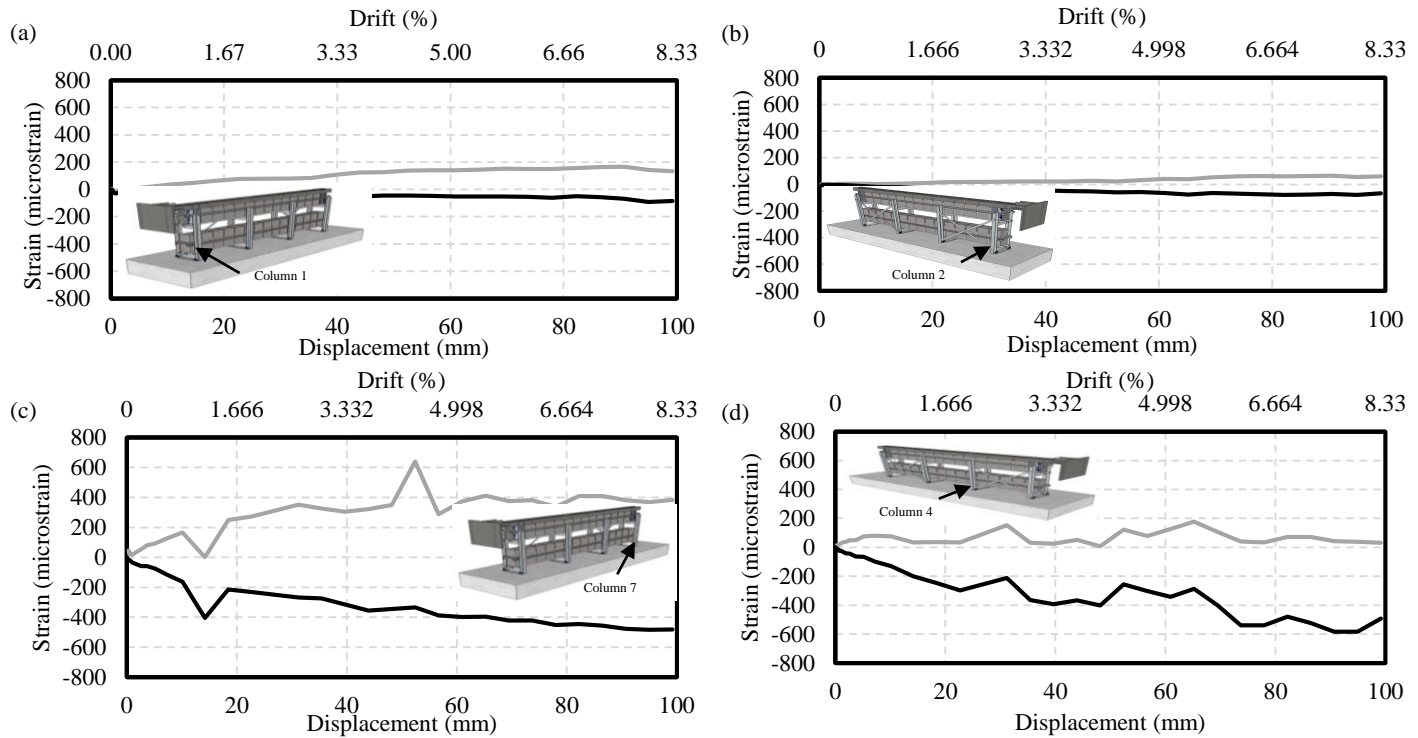
Figure 2.10: Columns strains; (a) column 1 vertical strain; (b) column 2 vertical strain; (c) column 7 horizontal strain; (d) column 4 horizontal strain.
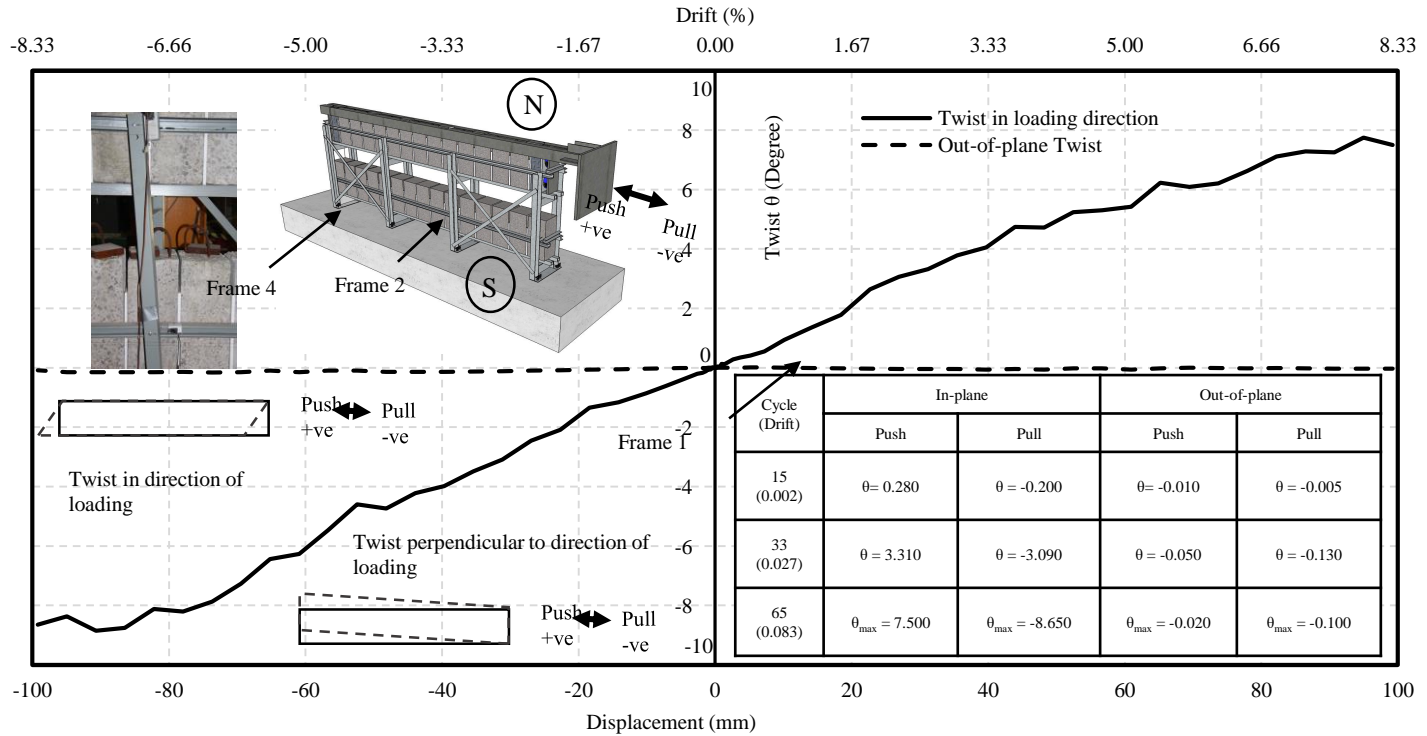
Figure 2.11: Rack twist response.
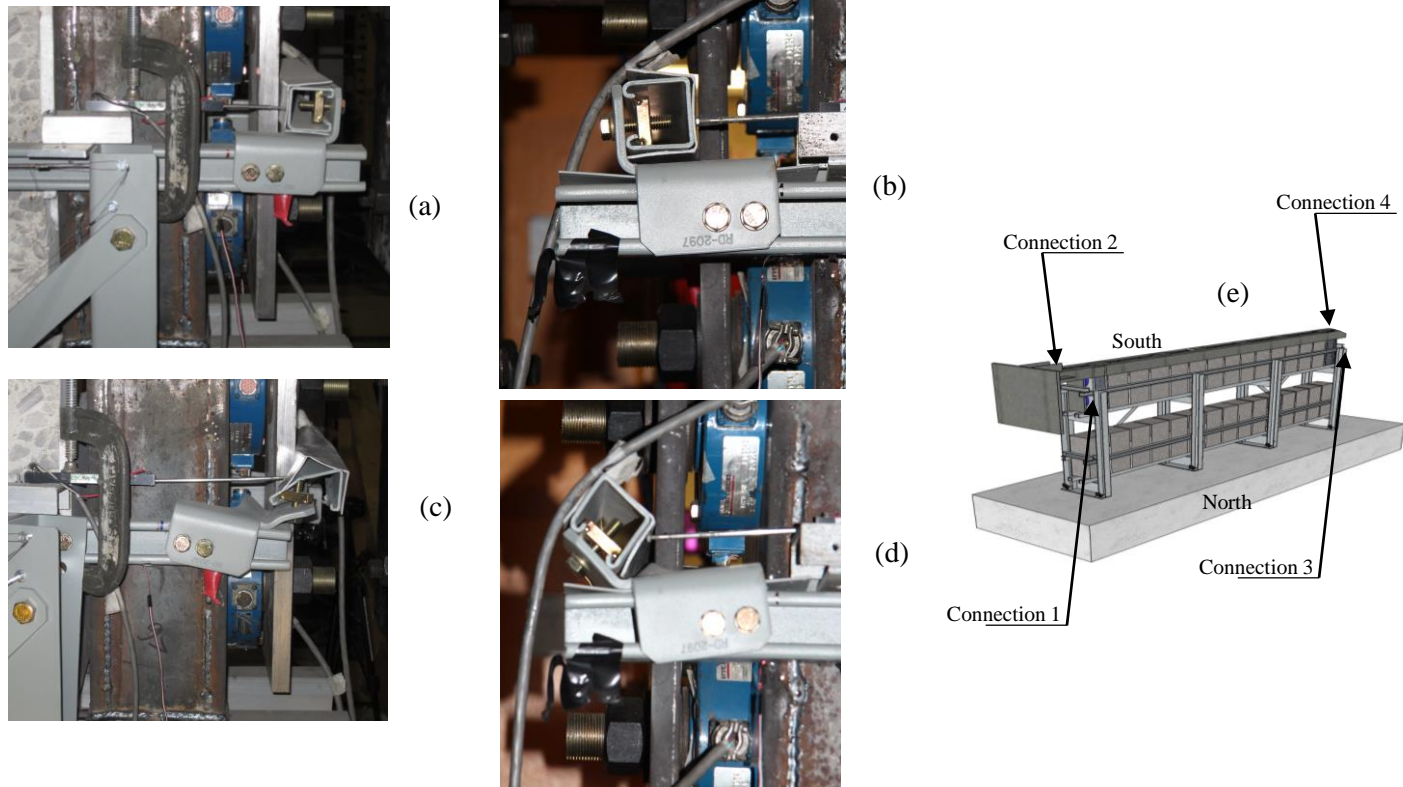
Figure 2.12: Connection deformation in pull; (a) Connection 2 (cycle 15); (b) Connection 2 (cycle 55); (c) Connection 1 (cycle 15); (d) Connection 1 (cycle 55).
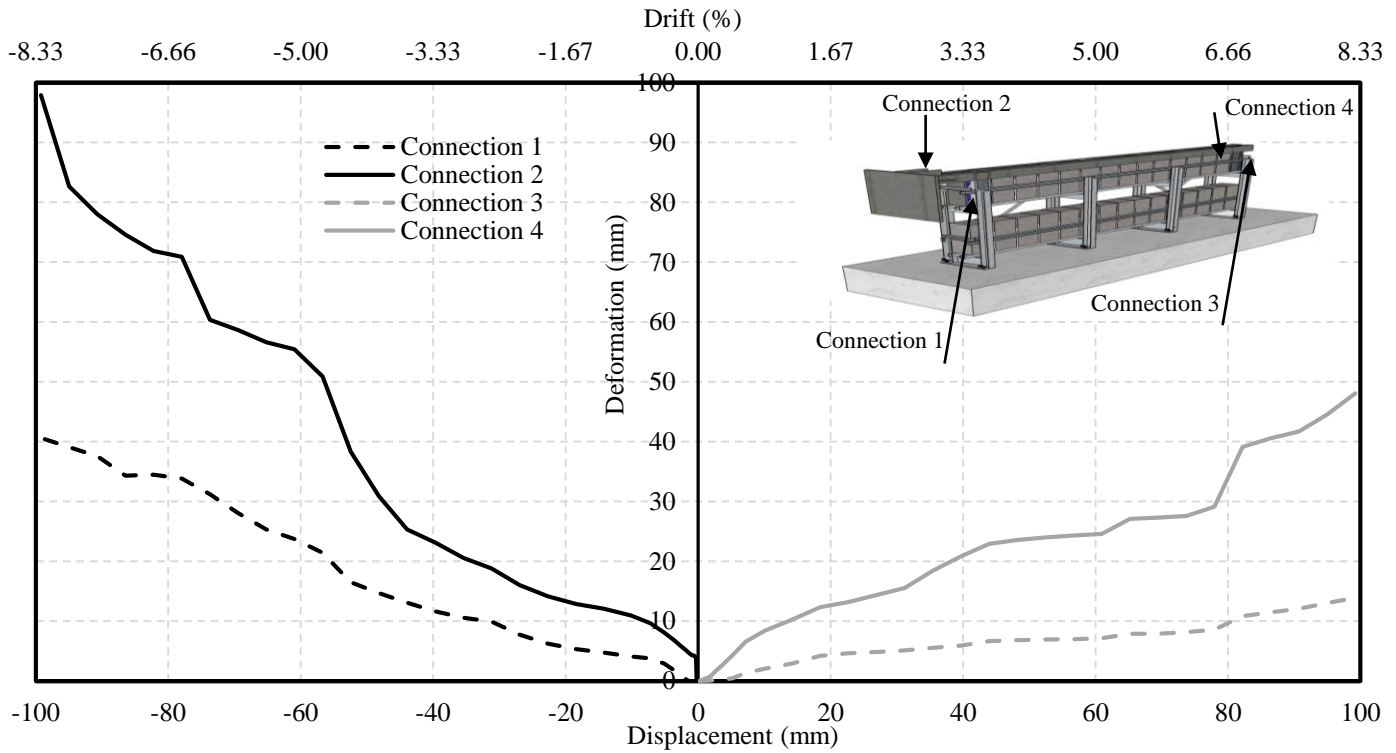
Figure 2.13: End rail deformation.
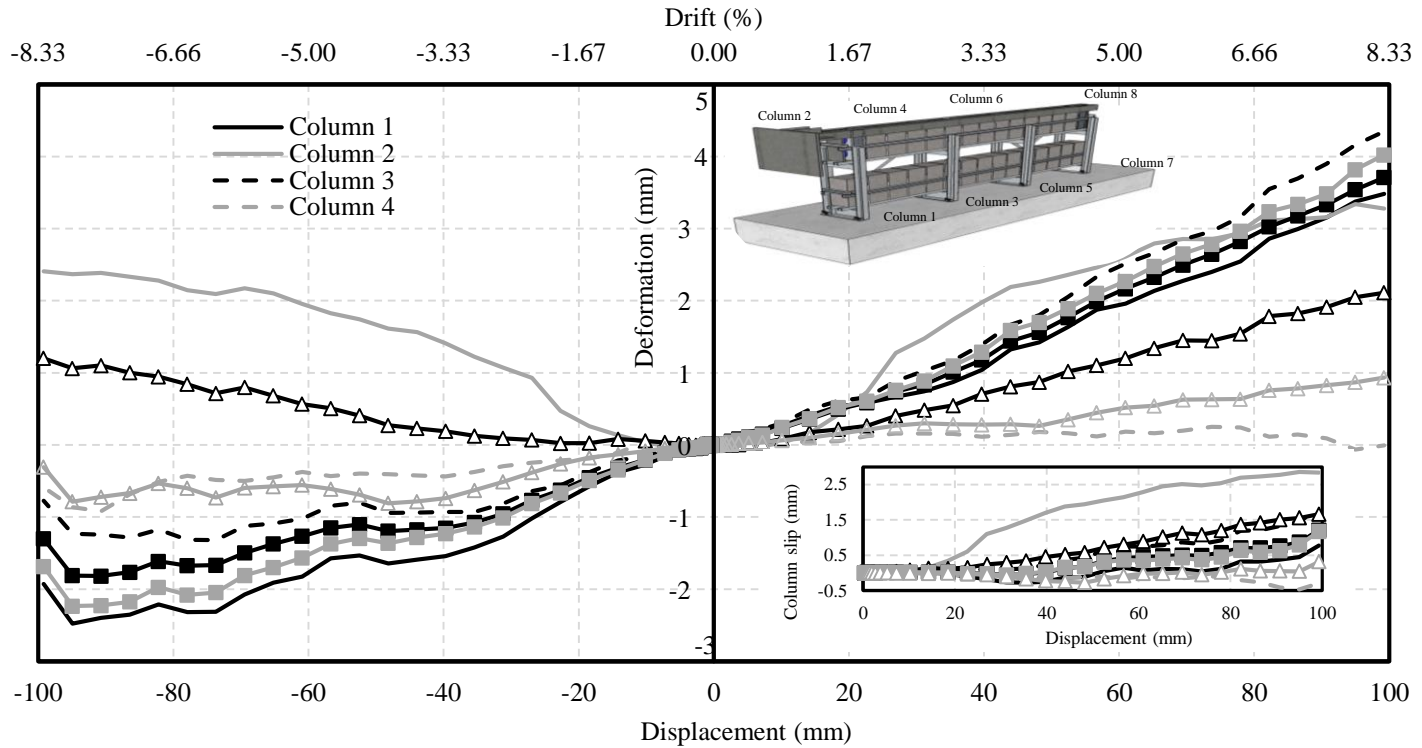
Figure 2.14: Slip deformation at the bottom of the columns.
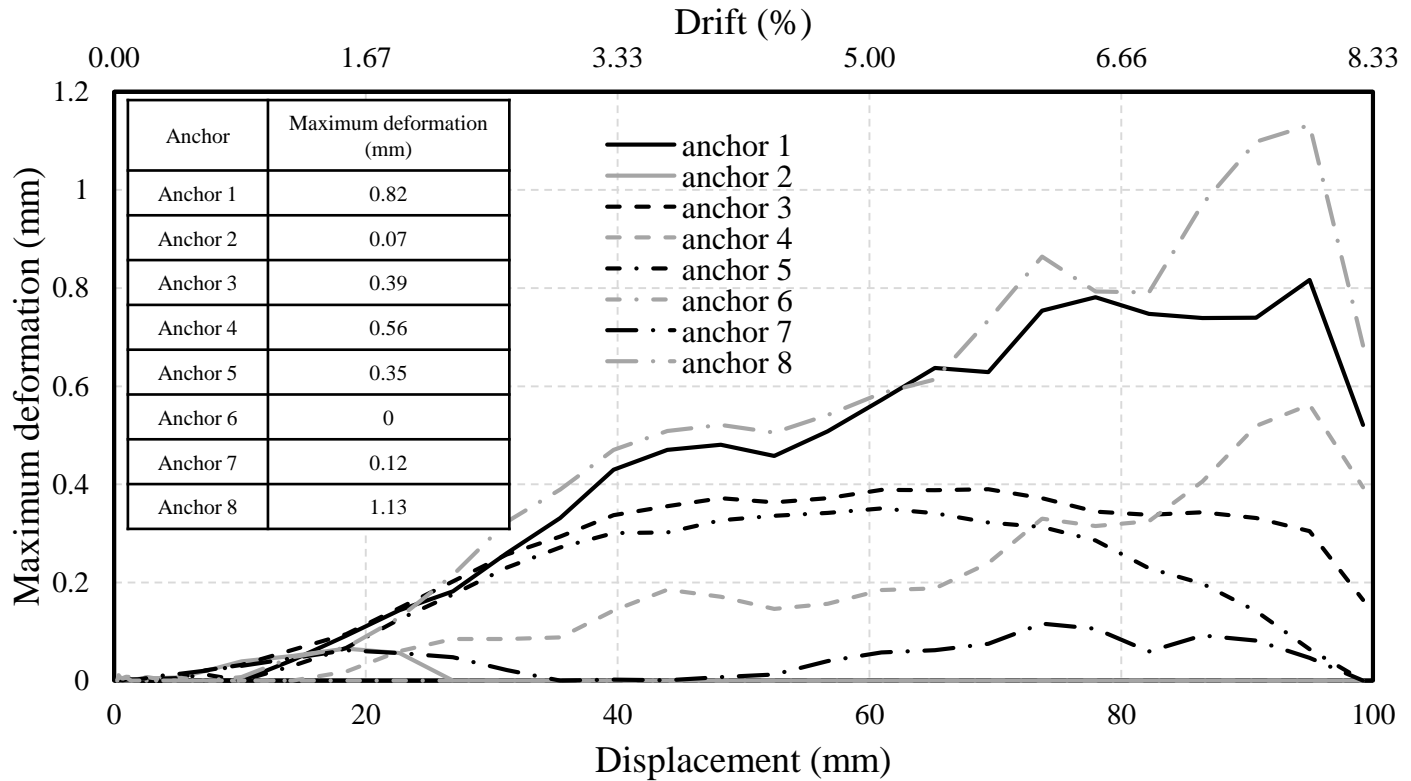
Figure 2.15: Maximum measured anchor tension deformations.
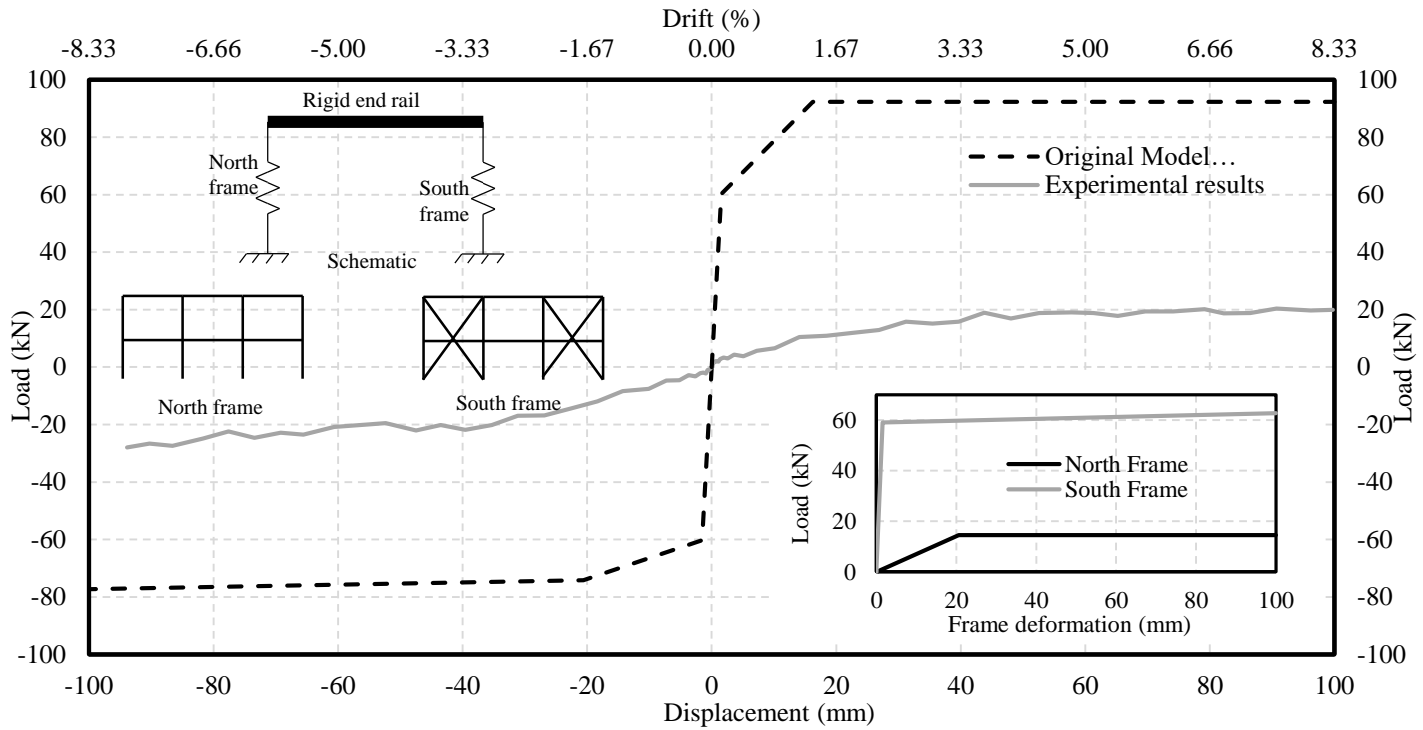
Figure 2.16: Model vs experimental pushover.
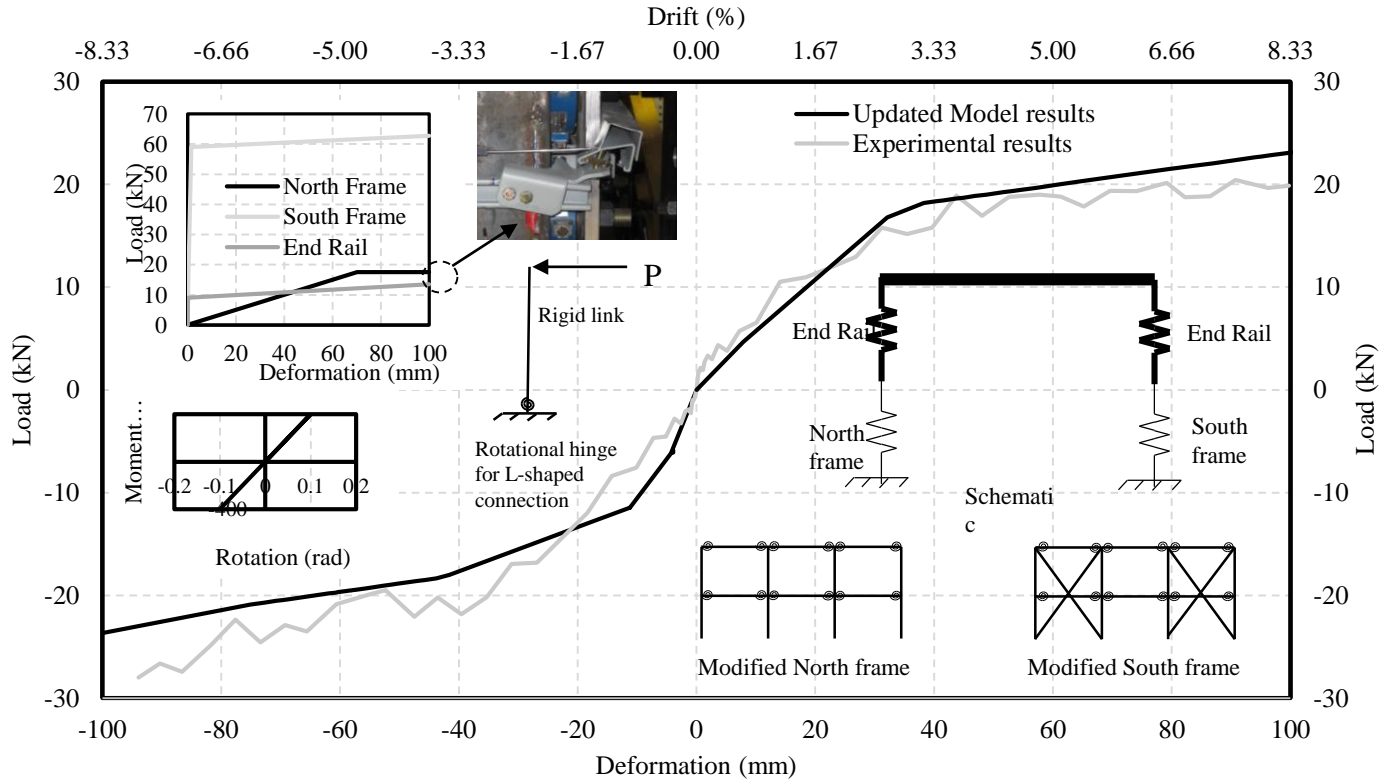
Figure 2.17: Modified model vs experimental pushover.
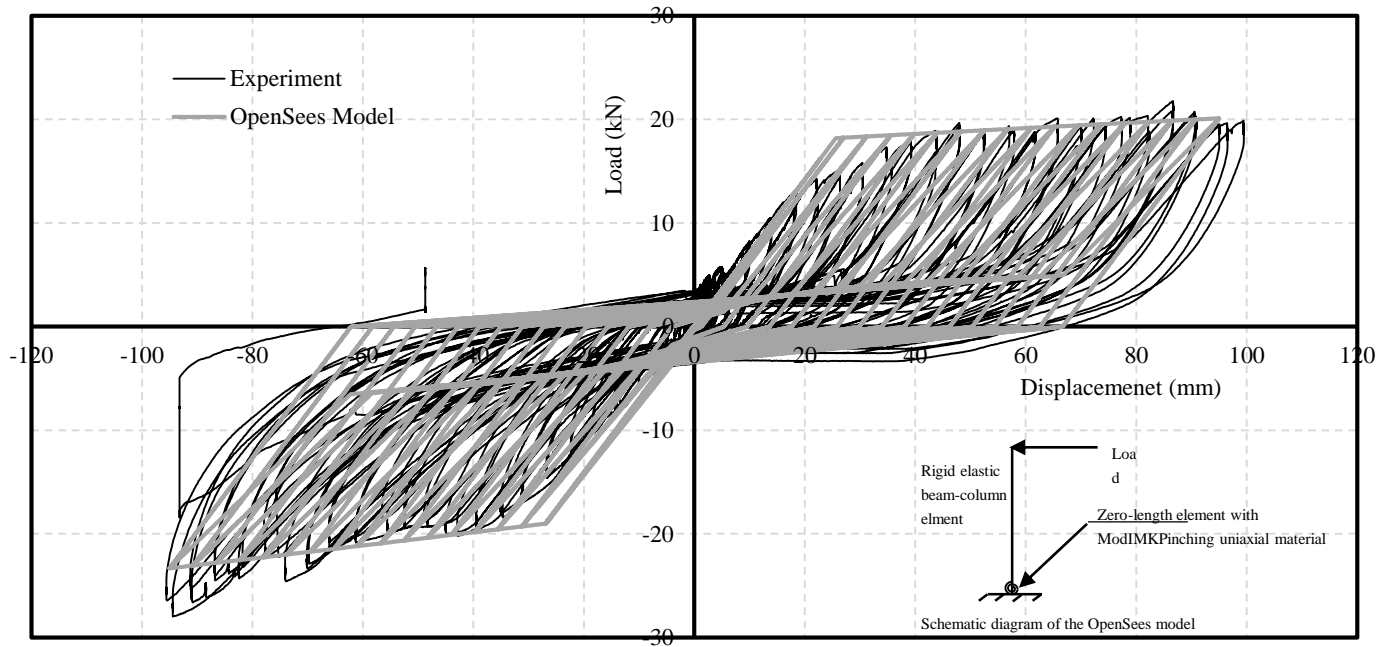
Figure 2.18: OpenSees cyclic response verses the experimental hysteretic behavior.

(a)   (b)   (c)
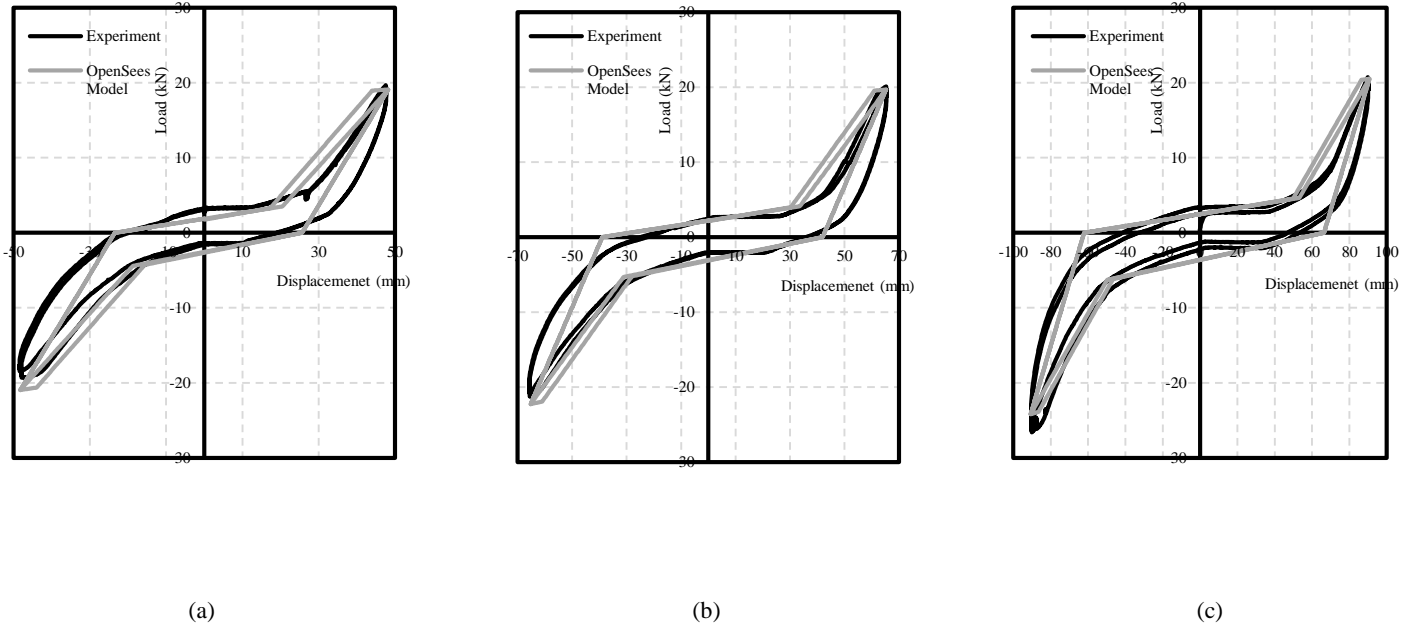
Figure 2.19: Individual OpenSees cyclic response verses the experimental hysteretic behavior for cycles; (a) 41 and 42; (b)49 and 50; (c) 61 and 62.

CHAPTER 3

3. SHAKE TABLE SEISMIC PERFORMANCE ASSESSMENT OF AUXILIARY BATTERY POWER SYSTEMS USING THE FEMA 461 PROTOCOL

3.1. ABSTRACT

Auxiliary batteries and battery rack systems are widely used as a risk mitigation strategy in several critical infrastructure systems to start emergency diesel generators following loss of external power from the grid. Although these systems might fail during earthquakes causing cascading catastrophic economic and life losses, they have received little attention in terms of investigating their seismic performance. However, after recent extreme events (e.g. Fukushima nuclear disaster), such risk mitigation systems have been attracting more attention to ensure their resilience during extreme events. In this respect, this chapter focuses on investigating the seismic performance and modes of failure of battery rack systems that are currently used in several critical infrastructure systems. Shake table tests were performed at different ground motion levels, following the recommendations of the FEMA 461 guidelines, and the experimental results were reported. The results demonstrated that the design guidelines and fragility curves currently assigned to battery rack systems in the FEMA P58 pre-standards do not encompass all possible failure mechanisms. The work in this chapter does not only enlarge the experimental database of the seismic performance of battery rack

systems, but facilitates the adoption of these systems within the next generation of performance-based seismic design standards.

3.2. INTRODUCTION

Structural components (e.g. beams, columns, shear walls, etc.) are the main supporting elements that are responsible for resisting both gravity and lateral (i.e. seismic, wind, etc.) loads, while nonstructural components (e.g. partition walls, mechanical and electrical components, etc.) include all the elements that do not contribute to the load-carrying capacity of the structure (Filiatrault and Sullivan 2014). The performance of these nonstructural (functional) components has been attracting the attention of many researchers and policymakers in the last decade because the damage/loss of such components typically exceeds the cost of the structural systems within the critical infrastructure facilities by a sizable margin, especially for power generation stations (i.e. nuclear power plants) (Whittaker and Soong 2003; FEMA 2012a). For example, many researchers recently studied the seismic response of different nonstructural components to understand their failure modes and subsequently develop ways of mitigation and rehabilitation in an effort to enhance the resilience of the relevant infrastructure (Whittaker and Soong 2003; Kim et al. 2012; Furukawa et al. 2013). In this respect, the seismic performance assessment of nonstructural and functional components represents the new frontiers and the current grand challenge in performance-based seismic design (Filiatrault and Sullivan 2014).

Critical nonstructural electrical components are typically designed to remain functional either after earthquake events such as in essential commercial buildings (i.e. hospitals and emergency centers), or during and after these events such as in nuclear generation stations. For example, auxiliary battery power systems are key components in critical infrastructure (e.g. hospitals, substations, etc.), to ensure infrastructure resilience after the loss of offsite power. In addition to other backup power systems, the auxiliary battery power systems are also used in nuclear power stations to ensure safe operation and accident recovery (i.e. core meltdown and contaminant release). As such, the failure of these components is one of the main contributors to the overall risk of nuclear power stations, which may also lead to catastrophic economic and life losses.

Different types of backup batteries and rack systems are available to supply the required electrical power for critical infrastructure. Relevant research has focused on investigating the seismic performance of these systems within different facilities. For example, Berak (2005) validated a finite element model to simulate the dynamic behavior of different types of batteries and battery racks used in telecommunication infrastructure. In addition, other researchers have investigated the seismic demands on different types of nonstructural components located in different facilities (Parise et al. 2013), and in irregular buildings (Mohammed et. al. 2008). Moreover, Huang et al. (2017) studied the seismic behavior of cable tray systems used in nuclear power stations using shake table testing. The same authors reported that amplification factors currently assigned to these systems were

underestimated in the design code (ASCE 2010). All relevant standards (Telcordia Technologies 2002; IEEE 2005 and 2013) indicate that individual manufacturers are responsible for ensuring that backup batteries and battery rack systems remain functional after a prescribed ground motion level. For this reason, limited independent research has been carried out on the seismic performance of these systems, and subsequently, these systems might still exhibit poor performance during seismic events (Fujisaki et al. 2014).

Fragility curves can be used to quantify the seismic performance of battery rack systems. These curves define the cumulative probability distribution of a component to reach a prescribed damage state based on a demand parameter (e.g. peak ground acceleration). Fragility curves are a useful tool for pre-earthquake design, risk mitigation, and planning (i.e. functionality level) and for post-earthquake damage assessment (i.e. retrofit prioritization, and loss estimation). In the next generations of performance-based design guidelines, fragility curves can be used to ensure that structural and non-structural components reach prescribed performance design objectives (Filiatrault and Sullivan 2014). Fragility curves of nonstructural components have been investigated in previous research studies. For example, Choun et al. (2008) used fragility analysis to evaluate the probability of failure of a nuclear power plant when the seismic capacity of certain safety-related components is enhanced. Huang et al. (2010) also investigated the influence of utilizing base-isolation strategies for certain safety-related components through the use of fragility curves. Recently, Huang et. al. (2017) developed fragility curves for

cable tray systems in a nuclear power plant using shake table results, and subsequently compared these curves to relevant studies (Choun et. al. 2008). Comprehensive review of existing approaches and applications of fragility analysis can be found elsewhere (Zentner et al. 2017). These fragility curves are used within the event tree and fault tree analyses to perform a probabilistic risk assessment (PRA) for NPPs. Such PRA, in turn, is typically utilized to develop the NPP probability of failure in terms of the core damage frequency (CDF).

Other studies (e.g. Choun et al. 2008) demonstrated that batteries and battery rack systems have a major contribution towards the CDF of NPPs. Yet, a limited number of studies to date have been conducted to develop fragility curves for battery rack systems. For example, Johnson et al. (1999) initially introduced fragility curves for batteries and battery racks, which were based on expert opinion and observations following historical earthquakes. More specifically, Johnson et al. (1999) assigned specific mean and dispersion (i.e. standard deviation) values to develop a fragility curve for each in-situ condition (e.g. anchoring, battery restraints, longitudinal bracing, and battery spacers), as shown in Fig. 3.1. This study used an earthquake experience database from different facilities called the Seismic Qualification Utility Group database (SQUG) (2017), a description of this database can be found elsewhere (SQUG 1999). However, the study did not provide a comprehensive description of the observed damages, and whether these damages can be repaired or not. Porter (2009) combined 132 specimens from the SQUG and the Generic Equipment Ruggedness Spectra (GERS) databases (EPRI 1991) to

develop fragility curves that are currently presented in the FEMA P-58 pre-standard background documents (FEMA 2012b). These documents are components of the ATC58 methodology that was developed in an effort to reach the next generation of performance-based seismic design codes and standards (FEMA 2012b). A brief description of the observed damages to the batteries and battery racks was provided in FEMA P-58. More specifically, three dominant failure modes were reported, namely: failure of the anchors, toppling of the battery off the rack with an acid spill, and yielding, and subsequently permanent deformations, of the rack members. Regression analysis was used to develop fragility curves that are not only based on the installation conditions of the rack (i.e. well or deficient installation based on guidelines in FEMA P-58 (2012b)), but also neglected the different damage states and failure modes reported in previous studies (i.e. Johnson et al. 1999). As such, extensive research is still needed to investigate the seismic performance of the available types of batteries and battery racks, because the available fragility curves are primarily based on experience and historical data, as previously discussed.

Two shake table testing protocols are currently available to quantify the seismic performance of nonstructural components. First, the AC156 testing protocol (ICC-ES 2012), developed in compliance with the International Building Code to evaluate the performance of nonstructural components under seismic loading. Second, the FEMA 461 (2007) methodology provides guidelines to both quasi-static and shake table testing protocols for displacement and acceleration sensitive components, respectively, that can be adopted for both structural and

nonstructural components. This study follows the FEMA 461 shake table testing protocol as it has been argued that this protocol provides more compatible estimates to such tested systems (Burningham et al. 2007; Retamales et al. 2011).

The objectives of the current study are to: 1) present the experimental seismic performance results of currently existing/operational batteries and their supporting rack system using shake table testing of a single rack (slice) in the in-plane direction considering the back-to-back installation configuration; 2) directly quantify their seismic performance and the associated acceleration demands at which different damage states occur; and 3) facilitate the development of experimental fragility curves for these existing/operational battery rack systems to allow for a direct comparison with those available in the FEMA P-58 (2012b). In this respect, this chapter first presents a description of the experimental program, test setup, loading protocol, and instrumentation. This experimental program was performed on a shake table located in the Applied Dynamics Laboratory (ADL), McMaster University. Following the experimental program description, this chapter focuses on quantifying the dynamic and hysteretic properties of the rack. Finally, fragility curves are developed based on the experimental results at different damage states. This study aims not only at enlarging the database of the available seismic response of batteries and battery racks, but also at facilitating the adoption of these nonstructural components within the next generation of performance-based seismic design codes and standards.

3.3. EXPERIMENTAL PROGRAM

3.3.1. Prototype Battery and Battery rack

The dynamic behavior of prototype KCR 17 batteries and their supporting battery rack was experimentally investigated using shake table testing. These batteries are high-efficiency backup batteries that are typically used in several critical infrastructure systems to supply and maintain electricity or to trigger the backup generators upon loss of the offsite power (C&D Technologies 2012). In addition, KCR 17 batteries are classified as nuclear-grade backup batteries (C&D Technologies 2012) to be used in nuclear power stations. During the test in this study, the batteries were filled with water instead of acid, as per the laboratory safety requirements, between the recommended minimum and maximum fluid height, to achieve the same battery weight. Therefore, the output voltage of the batteries could not be measured during the test, instead, the movement of the batteries, that might break their conductors and prevent them to remain functional under extreme events, was monitored. Two real batteries and sixteen concrete blocks were used, where the weight (i.e. 65.8 kg) and dimension (217x265x464 mm) of each concrete block were originally determined to represent their corresponding values of a single real battery.

Three types of seismically qualified matching battery racks are available (i.e. EP1, EP2, and EP693) that are all based on the same main steel frame. However, the difference between these racks is the configuration of the bracing and the tie rods used within the side supporting rails (i.e. beams). Figure 3.2 shows the

configuration of the selected EP1 battery rack (RDB 0801-5EP1P), which consists of three tiers and one step. The rack is constructed from different C-channel cross-sections of dimensions 3x3x2x0.13in for the columns (i.e. different flange lengths), 1.64x1.64x0.11in for the longitudinal beams (i.e. side rails and supporting rails), and 3x2x0.13in for the transverse beams. However, all the braces have rectangular cross-sections of dimensions 1.5x0.2 in. Similar to the current study, Johnson et.al. (1999), Porter et al. (2006), and Porter (2009) have shown that back-to-back configuration is typically used in substations and NPPs, as shown in Fig. 3.2. The rack is constructed from steel C-channel cross-sections with various sizes connected via sliding nuts and consists of two braces on each side (i.e. lower and upper bracings). The tested battery rack is currently used in several electrical substations in Ontario, Canada. The only accessible design information states that this system is originally designed to withstand the seismic requirements of the currently outdated UBC 1994 seismic requirements for Zones 1-4 for essential and nonessential buildings, above and below grade, with peak ground acceleration of 0.45g.

3.3.2. Anchoring

The tested battery rack was anchored to a reinforced concrete foundation, designed to act as a rigid floor, using four post-installed anchors to resemble the in-situ conditions, as shown in Fig. 3.2. Undercut type anchors are typically used in most substations and nuclear power plants due to their high performance under dynamic loading (Hilti incorporation 2017). The lateral load demands were

calculated based on the IEEE 693 (2005) to sustain the applied tension and shear forces during the test. Hilti Profis software (Hilti co. 2017) was used to distribute the design loads on the anchors and calculate the capacity of the anchors according to CSA A23.3 (2014). The governing design equation was the combined tensile stress and shear forces, calculated using

$$\frac{N_f}{N_r} + \frac{V_f}{V_r} \leq 1.2 \tag{1}$$

where N_f is the tensile force demand, N_r is the tensile capacity, V_f is the shear force demand, and V_r is the shear capacity. The anchors were designed to fail in a ductile manner, as recommended by IEEE 693 (2005), therefore, N_r and V_r were determined based on the anchor cross-section capacity (i.e. concrete shear and tensile capacity were evaluated to exceed the demand). As such, HAD-P M12*125/30 undercut type anchor was selected during the design stage. Table 1 presents the demands and capacities of the HAD anchor used, while Fig. 3.3 shows the test setup of the rack anchored to the reinforced concrete platform on top of the shake table. The CSA A23.3 (2014) and the manufacturer's recommended guidelines were followed during the installation process.

3.3.3. Instrumentation and Data Acquisition

Three displacement transducers (D1, D2, and D3) and three accelerometers (A1, A2, and A3) were used, at the base of the batteries within each tier, to measure the displacement and acceleration responses of the rack, respectively, as shown in Fig. 3.3. One displacement transducer (D4) was used to measure the displacement

motion of the reinforced concrete platform; this measurement allows a direct comparison with the shake table displacement to ensure that no sliding occurred between the reinforced concrete platform and the shake table during the test. Four displacement transducers (D5, D6, D7, and D8) were mounted on the four columns to measure the vertical deformation of the anchors, where D5 only is shown in Fig. 3.2 for illustration. Due to the unsymmetrical configuration of the bracing within the rack, two additional displacement transducers (D9 and D10) were used to measure the torsional (twist) response of the rack during the test, as shown in Fig. 3.2. Three displacement transducers were also installed on each side of the rack (D11-D13 and to D14-D16) to measure the relative displacement of the end batteries with respect to the rack. As shown in Fig. 3.2, one transducer (D11) was installed at the bottom of the left battery to measure the sliding of the battery on the rack and additional two transducers (D12 and D13) were installed at two-thirds of the left battery height to capture its behavior relative to the end rail. To ensure that the measured strains of the braces are due to axial deformations only, an additional displacement transducer (D17) was used to measure the relative deformation between the endpoints of the bracing, as shown in Fig. 3.3. Two strain gauges were installed on each column (S1 to S8) to measure the vertical and horizontal strains, where Fig. 3.2 shows only (S1 and S2) for illustration. One strain gauge (S9) was used on one column to measure the strain in the transverse horizontal direction. One strain gauge was mounted in the middle of the lower bracing on each side (S10 and S11), as shown in Figs. 2 and 3. Refer to appendix A for a full list of instrumentation

used. Experimental data were collected using a National Instrument compact DAQ type data acquisition system. Data were then filtered using a digital low-pass Butterworth filter implemented in Matlab (Matlab and Statistics Toolbox 2013), having a corner frequency of 30 Hz, as recommended by the FEMA 461 (2007).

3.3.4. Ground Motion Selection and Scaling

FEMA 461 (2007) shake table testing protocol was adopted in this study to evaluate the seismic performance of the tested battery rack. Although biaxial (one horizontal and one vertical) direction testing should be used according to the FEMA 461, the scope of the current study is limited to a uniaxial shake table testing only as the battery rack system combined with the anchors have the sufficient vertical stiffness to avoid any failure due to vertical excitations. More specifically, based on the axial stiffness of the used anchors and the lumped total mass of the rack system, the vertical fundamental frequency was found to be 127 Hz, (i.e. 25 times greater than the horizontal fundamental frequency). Since the vertical fundamental frequency was greater than ten times the horizontal fundamental frequency, the vertical component of the ground motion was neglected in the current study, as recommended by the FEMA 461 (2007). Similar uniaxial shake table testing on nonstructural components has been also performed by other researchers (e.g. Magliulo et al. 2012, Rahmanishamsi et al. 2014, Cosenza et al. 2015). A Matlab (Matlab and Statistics Toolbox 2013) code specified in FEMA 461 (2007), originally developed by Wilcoski et.al. (1997), was used to generate the narrow band random sweep acceleration records. These records were based on

recommended input parameters by FEMA 461, as shown in Table 2. The generated records were then filtered to remove any unwanted low-frequency signal as per the FEMA 461 guidelines. Afterward, a relatively smooth acceleration record was selected and scaled so that the acceleration response spectrum would be approximately 1.0 g above 2 Hz (FEMA 2007). Finally, a high-pass filter was used to remove any low-frequency content arising from numerical integration of the acceleration when the displacement record was evaluated, which was used as the input signal for the shake table. Figure 3.4 shows the good agreement between both generated unfiltered and filtered motions in terms of the acceleration response spectra, S_A, and the frequency, ω, while Fig. 3.5 presents the ground acceleration history of the filtered record used during the test.

The generated filtered ground motion acceleration time history was scaled as recommended by FEMA 461. FEMA 461 described a 25% minimum increase in the spectral demand parameter, taken as the peak ground acceleration (PGA) in the current study. Using spectral acceleration (SA) at the appropriate period, instead of the PGA, better describes the response of the system. However, due to the lack of information regarding the natural frequency shift during testing, SA at the continuously changing natural frequency could not be accurately determined. However, as described in the FEMA 461 guidelines, other ground motion intensity parameters (e.g. PGA) could be used with proper justification. As such, twelve-step experimental incremental dynamic analyses were implemented as suggested by FEMA 461. The initial scale factor (SF) was 0.5 and its corresponding PGA was

0.18g. Table 3 shows the SF_S used along the test history and their corresponding PGAs. Figure 3.6 shows a sample of the input and output table acceleration response spectra for different earthquake levels (i.e. SF=1.53, 3.72, and 4.66). The figure shows that the variation between the input and output PGA values was only 3.5% and 8.5% at SF = 1.53 and 3.72, respectively. However, this variation reached 38% by SF = 4.66 due to specimen-table interaction (Nagarajaiah et al. 1992, Roussis and Constantinou 2005, Luo et al. 2014). For this reason, the output acceleration history of the table has been used throughout the current study. The experimental testing procedure was terminated at *SF=5.82* with corresponding PGA of 2.44g for laboratory safety reasons.

It is worth mentioning that the current study focuses on the effects of damage propagation and the severity of a currently existing/operational battery rack system. More specifically, this rack was subjected to a progressively increasing intensity applied by a shake table. This enabled an investigation of the behavior of the rack in various accumulated damage states. As such, within the objective of the current study, the rack components (e.g. braces) were not replaced after each test, and instead, all the rack component responses and their corresponding cumulative damages were recorded (e.g. Mosqueda et al. 2009; Wang et al. 2015; Huang et al. 2017).

3.4. RESULTS AND DISCUSSION

The evaluation of the natural frequencies after each testing level and observing the shift in these frequencies give an indication of the damage, rather than the type of damage, and the extent of such damage per se. More specifically, previous studies (e.g. Salawu 1997) demonstrated that natural frequency changes alone may not be sufficient for identification of the location of structural damage. For example, cracks associated with similar crack lengths but at two different locations may cause the same level of frequency shift. Instead, the indication of damages in the current study was evaluated using other indices such as stiffness degradation, ductility, member strains, and joint deformations, as will be discussed in the current section.

3.4.1. Dynamic Properties

Two experimental tests were performed to determine the natural frequency and damping ratio of the battery rack system. First, a simple and effective method to find these dynamic properties (i.e. frequency and damping ratio) is the tap test, also known as the hammer test (Wittich and Hutchinson 2015). In this method, the free vibration decay motion was recorded, and subsequently, two non-sequential peaks and the number of cycles between them were analyzed to evaluate the dynamic properties, following the procedure outlined in Chopra (2007). KP and Hirani (2014), Yan et al. (2014), and Di Sarno and Manfredi (2012) have used a similar procedure. Figure 3.7 shows the decay acceleration response, A_R, measured

at the top of the rack during the tap test versus the time. The natural period and the damping ratio of the system were approximately 0.19 s, and 1.5%, respectively. Second, these dynamic properties were verified with a nondestructive band limited low amplitude white noise test. The root-mean-square of the generated white noise was within the limits (i.e. 0.05±0.01g) suggested by FEMA 461 (2007). Fig. 3.8 shows the Power Spectral Density (PSD) of the measured response at the top of the rack in the frequency domain. The first peak in the curve represents the natural frequency of the system, ω_n, that was approximately 4.5 Hz (i.e. natural period=1/frequency=0.22 s).

3.4.2. Rack Response

The rack response in the direction of loading was measured using three displacement transducers at each tier level, as shown in Fig. 3.3. Fig 9 shows the maximum response of the rack in both directions of loading (i.e. North and South) at each tier level relative to its base at different earthquake levels (i.e. $SF = 2.98, 3.73$ and 4.66), while Table 3 shows the damage observed within the rack at key levels of shaking. As shown in Fig. 3.9, the response at the bottom of the rack was higher at SF=3.73 compared to that at SF=4.66. This could be contributed to the system hardening at intermediate level scale factors compared to higher counterparts, as discussed by Vamvatsikos and Cornell (2002). As shown in Fig. 3.9 and Table 3, the response at the top of the rack increased as the testing progressed reaching a maximum deflection of 24 mm at *SF=4.66*. This rack

deflection exceeds the maximum allowable deflection (i.e. 20 mm for ultimate loading conditions) assigned to category (A) or (III), specified by FEMA 450 (2004), and ASCE 113 (2007). These design guides, provided by ASCE and FEMA, respectively, are considered as comprehensive resources for the investigation of the structural integrity of nonstructural electrical components in substations (FEMA 2004, ASCE 2007).

The steel members of the rack were connected by sliding type nuts torqued according to the manufacturer's recommended values before the test. However, it was observed during the test that the sliding nuts connecting columns to side rails slipped and locked leading to a decrease in the relative distance between columns decreasing the distance between bracing endpoints. This decrease led to permanent buckling of the braces in compression, as shown in Figs. 10 a and b for both front and back lower braces, respectively. According to the substation design guide ASCE 113 (2007), this battery rack is considered non-functional at $SF=1.53$, when permanent buckling of the lower bracing and subsequently permanent and residual deformations were first observed at a maximum acceleration response of 1.22g.

3.4.3. Effective Stiffness Degradation

The effective secant stiffness, K, determined from the load-displacement response of the inelastic structure at the design level of top displacement, has been adopted for displacement-based design (Priestley et al. 2007). To assess the stiffness degradation of the rack system as the scale factor (i.e. earthquake level)

increased, the effective secant stiffness was calculated as the ratio between the total

base shear and the corresponding prescribed top drift ratio (i.e. 0.1%). The total

base shear was calculated as the total inertia forces (i.e. the multiplication of the

mass at each tier with the corresponding total measured acceleration). Figure 3.11

presents the variation of the effective secant stiffness (K_i) normalized to the secant

stiffness at $SF=0.5$ (K_o), with respect to different earthquake levels. This figure

clearly demonstrates the progressive damage within the battery rack system. For

example, as can be seen in Fig. 3.11, the secant stiffness of the rack system was

reduced approximately by 50% and 20% at $SF=0.63$ and $SF=0.78$, respectively.

Afterward, the secant stiffness remained around 15% of its counterpart at $SF=0.5$,

until $SF=2.98$. This significant reduction in the effective stiffness is mainly

attributed to the slippage of nuts connecting steel members of the rack, as

previously discussed.

3.4.4. Energy Dissipation

Another key factor of quantifying the damage in structural and nonstructural

components is the energy dissipation, E_d (Park and Ang 1985; FEMA 2012b),

because it reduces the ductility and strength demands of the structure. The energy

dissipation, E_d, was calculated in the current study as the area under the force and

displacement relationship (Chopra 2007). Figure 3.12 shows the energy dissipation

for each scale factor (E_d) normalized to the energy dissipation at, $SF=0.5$, E_{do}.

Energy dissipation was normalized to monitor the trend of increase of energy

dissipation after yielding of the rack steel members to evaluate the damage that occurred as the test progressed. As can be seen in Fig. 3.12, as expected, for low ground motion levels, the energy dissipation was low which characterized the behavior of the batteries and battery rack system before significant inelastic deformation had taken place. For higher ground motion levels, the energy dissipation increased significantly compared to lower ground motion levels.

3.4.5. Strain Response

The rack consisted of lower and upper bracing on both sides as previously mentioned and shown in Fig. 3.3. During the test, the midpoint strain variation of each brace within the rack was monitored using a strain gauge. Fig. 3.13 shows the midpoint strain variation of the lower brace at different scale factors. As can be seen in Figs. 13 a and b, the strain of the lower bracing increased as the experimental testing progressed until *SF=1.22*. However, slippage of the nut at *SF=1.53* led to yielding of the lower brace in tension, and subsequent residual deformations within the same brace, as can be seen in Figs. 13 c and d. In addition, the strains were also calculated by dividing the relative deformation between the brace ends by the brace length. This relative deformation was measured during the test using displacement transducers, as previously mentioned. Figure 3.14 shows the peak strains of both measured and calculated strains normalized to the yield strain. As shown in Fig. 3.14, excessive decrease between the brace endpoints eventually led to higher calculated compressive strains than their measured counterparts.

3.4.6. Battery Movement

Batteries were installed in this study as per the manufacturer's recommendations. More specifically, the middle batteries were installed first on supporting rails, made of C-channel cross-sections, at the bottom level, and then spacers were provided between batteries until reaching the end batteries. Subsequently, end rails were installed to prevent batteries from sliding off the rack. Finally, another two side rails in the direction of loading were installed at approximately two-thirds of the battery height, as shown in Fig. 3.2.

The relative deformations between the batteries and the rack were monitored using three displacement transducers. The two-dimensional dynamic behavior of the battery in the direction of loading was investigated since there was no room for the battery to move in the transverse direction. As such, the battery was considered as an unattached/unanchored rigid body that was free to slide and/or rock in the longitudinal direction but was restrained from rocking and/or sliding in the rack transverse direction. Figure 3.15 shows the peak measured displacements of left and right batteries, as the configuration shown in Fig. 3.3. As expected, peak displacements of the batteries were low at low ground motion levels (i.e. below $SF=1.53$). However, for higher ground motion levels, peak displacements of batteries increased significantly. At $SF=3.73$, the spacing between batteries at the top tier along the direction of loading was approximately 25mm. This significant increase in the relative spacing between batteries would potentially cause the

breaking of their conductors and prevent them to remain functional under extreme events (Porter et al. 2006).

The maximum measured displacement of batteries was approximately 10 mm, although the maximum allowable clearance in all the batteries before the test was 2.5 mm, as recommended by the manufacturer. This is mainly attributed to the permanent rotation that the end rail experienced due to its pounding with the batteries during the test. Figure 3.16a shows the permanent rotation of the end rail at *SF=4.66*, while Figure 3.16b presents the subsequent increase in the clearance between the batteries due to this permanent rotation. As shown in Fig. 3.16, the end rail had no clearance in the supporting rail to move, the next scaled ground motion might have caused the rail to come out and the battery to drop.

3.5. FRAGILITY ANALYSIS

This chapter presents preliminary fragility curves based on the experimental results of the tested rack system following the EPRI (2002) methodology. This standardized methodology is adopted as it is intended for such components with limited experimental tests. Although similar fragility curves were developed by Huang et al. (2017) for cable tray systems in nuclear power plants, the current study utilizes its developed preliminary fragility curves only to allow for a direct comparison with those available in the FEMA P58 assigned to battery rack systems. The probability of failure p_f is given by:

$$p_f = \Phi\left[\frac{1}{\beta_c} ln\left(\frac{a}{A_m}\right)\right] \qquad (2)$$

$$\beta_c = \sqrt{\beta_R^2 + \beta_U^2} \qquad (3)$$

$$A_m = \frac{TRS_C}{RRS_C} F_D F_{RS} PFA \qquad (4)$$

where Φ is the cumulative standard Gaussian normal distribution, a is the base acceleration. According to EPRI 2002, β_C is the total variability, β_R represent the random variability of the ground motion characteristics and the corresponding response of the rack, and β_U represents the uncertainty associated with the material properties, modeling approximations, and design code requirements. TRS_C and RRS_C are the target and required response spectra respectively, F_D is the component capacity factory that describes the functional requirements of the component during and after testing with or without deficiencies, F_{RS} is the structural response factor that indicates to the behavior of the structure at the location of the component, and PFA is the peak floor acceleration, or the peak base acceleration (PBA) for the shake table testing. To evaluate the probability of failure, the PBA (peak [table top] base acceleration) of the ground motion that caused the prescribed damage state. FEMA 461 recommended the use of SA as the ground motion intensity measure unless proper justification is provided. As such, PBA was used in the current study as a ground motion intensity measure to facilitate a direct comparison with those fragility curves provided in FMEA P-58. According to the EPRI (2002) methodology, to develop these preliminary fragility curves, some experimental

responses (e.g. peak floor acceleration) at which the damage state occurs are used, while other parameters (FRS, FD, βU, βR, and βC) are given in the EPRI 2002 due to the lack of substantial amount of data, as shown in Table 4 for different damage states. EPRI 2002 recommended also β_R values to be used with limited experimental testing to develop the fragility curves.

The experimental observations show four damage states; the first damage state (DS1) is the slippage of the nut connecting columns to side rails, the second damage state (DS2) is the yielding of the lower brace, the third damage state (DS3) is the breakage of the conductor due to excess relative movement between batteries (Porter et al. 2006), and finally the fourth damage state (DS4) is when the top of the rack response exceeds the allowable limits.

Figure 3.17 shows the developed fragility curves for the four damage states DS1, DS2, DS3, and DS4. The fragility curves provided in FEMA P58 (FEMA 2012b) for the well and deficient installation conditions are also shown in Fig. 3.17 to facilitate a direct comparison. As can be seen in Fig. 3.17, FEMA P58 (2012b) deficient installation condition (defined as racks with no battery spacer, no anchorage, no restraints, and no longitudinal cross braces) is more fragile than damage states DS1, and DS2, while FEMA P58 (2012b) well installation condition is neither more fragile than DS3 nor less fragile than DS4. For example, the rack system had median base acceleration values of 1.17g, 1.17g, 1.46g, and 4.74g at DS1, DS2, DS3, and DS4, respectively, while the corresponding values for FEMA P58 deficient and well installation conditions are 1.11g, and 2.32g, respectively.

This is mainly attributed to the slippage and locking of the sliding-nuts that were observed within the rack in this study.

3.6. CONCLUSIONS

This study investigates the dynamic behavior and failure mechanism of auxiliary batteries and their supporting rack systems that are currently being used in several critical infrastructure systems. The findings of this chapter will be incorporated as a part of a major research scope to eventually develop fragility curves, under well-controlled testing conditions, for different types of batteries and battery rack systems. In this respect, a widely-used prototype battery KCR17 and its supporting rack system were tested on a shake table with all the in-situ conditions using the FEMA 461 guidelines. The rack response, battery movements, stiffness degradation, energy dissipation, and strain response were presented to assess the seismic performance of batteries and the battery rack system. Finally, fragility curves at different damage states were developed based on modes of failure observed during the test and compared to their current counterparts in FEMA P-58.

Slippage of the nuts connecting columns to side rails was the dominant mode of failure. More specifically, these nuts slipped and locked leading to a decrease in the relative distance between columns and subsequent buckling of the brace. Excessive buckling of the brace eventually led to permanent and residual deformations. These deformations contributed to a significant reduction in the effective stiffness of the rack system and subsequent increase in the energy

dissipation at high ground motion levels. In addition, permanent rotations of end rails were observed during the test leading to excessive movement of batteries that might break their conductors and prevent them to remain functional under extreme events. Finally, the developed fragility curves demonstrated that their counterparts in FEMA P-58 currently assigned to these rack systems may be unconservative and may require revision. This lack of conservatism might be attributable to the limited number of experimental studies at the time when FEMA P-58 was being developed.

Although the current study focused only on a single existing battery rack system subjected to the same progressively increasing seismic motion, additional experimental tests or parametric studies through validated models, considering several rack configurations, sizes, materials, joints/connections, support conditions, gravity loads, loading patterns and protocols, are still needed to facilitate a better understanding of the behavior of battery rack systems that will, subsequently, facilitate adoption of these nonstructural components within the next editions of relevant standards and design codes.

3.7. ACKNOWLEDGMENT

program. Special thanks go to the McMaster University Applied Dynamic Laboratory (ADL) staff.

3.8. REFERENCES

American Society of Civil Engineers (ASCE). (2007). "Substation Structure Design Guide." ASCE 113.

American Society of Civil Engineers (ASCE) (2010). "Seismic design loads for buildings and other structures." ASCE/SEI 7-10, Reston, VA:

Berak, E., & Marconi Communications. (2005). "Modal testing and finite element analysis of a battery rack for seismic applications." *Journal of the IEST*, 48(1).

Burningham, C., Mosqueda, G., & Saavedra, R. (2007). "Comparison of seismic fragility of free-standing equipment using current testing protocols and recorded building floor motions." *Earthquake Engineering Symposium for Young Researchers*. Seattle, Washington.

C&D Technologies. (2012)." KCR Lead- calcium and KAR Lead antimony for switchgear and control applications." C&D Technologies.

C&D Technologies Inc. (2017). Retrieved from http://www.cdtechno.com/

Canadian Standards Association (CSA). (2014). "Design of concrete structures.", *CSA A23.3-14*.

Canadian Standards Association (CSA) (2014). "Seismic risk reduction of operational and functional components of buildings", CSA S832-14.

Chopra, A. K. (2007). "Dynamics of Structures: Theory and Applications to Earthquake Engineering." *3rd edition. Upper Saddle River, N.J: Pearson/Prentice Hall*.

Choun, Y. S., Choi, I. K., and Seo, J. M. (2008). "Improvement of the seismic safety of existing nuclear power plants by an increase of the component seismic capacity: A case study." *Nuclear Engineering and Design*, 238(6), 1410-1420.

Cosenza, E., Di Sarno, L., Maddaloni, G., Magliulo, G., Petrone, C., & Prota, A. (2015). "Shake table tests for the seismic fragility evaluation of hospital rooms." *Earthquake Engineering & Structural Dynamics*, 44(1), 23-40.

Electric Power Research Institute (EPRI) (1991). "Generic Seismic Ruggedness of Power Plant Equipment." *EPRI NP-5223-SL Revision 1*, Oakland, CA.

Electric Power Research Institute (EPRI). (2002). "Seismic fragility application guide." *EPRI Rep. No. TR-1002988*, ABSG Consulting, Irvine, CA.

FEMA (2004), "NEHRP recommended provisions for seismic regulations for new buildings and other structures", FEMA 450.

FEMA. (2007). "Interim testing protocols for determining the seismic performance characteristics of structural and nonstructural components." *FEMA 461*.

FEMA. (2012a). "Reducing the Risks of Nonstructural Earthquake Damage- A Practical Guide." *FEMA E-74*.

FEMA. (2012b). "Seismic performance assessment of buildings." *FEMA P -58*, Washington, DC.

Filiatrault, A., & Sullivan, T. (2014). "Performance-based seismic design of nonstructural building components: The next frontier of earthquake engineering." *Journal of Earthquake Engineering and Engineering Vibration*, pp. 17-46.

Fujisaki, E., Takhirov, S., Xie, Q., & Mosalam, K. (2014). "Seismic Vulnerability of Power Supply: Lessons Learned from Recent Earthquakes and Future Horizons of Research." *9th International Conference of Structural Dynamics*. Porto, Portugal.

Furukawa, S., Sato, E., Shi, Y., Becker, T., & Nakashima, M. (2013). "Full-scale shaking table test of a base-isolated medical facility subjected to vertical motions." *Journal of earthquake engineering and structural dynamics*, vol. 42, pp.1931–1949.

Hilti co. (2017). Hilti PROFIS anchor application, version 2.6.5.

Hilti incorporation. (2017). Retrieved May 19, 2016, from https://www.hilti.ca/anchor-systems/undercut-anchors/r1191#features-applications

Huang, Y. N., Whittaker, A. S., and Luco, N. (2010). "Seismic performance assessment of base-isolated safety-related nuclear structures." *Earthquake Engineering & Structural Dynamics*, 39(13), 1421-1442.

Huang, B., Lu, W., and Mosalam, K. M. (2017). "Shaking Table Tests of the Cable Tray System in Nuclear Power Plants." *Journal of Performance of Constructed Facilities*, 31(4), 04017018.

ICC-ES. (2012). "Acceptance criteria for seismic qualification by shake table testing of nonstructural components and systems." *International Code Council Evaluation Service*, International Code Council AC156, Whittier, CA.

IEEE. (2013). "IEEE Standard for Qualification of Class 1E Vented Lead Acid Storage Batteries for Nuclear Power Generating Stations." *IEEE 535*.

IEEE (2005). "IEEE Recommended Practice for Seismic Design of Substations." *IEEE Std 693*.

Johnson, G. S., Sheppard, R. E., Quilici, M. D., Eder, S. J., & Scawthorn, C. (1999). Seismic reliability assessment of critical facilities: A handbook, supporting documentation, and model code provisions.

Kim, M., Choi, I.-K., & Seo, J.-M. (2012). "A shaking table test for an evaluation of seismic behavior of 480 V MCC." *Journal of Nuclear Engineering and Design*, pp. 341-355.

KP, L., & Hirani, H. (2014). "Stiffness and damping coefficients for rubber mounted hybrid bearing*." Lubrication Science*, 26(5), 301-314.

Luo, J., Wierschem, N. E., Hubbard, S. A., Fahnestock, L. A., Quinn, D. D., McFarland, D. M., ... & Bergman, L. A. (2014). "Large-scale experimental evaluation and numerical simulation of a system of nonlinear energy sinks for seismic mitigation." *Engineering Structures*, 77, 34-48.

Magliulo, G., Pentangelo, V., Maddaloni, G., Capozzi, V., Petrone, C., Lopez, P., Talamonti, R., & Manfredi, G. (2012). "Shake table tests for seismic

assessment of suspended continuous ceilings." *Bulletin of Earthquake Engineering*, 10(6), 1819-1832.

Matlab and Statistics Toolbox. (2013). Natick, Massachusetts, United States: The MathWorks Inc.

Mohammed, H., Ghobarah, A., & Aziz, T. (2008). "Seismic Response of Secondary Systems Supported by Torsionaly yielding Structures." *Journal of Earthquake Engineering*, pp. 932-952.

Mosqueda, G., Retamales, R., Filiatrault, A., & Reinhorn, A. (2009). "Testing facility for experimental evaluation of non-structural components under full-scale floor motions." *Journal of The Structural Design of Tall and Special Buildings,* 18, pp. 387-404.

Nagarajaiah, S., Reinhorn, A. M., & Constantinou, M. C. (1992). "Experimental study of sliding isolated structures with uplift restraint." *Journal of Structural Engineering*, 118(6), 1666-1682.

Parise, G., Martirano, L., Parise, L., De Angleis, M., Reggio, A., & Weber, J. (2013). "Seismic Qualification of Electrical Equipment in Critical Facilities." Industrial and Commercial Power Systems Technical Conference. IEEE.

Park, Y., & Ang, A. (1985). "Mechanistic seismic damage model for reinforced concrete." *Journal of Structural Engineering*, ASCE, pp. 722-739.

Porter, K. (2009). "Fragility of Battery Racks." *Federal Emergency Management Agency FEMA*.

Porter, K., Krishnan, S., & Xu, X. (2006). "Analysis of simultaneous operational failure of critical facilities due to earthquake, for a California utility." *Earthquake Engineering Research Laboratory EERL 2006-01*, Pasadena, California.

Priestley, N., Calvi, G., & Kowalsky, M. (2007). "Displacement-based seismic design of structures." *IUSS*. Pavia, Italy.

Rahmanishamsi, E., Soroushian, S., & Maragakis, E. M. (2014). "Seismic response of ceiling/piping/partition systems in NEESR-GC system-level experiments." *In Structures Congress* 2014 (pp. 1824-1835).

Retamales, R., Mosqueda, G., Filliatrault, A., & Reinhorn, A. (2011). "Testing Protocol for Experimental Seismic Qualification of Distributed Nonstructural Systems." *journal of Earthquake Spectra*, 27(3), pp. 835-856.

Roussis, P. C., & Constantinou, M. C. (2005). Experimental and analytical studies of structures seismically isolated with an uplift-restraint isolation system (No. 1). *Multidisciplinary Center for Earthquake Engineering Research*.

Di Sarno, L., & Manfredi, G. (2012). "Experimental tests on full-scale RC un-retrofitted frame and retrofitted with buckling-restrained braces." *Earthquake Engineering & Structural Dynamics*, 41(2), 315-333.

Salawu O.S. (1997), "Detection of structural damage through changes in frequency: a review", *Engineering Structures*, vol. 19(9), pp. 718-723.

SQUG. (1999). "Electronic Earthquake Experience Database User's Guide: SQUG EPRIWEB Site." *CA: EPRI, TR-113705*, Palo Alto.

SQUG. (2017). Retrieved from http://www.squg.mpr.com

Telcordia Technologies. (2002). "Network Equipment-Building System (NEBS) Requirements: Physical Protection." *Specification GR-63-CORE*, Issue 2.

Vamvatsikos, D., & Cornell, C. A. (2002). "Incremental dynamic analysis." *Earthquake Engineering & Structural Dynamics*, 31(3), 491-514.

Wang, Z.Z., Jiang, Y.-J., Zhu, C.A., & Sun, T.C. (2015). "Shaking table tests of tunnel linings in progressive states of damage." *Journal of Tunneling and Underground Space Technology,* 50, pp. 109-117.

Whittaker, A., & Soong, T. (2003). "An overview of nonstructural components research at three U.S. earthquake engineering research centers". *Seminar on Seismic Design, Performance, and Retrofit of Nonstructural Components in Critical Facilities ATC-29-2*.

Wilcoski, J., Gambill, J., & Smith, S. (1997). "CERL equipment fragility and protection procedure (CEFAPP)". *U.S Army Construction Engineering Research Laboratory, USACERL Technical Report 97/58*, Champaign, Illinois.

Wittich, C., & Hutchinson, T. (2015). "Shake table tests of stiff, unattached, asymmetric structures." *Journal of Earthquake engineering and structural dynamics*, vol. 44, pp. 2425-2443.

Yan, L., Chouw, N., & Jayaraman, K. (2014). "On energy absorption capacity, flexural and dynamic properties of flax/epoxy composite tubes." *Fibers and Polymers*, 15(6), 1270-1277.

Zentner, I., Gündel, M., and Bonfils, N. (2017). "Fragility analysis methods: Review of existing approaches and application." *Nuclear Engineering and Design*, 323, 245-258.

Table 3.1. Demand and capacity of the HAD anchor

Failure mode	Demand (kN)	Capacity (kN)
Tension	19	45
Shear	9	20

Table 3.2. FEMA 461 recommended MATLAB parameters

Parameter	Value
Sample Rate (Hz)	100
Beginning Sweep Rate (octaves/min)	6
Ending Sweep Rate (octaves/min)	6
Beginning Center Frequency (Hz)	0.5
Ending Center Frequency	32
Filter Bandwidth (octaves)	1/3
Filter Error (octaves)	0.2

Table 3.3. Peak ground accelerations and their corresponding scale factors

and observed damages

Scale factor	PGA (g)	Observed damage	Elastic spectral acceleration (g)
0.50	0.18		0.41
0.63	0.22		0.59
0.78	0.28		0.82
0.98	0.35	- buckling of the lower back brace	1.13
1.22	0.43	- buckling of both lower braces	1.47
1.53	0.54	- nut slip between column and rail - yielding of the braces	1.90
1.91	0.67	- nut slip between end rail and supporting rail - buckling of the upper braces	2.41
2.38	0.84		3.08
2.98	1.05		3.88
3.73	1.32		4.94
4.66	1.64	- excessive rack deformations	5.85
5.82	2.06		7.64

Table 3.4. Different parameters used to develop fragility curves

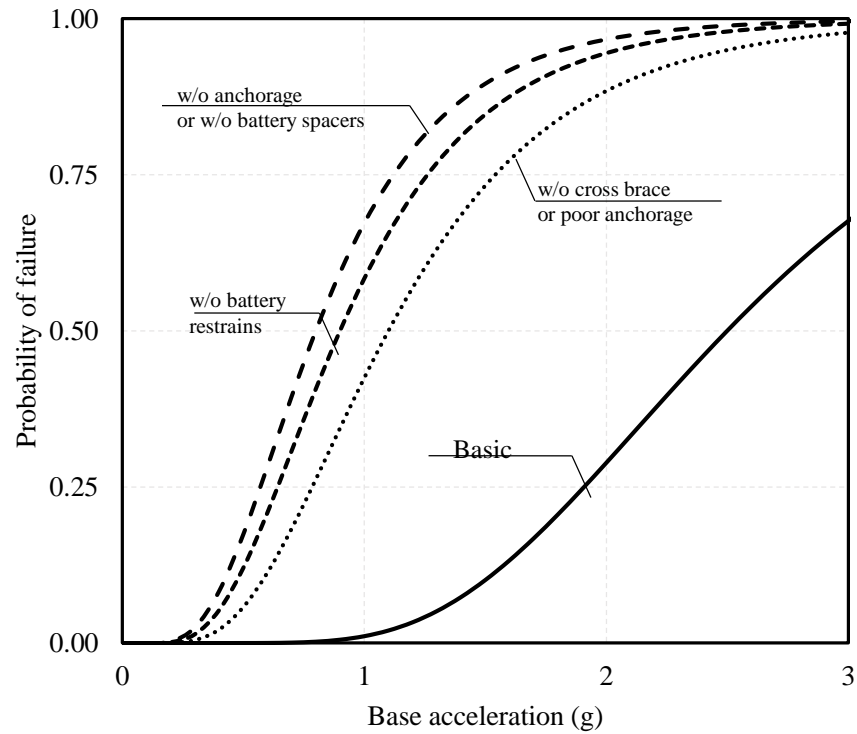| Parameter	DS1	DS2	DS3	DS4	FEMA P-58 well installed	FEMA P-58 deficient installed
Damage description	Nut slip	Brace yielding	Conductor breakage and malfunction	Excessive rack deformations	N.A.	N.A.
SF	1.53	1.53	1.91	4.66		
FRS	1.10	1.10	1.10	1.10		
FD	1.90	1.90	1.90	1.90		
βU	0.28	0.28	0.28	0.28		
βR	0.09	0.09	0.09	0.09		
PFA	0.56	0.56	0.70	2.27		
βc	0.29	0.29	0.29	0.29	0.20	0.60
Am	1.17	1.17	1.46	4.74	2.32	1.11

Figure 3.1: Fragility curves of battery rack systems, data from Johnson *et al* (1999).
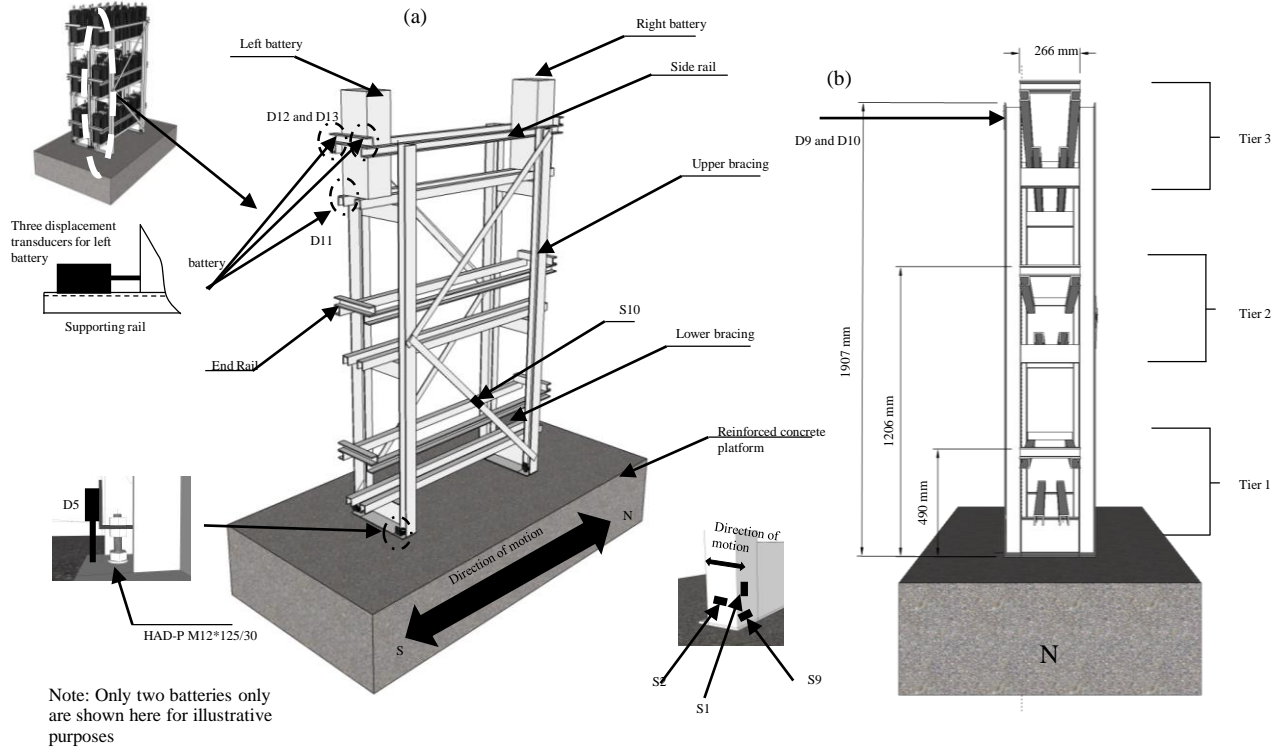
Figure 3.2: Rack EP1 configuration; (a) Three dimensional (3D) view from the South direction; (b) 3D view from the North direction.
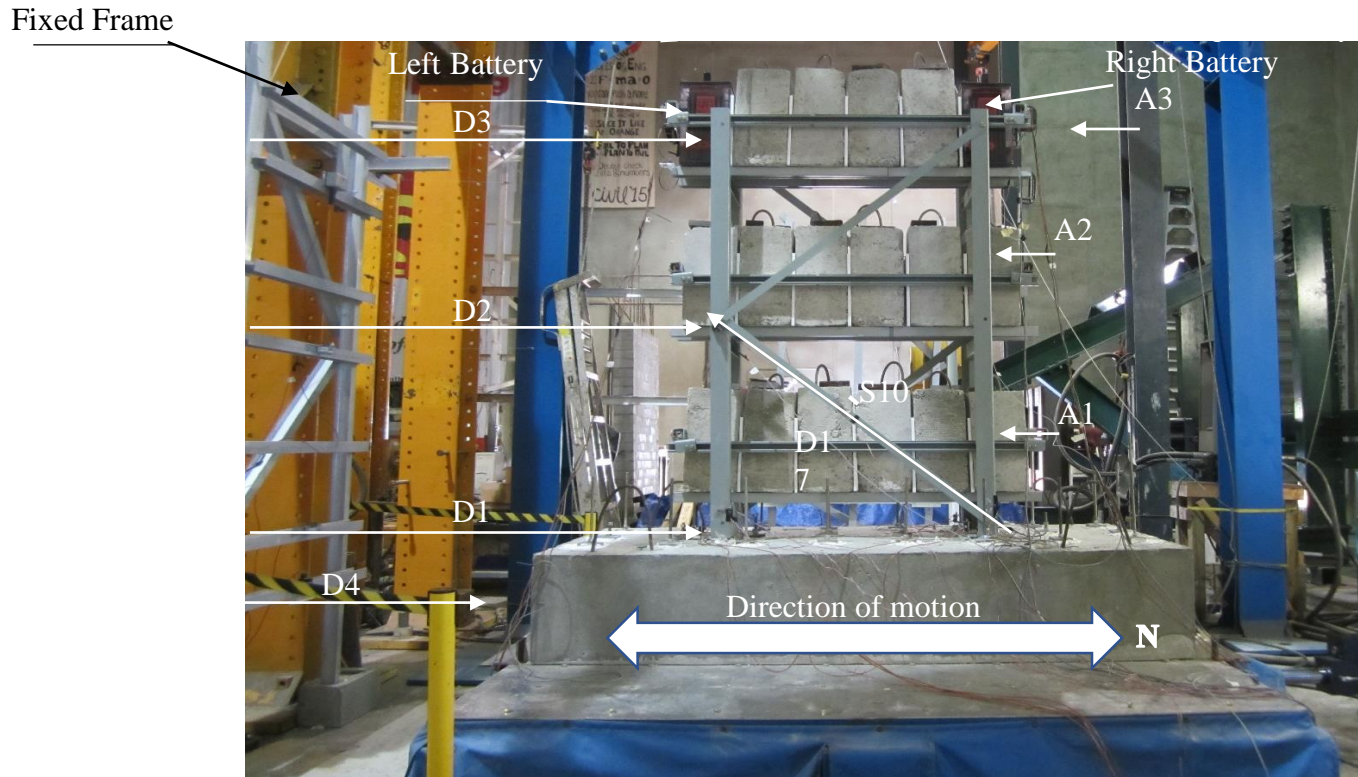
Figure 3.3: Test setup and fixation of the battery rack system to the shake table, image by Ahmed Ghith.

	Unfiltered	Filtered
PGA	0.35g	0.36g
ξ	5%	5%
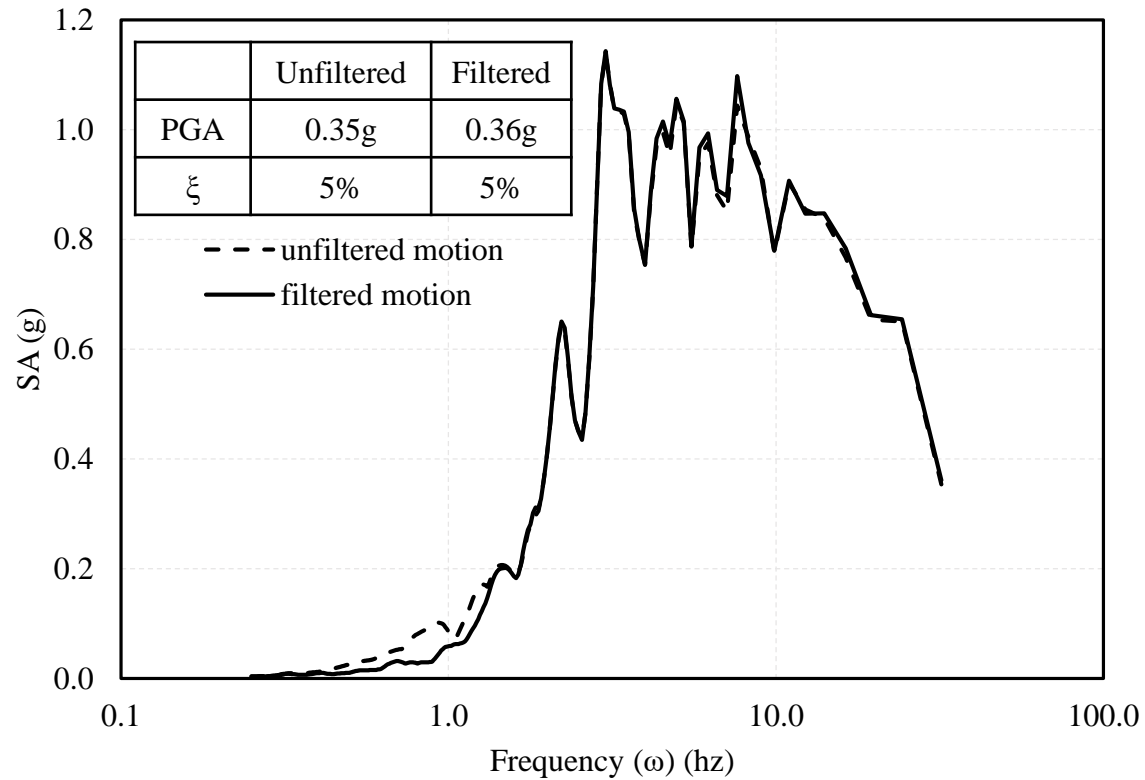
Figure 3.4: Response spectra of filtered and unfiltered FEMA 461 generated ground motion record.
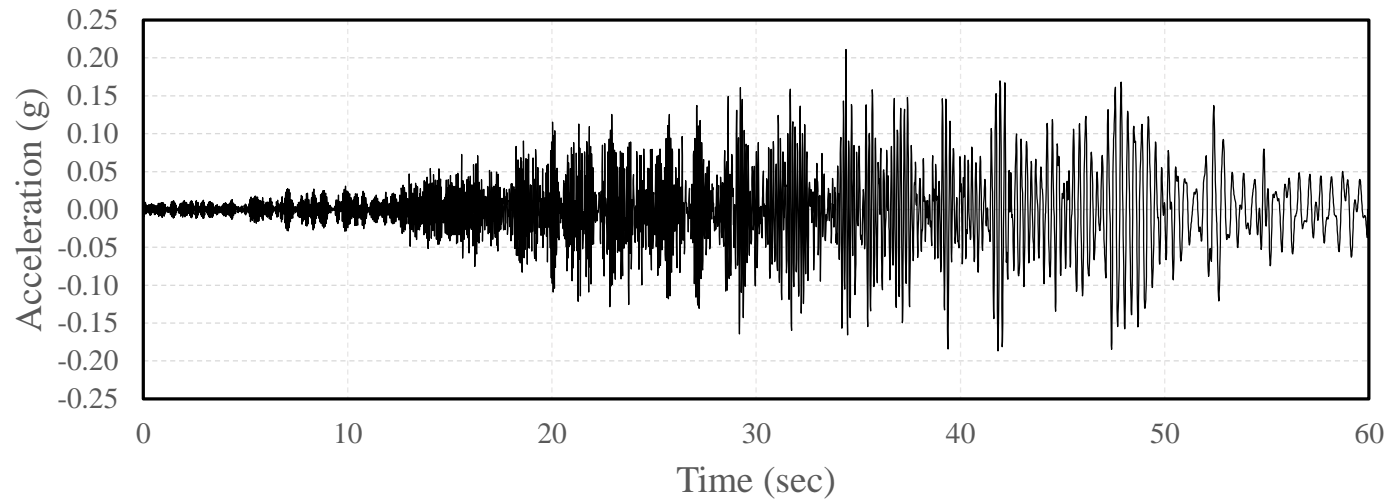
Figure 3.5: Acceleration time history of unscaled FEMA 461 ground motion.

a) SF = 1.53

a) SF = 3.72

a) SF = 4.66
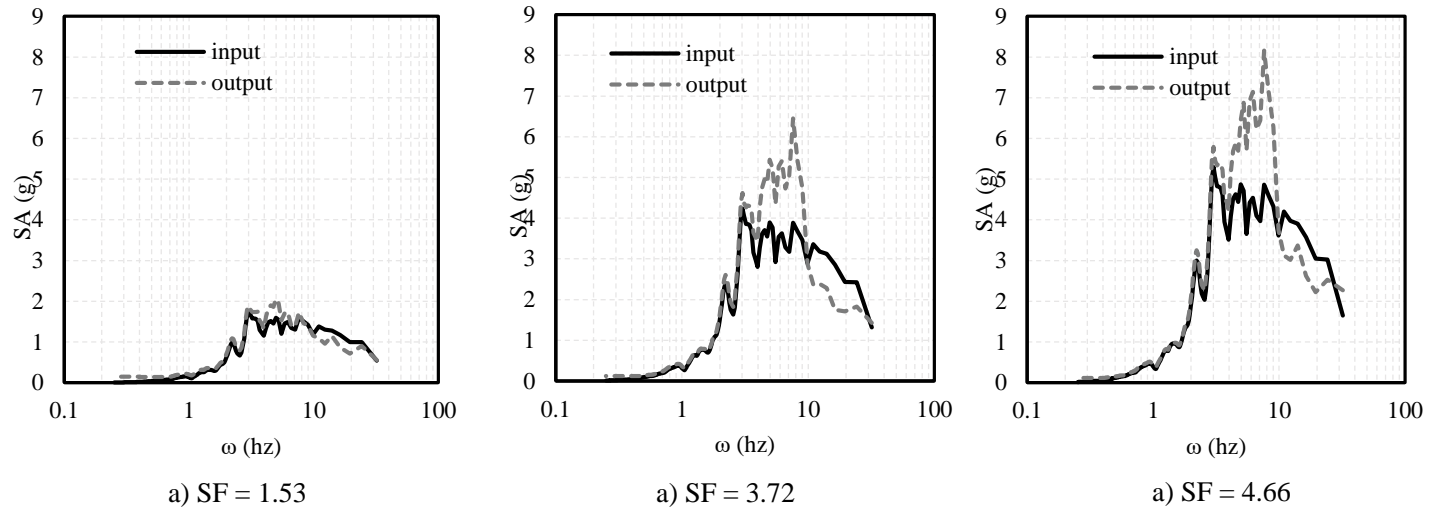
Figure 3.6: Response spectra of the different ground motion levels used through out the test.
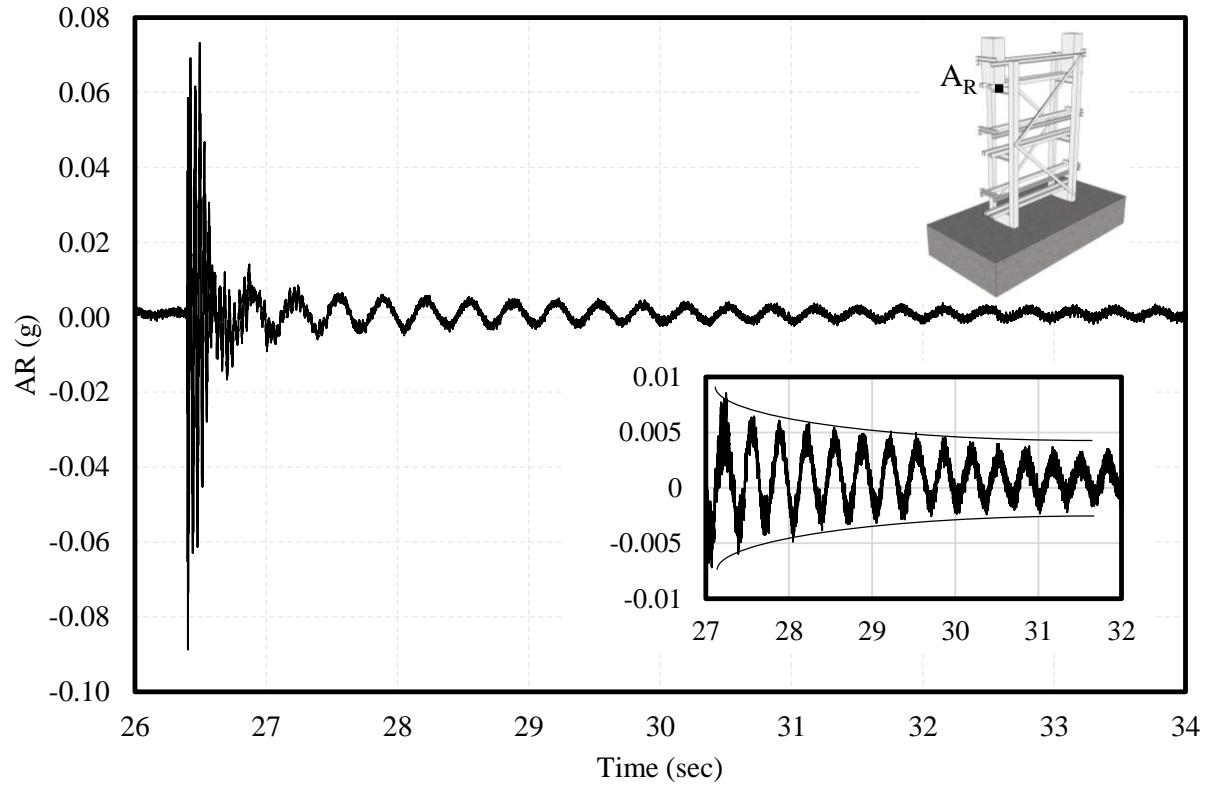
Figure 3.7: Response of the top of the rack to the tap test.
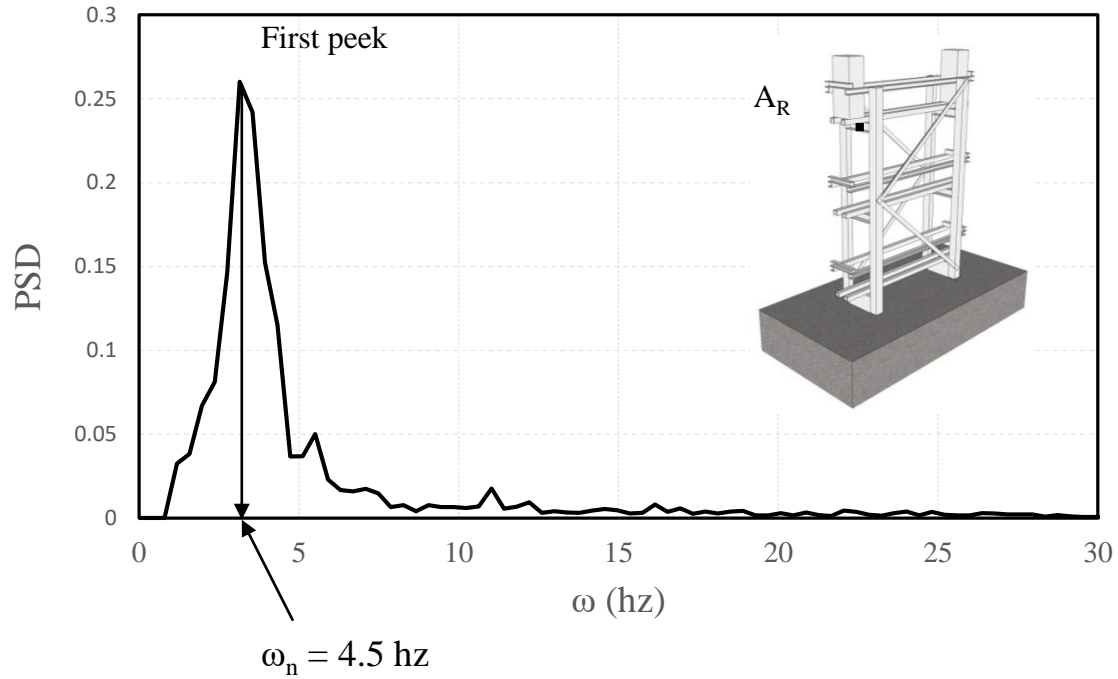
Figure 3.8: PSD of the top of the rack.
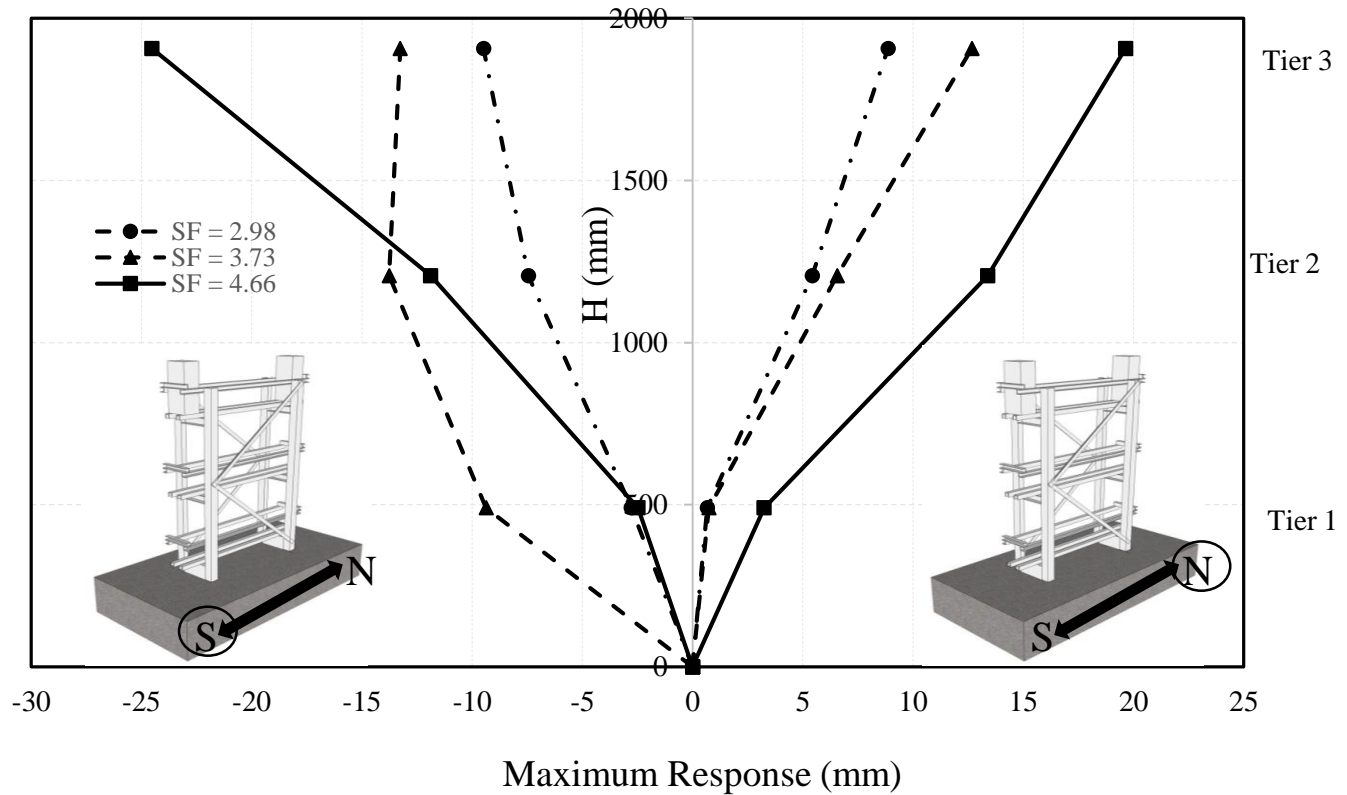
Figure 3.9: Maximum displacement response of the rack at different ground motion levels.

(a)

Permanent brace
deformation

(b)

Permanent brace
deformation
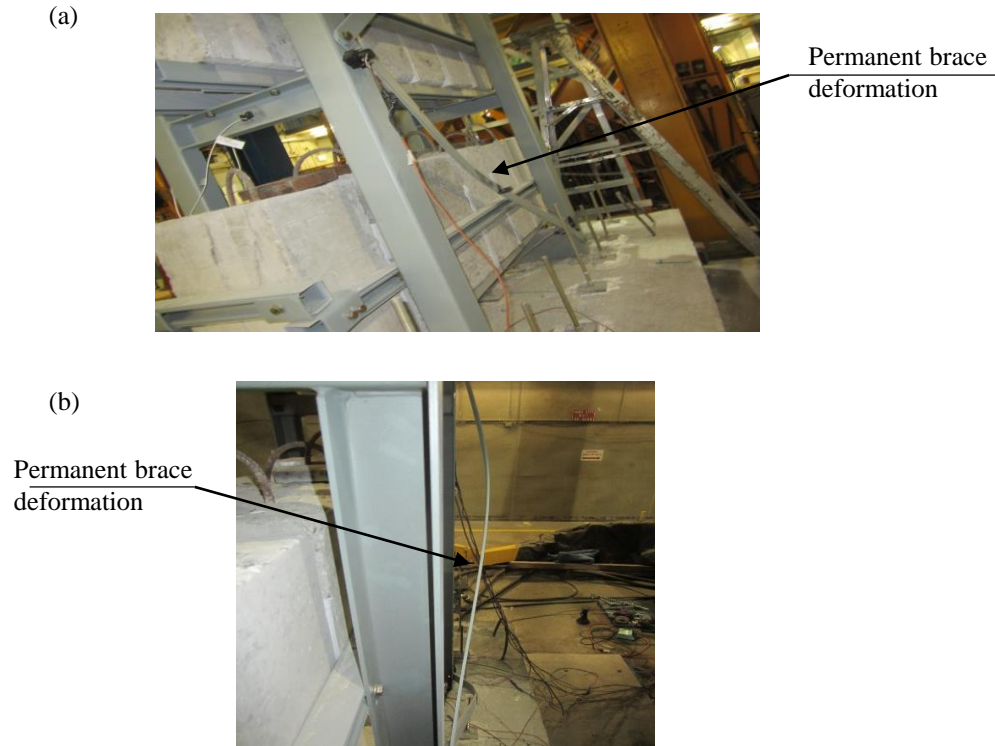
Figure 3.10: Brace buckling after testing due to sliding of nuts connecting columns to side rails, images by Ahmed Ghith.
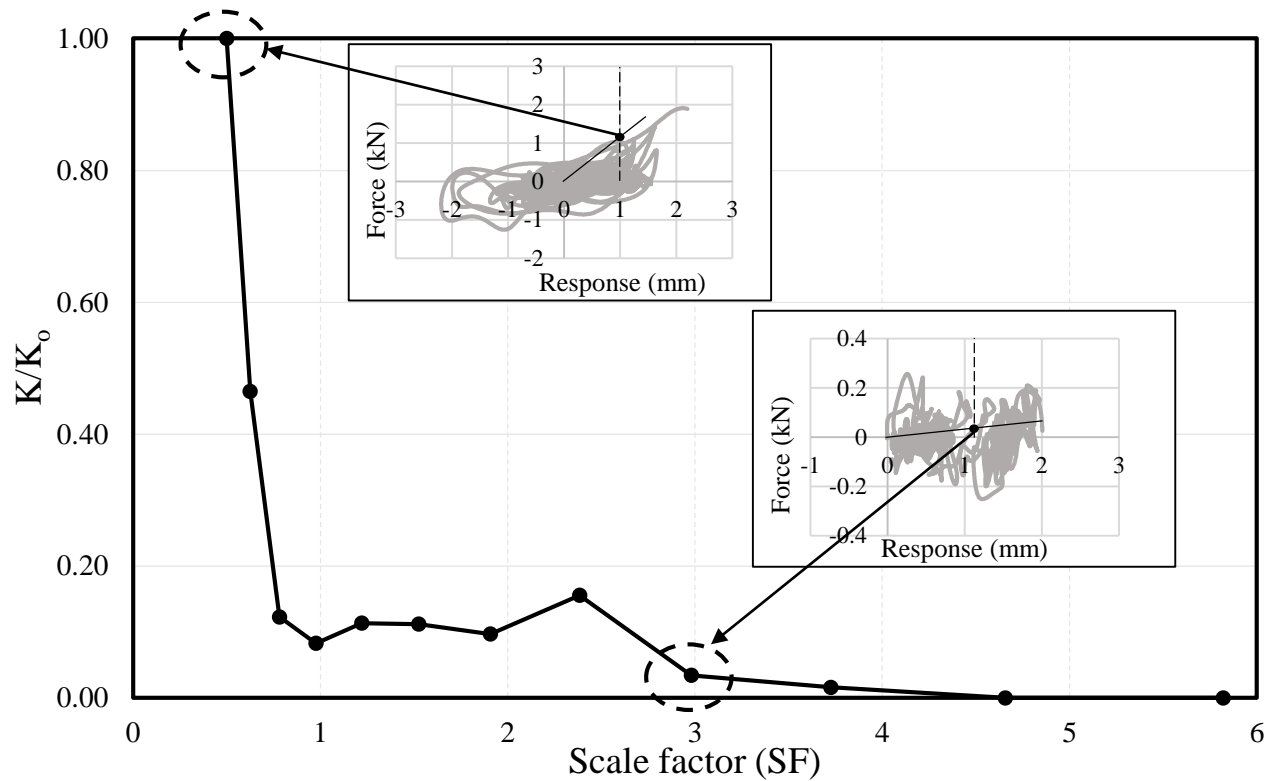
Figure 3.11: Effective secant stiffness of the rack system at different ground motion levels normalized to the initial secant stiffness at SF=0.5.
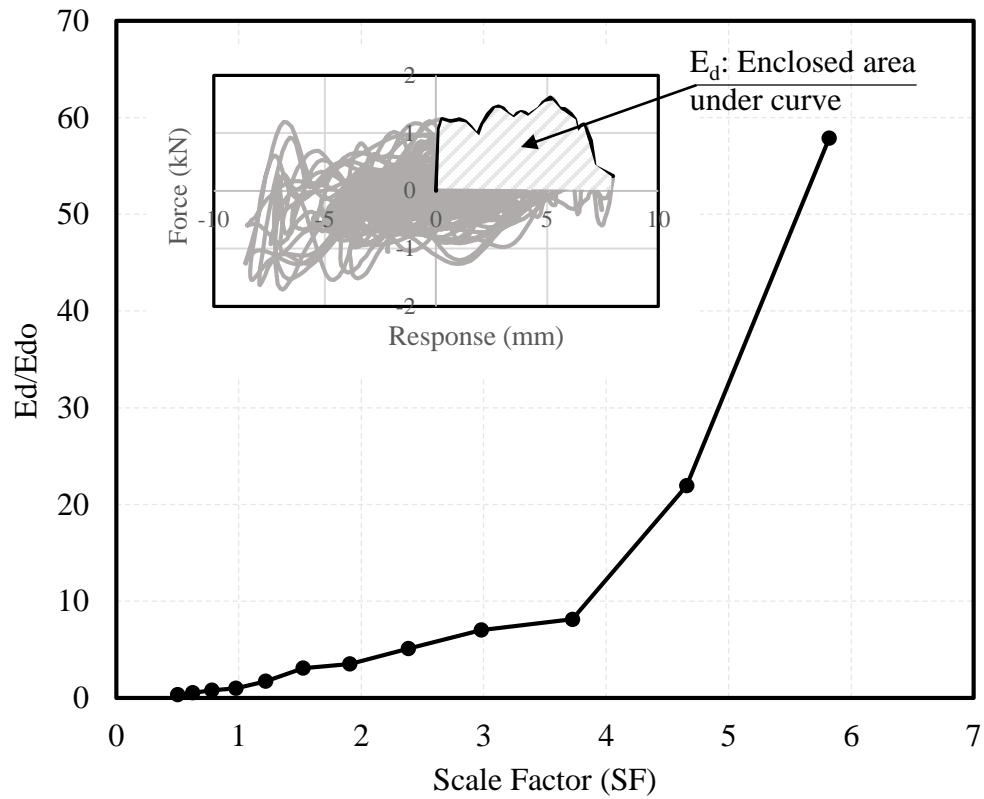
Figure 3.12: Energy dissipation of the battery rack system versus different levels of ground motions.
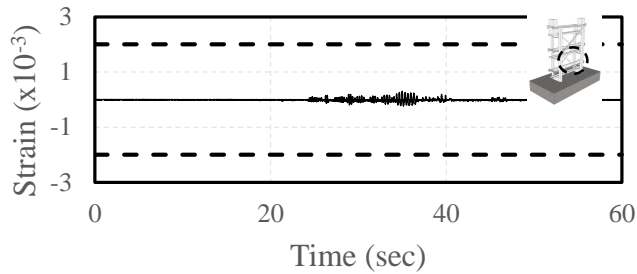
(a)
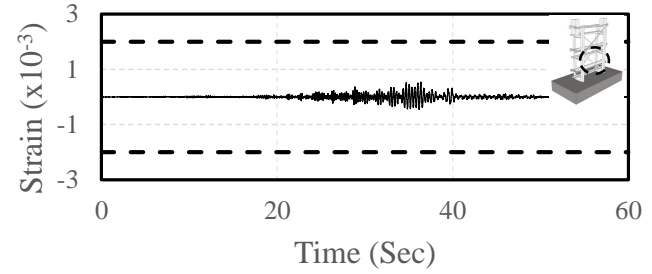
(b)
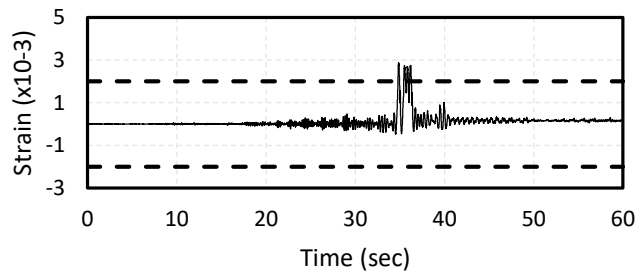
(c)
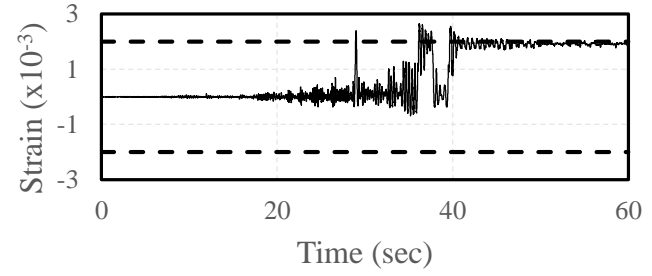
(d)

Figure 3.13: Strain variations in the lower brace at different levels of ground motions; (a) SF=0.5; (b) SF=0.98; (c) SF=1.53; (d) SF=1.91.
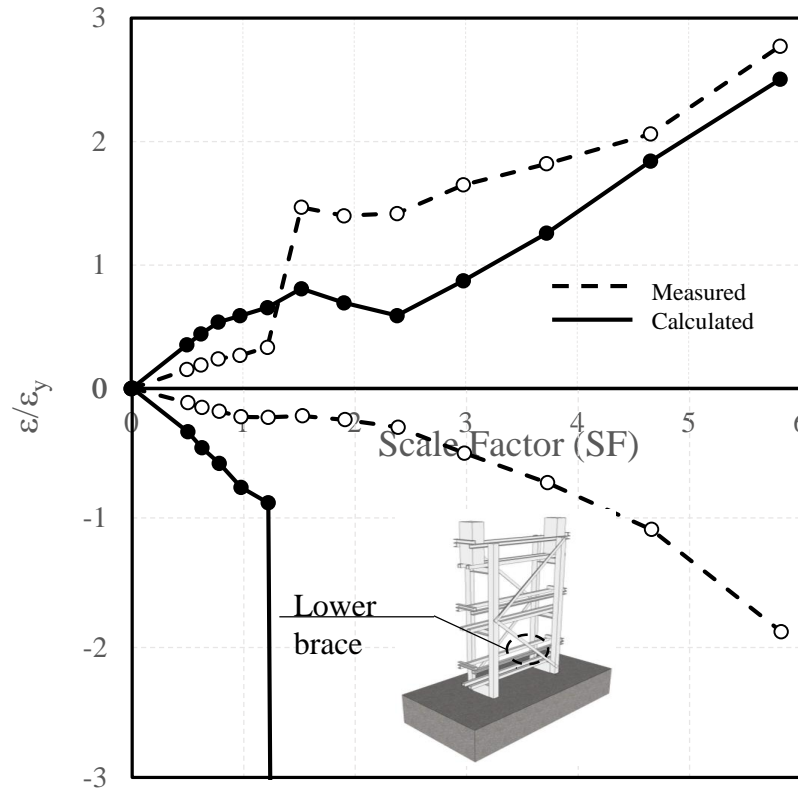
Figure 3.14: Maximum strains in the lower brace at different ground motion levels.
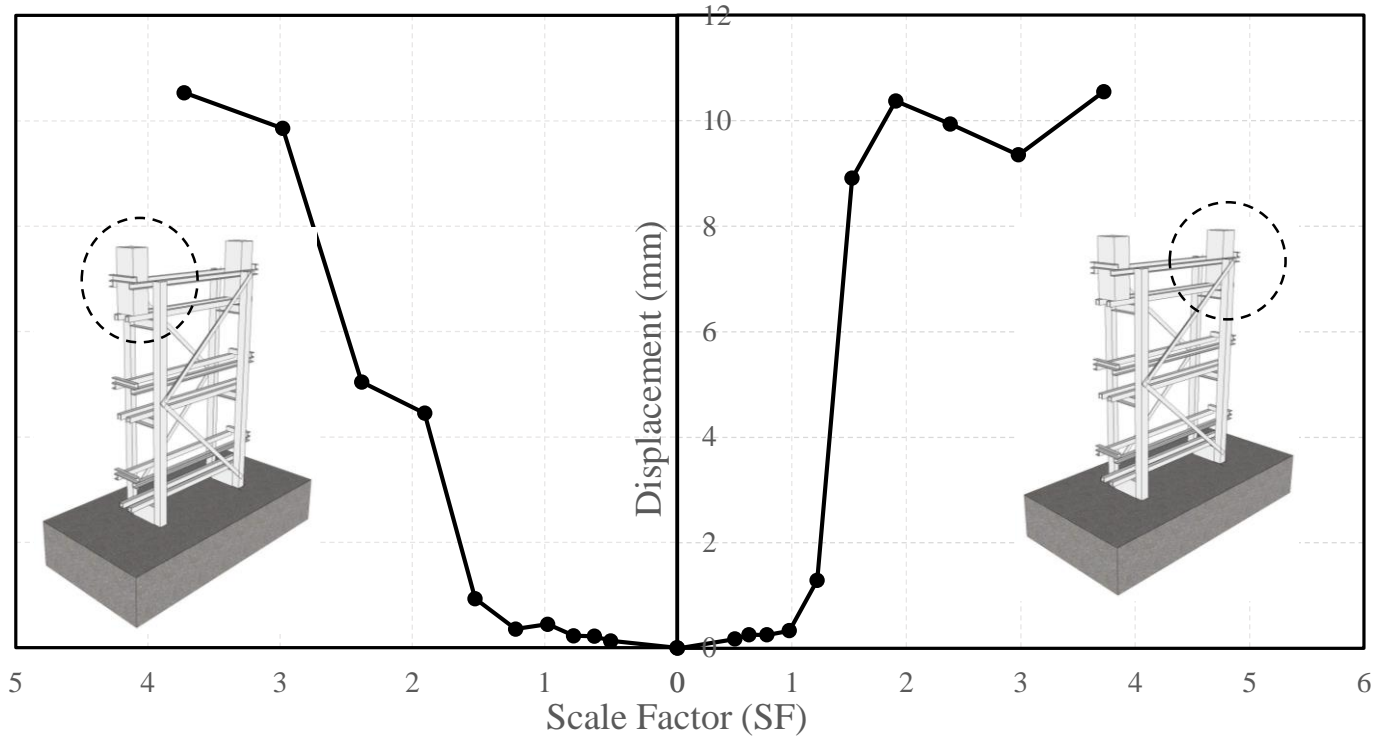
Figure 3.15: Maximum displacement of left and right batteries at different ground motion levels.

(a)

(b)

Gap between batteries
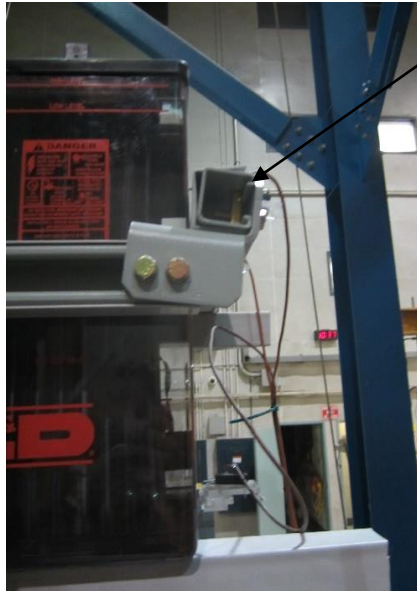
Rotation of end rail with no allowance to slide

Fig. 16: Permanent deformations at SF = 4.66; (a) Rotation of end rails; (b) Increase in gap between batteries, images by Ahmed Ghith.
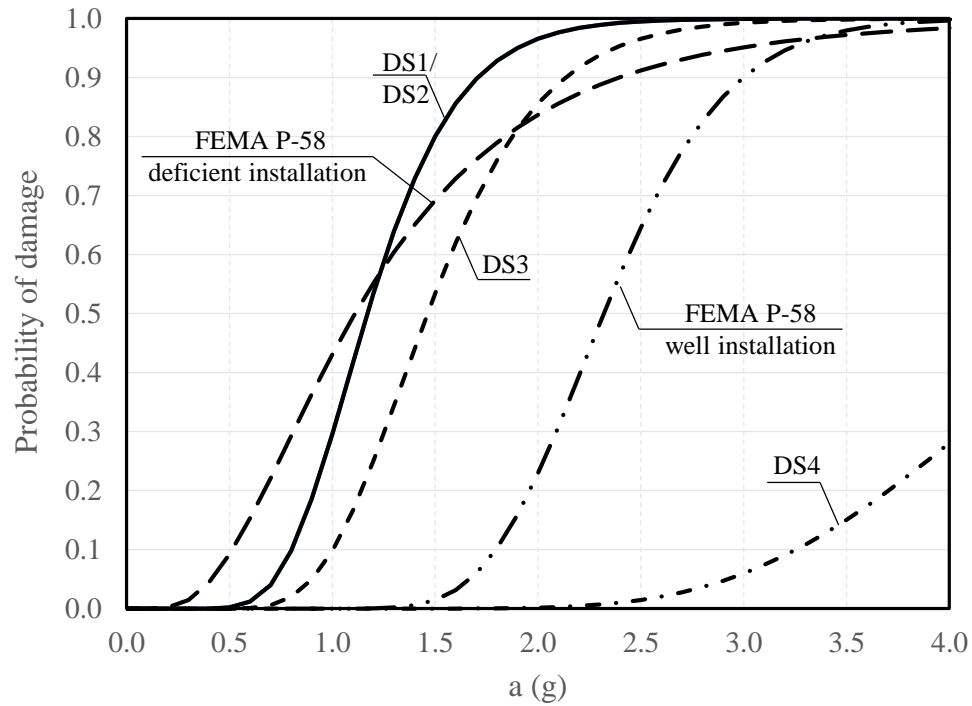
Figure 3.17: Fragility curves for the battery rack system at different damage states (the FEMA P-58 curves are based on data from Porter 2009).

CHAPTER 4

4. OPENSEES MODELING OF ABPS

4.1. ABSTRACT

Auxiliary Battery Power Systems (ABPSs) are currently used as a reliable mitigation strategy in Nuclear Power Plants (NPP) posterior to the failure of offsite power supply. The importance of these systems is manifested by their direct contribution to the core damage frequency. As such, this chapter presents a numerical model of a commercially available ABPS currently operating/existing in NPP. The 3D model is developed using OpenSees software. The model is then validated using quasi-static test results from previous studies. The model is found to be in good agreement with the experimental results in terms of the initial stiffness and the ultimate capacity. The lateral performance of the ABPS is found to be governed by the capacity of the L-shaped connection between the side rails and the end rail. As such, the lateral capacities of several additional racks were evaluated to investigate the capability to seismically upgrade the ABPS by adding extra braces, as recommended by the manufacturer. Addition of extra braces should help increase the lateral stiffness and capacity, however, the capacities of eight different configurations of ABPS, having different lengths, tiers, and seismic categories, were found to be limited by the weakest link the L-shaped connection, and the addition of extra braces did not benefit the lateral capacity of ABPS. Furthermore, the model is also compared to results from dynamic shake table tests. The model

was updated to account for the dynamic rigid body response of the batteries, in terms of sliding and impact. However, the model was not able to predict all damage states observed from experimental tests, since the modeling of the rocking/sliding/impact behavior of the batteries simultaneously is a highly complex nonlinear problem by nature and beyond the scope of this study. The model presented is limited to the static assessment of the lateral performance of different ABPS.

4.2. INTRODUCTION

An Auxiliary Battery Power System (ABPS) is a widely used backup power system in Nuclear Power Plants (NPPs). It is used as a mitigation technique after the loss of offsite power. As such, it is critically important that these systems remain functional during and after seismic events. Moreover, the importance of ABPS was obvious during the Fukushima Daiichi Nuclear accident, after the loss of offsite power, and the flooding of emergency diesel generators. The ABPS of unit 3 was used to supply power to the rest of the station for 8 hours until the ABPS eventually ran out and the meltdown of the NPP started (NAIIC, 2011). As such, it is expected that ABPS has a major contribution to the failure probability of the NPP, for example, Choun, et al. (2008) have shown that the failure of the ABPS has a direct contribution to the Core Damage Frequency (CDF) of the NPP.

After the Fukushima accident, regulatory bodies in Canada updated the design requirements of NPPs to include Beyond Design Basis Events (BDBE).

BDBE is a new concept in design to ensure the existence of a safety margin between the failure of safety-related components and the design requirements. As such careful characterization of the failure of ABPS is required.

Failure of ABPS was initially investigated by Johnson, et al. (1999) using fragility curves to show the failure of the ABPS based on different in-situ conditions. The data used were based on historical observations from the Seismic Qualification Utility Group (SQUG) database (2017). Later on, Porter (2009) updated these curves by adding additional data from EPRI (1991), which are based on experience and testing. However, both research studies did not describe the different failure modes experienced by each ABPS and the corresponding demands. As such, there is a need to carefully investigate possible damage states of ABPS and present the corresponding demands.

Analytical models are typically a credible method to assess the performance of structural and nonstructural components under different loading scenarios. Analytical models can be a relatively inexpensive alternative to experimental testing. However, these models need to be validated/calibrated to ensure the accuracy of the simulation. To the best of the authors' knowledge, Berak and Mrconi Communications (2005) is the only publicly available research study that describes the development of a numerical model for ABPS, which presented a finite element model of ABPS for telecommunication applications. The authors validated the model against pull tests and shake table test results. However, due to the presence of a wide range of ABPS configurations and types for different

applications, there is a real need for further investigation and analytical modeling of ABPS.

This study presents a 3D model of a commercially available ABPS system operating/exiting in several NPPs. This study first presents the formulation of an OpenSees model of the ABPS and the simulation of different connection properties. Secondly, the model is validated against static experimental test results (Ghith, et al., 2019). The model is then used to predict the capacity of other ABPS configurations presented by the same manufacturer. Furthermore, the model is compared to dynamic test results (Ghith et al. 2019) and an updated model is presented to account for the dynamic response of the batteries. Finally, the limitations of the model are presented and the complex problem of accurately modeling the response of individual batteries is discussed.

4.3. EXPERIMENTAL PROGRAM AND TEST RESULTS

Ghith et al. (2019) tested a commercially available ABPS under a quasi-static fully reversed cyclic loading protocol adopted from FEMA 461 guidelines (2007). The ABPS had a 2-tier-1-step system configuration, as shown in Fig. 4.1. The displacement control cyclic loading was applied at the batteries of the top tier with two cycles at each amplitude, with a total of 65 cycles performed reaching a maximum amplitude of 99 mm. The testing was terminated due to the local failure of an L-shaped connection between the side rail and the end rail. Moreover, the presence of the sliding nuts between the columns and the side rails allowed the

formation of rotational hinges that prevented the utilization of full framing action between the vertical columns and the horizontal beams (i.e. side rails).

4.4. MODEL DESCRIPTION

A comprehensive 3D model was developed using OpenSees (McKenna, 2016) to replicate the performance of ABPS under cyclic loading. An extensive investigation was performed in an effort to capture all details of the ABPS, such as rack connections, battery behavior, and brace performance.

4.4.1. Rack Simulation

All rack elements were modeled using Force-Beam-Column elements with fiber sections. The formulation of these Force-Beam-Column elements assumes a uniform axial force and a linear distribution of the bending moment along the elements. Five and three Gauss-Lobatto integration points were chosen for the columns and the rails, respectively. All rack elements were modeled using fiber sections to define regions of maximum stress. All element cross-sectional dimensions were adopted from Ghith et al. (2019). The Steel02 uniaxial material command, implemented in OpenSees, was used to model the material behavior with Young's modulus and yield strength of 216 GPa and 316 MPa, respectively.

4.4.2. Connection Simulation

The connection between the column-girder panel, and the side rails or the supporting rails use serrated strut (i.e. T-sliding) nuts. The friction force between the column and the side rail depends on the clamping force, the friction coefficient

between column and side rail (epoxy coated), and the friction coefficient between the nut (with teeth) and the side rail. While the clamping force of the bolt depends on the amount of applied torque, the bolt diameter, and the friction coefficient between the bolt head and the member material. The friction force between the epoxy-coated steel has been studied in the literature (Sabino-Netto et al., 2008; Mihu et al., 2017; Kumar et al., 2014), the friction coefficient is found ranging from 0.15 to 1, moreover, the friction coefficient of dry steel on dry steel also ranges from 0.2 to 0.78 (Avallone, 2017). Thus, as a result of the large variation in the friction coefficient values presented in the literature, the lower and upper bounds of the friction force were calculated to be 4 and 22 kN, respectively. Consequently, the response of the sliding nuts was further investigated experimentally. Test results are shown in Fig. 4.2 along with the average friction force from the tests. The average friction force was determined to be 14 kN, as shown in Fig. 4.2. An idealized elastic-perfectly plastic material model was developed to be used as input for the OpenSees simulation of these connections.

As shown in Fig. 4.3, the connection between the side rail and the L-shaped connection has 2 sliding-type nuts. As such, the clamping force was assumed to be doubled, and following the slip critical connection design presented in CSA S16-14 (2014), the required friction force to cause a slip of the connection would be doubled as shown in Fig. 4.3.

In addition, according to Shi and Fan (2018), the use of an eccentric beam-column joint of rectangular tubed cross-sections will result in additional torsional

deformations, which will cause a decrease in the rotational elastic stiffness up to 30% compared to concentric cross-sections. Accordingly, the use of a C-channel cross-section (i.e. cross-section of columns and rails of the tested ABPS) will result in even lower elastic stiffness compared to a concentric joint. Moreover, joints are considered to be partially fixed if the elastic stiffness is ranging from 20% to 90% of a fixed connection (Salmon et al., 2008). As such, the connection between the columns and joints was assumed to have zero rotational elastic stiffness (i.e. relative rotational deformation between the columns and the joints was allowed).

Finally, as discussed by Ghith et al. (2019), the column base could rotate in one direction and was prevented from rotation in the other direction due to bearing against the reinforced concrete platform. As such, the model of the support at the bottom of the columns was developed to simulate experimental findings. The column rotational supports were modeled as linear rotational springs with different positive and negative stiffness values. The stiffness in one direction was determined from the rotational stiffness of a cantilever steel beam, as shown in Fig. 4.4, while the rotational stiffness in the other direction was determined from the rotational stiffness of a fixed-hinged beam.

4.4.3. Battery Simulation

Each battery was modeled as a combination of rigid elastic elements connected together, as shown in Fig. 4.5. The results of Ghith et al. (2019) have shown that the presence of the batteries along each tier acted as a diaphragm that prevented the inward deformation of the rack elements, as shown in Fig. 4.5a. As

such, each battery was connected to the adjacent side rails using two zero-length elements (i.e. a total of four zero-length elements) with a predefined rigid compression-only material, as shown in Fig. 4.5b.

In order to model the friction between the batteries and the rack, the friction coefficient had to be determined. Ellobody and Young (2006) found the friction coefficient between concrete and steel to be 0.25. Using the mass of each battery, the frictional force required to move the battery relative to the supporting rails was determined to be 0.16 kN. Six zero-length elements were used to model the friction between each interior battery and the supporting rails, as shown in Fig. 4.6. However, only four zero-length elements were used to model the friction for the first and last batteries to facilitate the connection of the end batteries to the adjacent moving end rails. Figure 4.6 shows the behavior of the friction model used to model the friction of a single battery in OpenSees.

To simulate the lateral behavior of the tested rack, detailed consideration was given to the loading mechanism. As previously described by Ghith et al. (2019), during the experimental tests, the displacement-controlled load was applied via an actuator connected to a rigid steel beam, the steel beam was welded to the first and last steel batteries, respectively, which bounded the row of batteries to move together. As such, during the simulation, the batteries were connected using rigid zero-Length elements. In order to transfer the load from the end batteries to the end rails, the end batteries were connected to the end rails at the midpoint and the endpoints instead of the midpoint only to avoid premature failure of the end rail.

Moreover, to allow the end batteries to move away from the end rail freely, rigid elastic elements with compression-only zero-Length elements in the longitudinal direction were used.

4.4.4. Brace Simulation

As described by Ghith et al. (2019), the braces had a low buckling capacity due to the cross-sectional area of the braces and the end boundary conditions, which were assumed to be hinged-hinged. A number of researchers have modeled the buckling behavior of braces. Batterman and Bruce (1967) proposed the idea of introducing initial imperfection (i.e. camber) during the simulation of braces to enforce second-order bending moments and thus introduce buckling, otherwise, the brace will deform in compression only. Later, Gunnarsson (2004) studied the use of an initial imperfection while also dividing the brace into several smaller Force-Beam-Column elements. Several studies have been performed in order to optimize the number of these elements (Gunnarsson, 2004; Terzic, 2013). These studies confirmed that the use of more than 10 elements is typically sufficient to capture the buckling behavior. As such, the brace was divided into 20 elements in the OpenSees model with a calibrated imperfection of L/100.

4.5. VALIDATION OF MODEL VS QUASI-STATIC TESTING

The cyclic loading protocol adopted in the experimental tests was followed (Ghith et al., 2019). The loading protocol adopted in the experimental test followed the FEMA 461 guidelines with a total of 65 fully reversed displacement-controlled

cycles with increasing amplitude, further information regarding loading protocol can be found in (Ghith et al., 2019). Figure 4.7 shows the model cyclic behavior against the experimental hysteretic response. The figure shows good agreement between the model and the experimental cyclic behavior. According to Ghith et al. (2019), the testing was stopped upon failure of the L-shaped connection, the sliding nut connecting the L-shaped connection to the end rail caused the internal lip of the end rail to fail resulting in connection failure. On the other hand, this model focuses on the global behavior of the ABPS system (i.e. macro model). As such this model is unable to simulate the failure of the lip of the end rail, thus the failure of the L-shaped connection was limited to the maximum deformation of the connection in the experimental results.

The figure in the top left corner of Fig. 4.7 shows the envelope of the experimental cyclic response and the envelope of the model cyclic response. The figure shows good agreement between the model and the experimental test results in terms of the initial stiffness at the early cycles. The model correctly captures the yielding of braces and the yielding of the L-shaped connection, as such the model accurately predicts the yield load and the corresponding yield deformation. After yielding, the model is able to capture the hysteretic behavior of the system, however, the model is unable to capture the increase in loading immediately prior to failure. The figure in the bottom right corner of Fig. 4.7 shows the cyclic behavior of the simulated rack against the cyclic behavior from the experimental results for cycles 21 and 28 (i.e. displacement levels 44 and 78 mm respectively). This figure

shows good agreement between the model and the experimental results in terms of the maximum lateral load and the energy dissipation after yielding.

4.6. PUSHOVER ANALYSIS OF DIFFERENT TYPES OF ABPS

The manufacturing company (C&D Technologies Inc., 2017) offers several different types of ABPS that are based on the same main frame. Upgradability from one seismic grade to the next is accomplished by the addition of extra bracing, while different ABPS retain the same columns, side rails, girders, supporting rails, end rails, and L-shaped connections. However, the above experimental results and the validated model show that the L-shaped connection is the weakest connection, indicating that the investigated lateral capacity of the ABPS is governed by this connection.

As such, the above-validated model was used to statically investigate the lateral behavior of several different ABPS similar to that provided by the same manufacturing company to assess the use of additional bracing to enhance the lateral performance of ABPS. As shown in Fig. 4.8, eight types of ABPS were simulated having different numbers of tiers, different lengths, and different seismic grades. The results of the model, shown in Fig. 4.8, indicate that the upgradability of the seismic grade by the addition of extra braces led to an increase in the lateral stiffness of the ABPS. The addition of extra braces did not benefit the lateral capacity of the ABPS. Figure 4.8 also shows that the 3 tier ABPS configuration has

lower stiffness than the 2 tier ABPS configuration. Moreover, the lateral stiffness of the ABPS, as expected, increased when the length of ABPS was increased.

Nevertheless, Fig. 4.8 also shows that all ABPS started yielding at almost the same lateral load. All the ABPS were found to fail as a result of excessive deformation of the L-shaped connection. For the 5 ft ABPS, an increase in the yield load of 2 % and 1 % was observed by the addition of extra bracing for the 2 tier and the 3 tier ABPS configurations, respectively. However, for the 12 ft ABPS, an increase of 2 % and 0.05 % in the yield loads were observed for the 2 tier and the 3 tier ABPS configurations, respectively. The addition of extra bracing to increase the seismic grade of the ABPS decreased the yielding deformation, however, it appeared to have little effect on the lateral yield capacity of the system.

4.7. DYNAMIC TEST RESULTS

In an effort to further validate the model dynamically, the results of a shaking table test on similar ABPS were considered (Ghith et al., 2019). The dynamic test was performed to investigate the lateral performance of a three-tier-one-step ABPS configuration as shown in Fig. 4.9. The ABPS was tested using a generated ground motion time history at increasing shaking intensity levels as per FEMA 461 (2007) guidelines and recommendations. In total, the ABPS was tested 12 sequential times on a shake table located in Applied Dynamic Laboratory (ADL), McMaster University, Canada. Different members' deformations and the overall rack response in both in-plane and out of plane directions were monitored

during testing. Consequently, four sequential damage states and their corresponding demands were observed; movement of the sliding nuts, yielding of the braces due to buckling, breakage of the conductor connecting the batteries, and the large response of the ABPS. Further information regarding the test setup and results could be found in (Ghith et al., 2019).

As such, the model was further modified to the dynamically tested ABPS configuration. The dynamically tested ABPS used the same material properties as the statically tested ABPS. The connections between the batteries were modified to rigid zero-Length compression-only elements, in order to capture the opening and closing of the gaps between adjacent batteries. Subsequently, the model was analyzed 12 sequential times at increasing shaking intensity levels following the dynamic test loading protocol. The response of the shake table was measured during testing and the recorded acceleration was used as the input time history at the base level in the model.

Figure 4.10 shows the response of the modeled rack versus the experimental results for Scale Factors (SF) of 0.63 and 1.22. The figure shows that the model overestimated the total response of the system, even at the early stages before the observation of any damage. It should be noted that almost 90% of the mass of the ABPS is concentrated in the dead weight of the batteries. As such careful representation of the movement of the batteries must be further investigated and neglecting the dynamic response properties of the moving batteries could lead to unrealistic results.

The moving battery can slide on the supporting rail touching adjacent batteries and spacers causing impact, this impact will dissipate energy leading to a decrease in the response of the batteries after impact. The impact of adjacent batteries and spacers could be observed during testing. The impact behavior of the adjacent batteries could also be observed in the recorded rack acceleration time histories, as the impact between adjacent batteries caused the release of high-frequency vibrations throughout the system (McFadden & Smith, 1984). As such, Fig. 4.11a and 4.11b show the recorded acceleration time histories during testing at the third and second tiers for SF=1.53, respectively. All the recorded acceleration time histories, shown in Fig. 4.11, show the high-frequency spikes in the recorded acceleration histories as a result of the impact behavior.

The end batteries were also able to slide on the supporting rails and touch the end rails causing impact. As such, the relative movement of the end batteries was recorded during testing. Three displacement transducers were used on each side to measure the relative displacement of the end batteries on the top tier relative to the rack. On each side, one displacement transducer was mounted on the supporting rail on the top tier to measure the relative displacement to the bottom of the end battery, while the other two were mounted on the end rail on the top tier to measure the relative displacement to the top of the end battery. Figure 4.12 shows the response of the end battery on the south side relative to the rack for SF = 0.79, 0.97, 1.22, and 1.53, respectively. While Fig. 4.13 shows the response of the end battery on the north side relative to the rack for the same SFs. Figures 4.12 and 4.13

show the recorded spikes as a result of the high-frequency vibrations released during the impact of the end batteries to the adjacent end rails while testing.

The model also neglected the free body rigid rocking motion of the batteries. This rocking motion of the batteries will affect the total response of the system, as the rocking motion of the batteries will cause a vertical impact to the supporting rails creating high-frequency vibrations as mentioned before. The uplift behavior of the rocking motion of the batteries could be observed during testing at higher ground motion intensities. As Fig. 4.14 shows the response of a middle battery in the top tier for SF=4.66, where the full rocking cycle (i.e. uplift right side-full contact-uplift left side) could be observed.

However, the rocking motion of the end batteries could be observed at lower earthquake intensity levels in the recorded relative displacements. Figure 4.15 shows the recorded relative displacement at SF=1.53 of the north and south sides end batteries, respectively. As shown in Fig. 4.15, there is a difference in the response of the end batteries between the top and bottom levels. This is attributed to the different horizontal displacement of the end batteries while rotating, which was caused by the rocking motion during testing.

Shenton and Jones (1991) have studied the two-dimensional mathematical simulation of a rigid body subjected to sliding and rocking motions. The authors investigated the initiation of the sliding or rocking motions from rest separately and consecutively. As such, they have shown that a rocking motion of a rigid

rectangular block could be triggered from rest (i.e. no sliding) if the following condition occurs

$$|\ddot{x}_g| > g\frac{B}{H}$$ (1)

where, $\ddot{x}_g$ is the horizontal acceleration at the bottom of the rigid body at any point in time, g is the gravitational acceleration, B is half the width of the rigid body in the 2D rocking motion direction, and H is half the height of the rigid body. This above condition was expected to happen at SF=0.98. However, Shenton and Jones (1991) also described that the mathematical representation of the initiation of the rocking motion of a rigid body can become complicated as soon as other modes, for example sliding, occur.

4.8. UPDATED MODEL FOR DYNAMIC BEHAVIOR

To account for the impact between adjacent batteries, a force-based impact model presented in (Muthukumar, 2003) was adopted. The impact model is simulated as a linear stiffness spring with damping, though, choosing the precise value of the spring stiffness is challenging (Muthukumar, 2003). Several studies have shown that the spring stiffness should be equal to the in-plane axial stiffness of the colliding bodies (Maison and Kasai, 1990; Muthukumar, 2003), while other studies have shown that it should be 20 times the axial stiffness (Anagnostopoulos, 1988). However, Muthukumar (2003) suggested that the spring stiffness should be taken as the elastic stiffness of the impact objects to avoid numerical convergence

problems and impractical high impact forces. Thus, to determine the axial elastic stiffness of the spacer a compression test has been performed. Three specimens were tested with different arrangements; single spacer, three stacked spacers, and five stacked spacers respectively. The axial stiffness of a single spacer was consistent among the three tested specimens and was determined to be 1.4 kN/mm. While the damping ratio (ξ) can be related to the coefficient of restitution (*e*) by

$$\xi = - \frac{ln\,e}{\sqrt{\pi^2 + (ln\,e)^2}} \qquad (1)$$

and is implemented in OpenSees as Rayleigh damping assigned to the zero-length element simulating the spacers and the mass of the batteries. An average value of the coefficient of restitution was taken as 0.7, resulting in a damping ratio of 11%.

Figure 4.16 shows the response of the simulated ABPS with the impact model and the experimental results for SF = 0.5, 1.53, 2.98, and 3.73. These figures show that incorporating the impact model in the numerical simulation of ABPS enhanced the model results compared to the experimental results. The model was able to capture the response of the system at low earthquake levels. However, as the damage increases the difference between the model and the experimental results increase.

To further investigate the effect of the damping in the impact model, the ABPS numerical model was analyzed using different coefficients of restitution. The coefficient of restitution was changed to 0.5 to allow for more energy dissipation

as expected from the Styrofoam spacer, this resulted in a damping ratio of 21%. Figure 4.17 shows the difference between the different models. The figure shows that the change in the coefficient of restitution from 0.7 to 0.5 had a negligible effect on the response. Also, the results of both models show that the ABPS experienced the same damage states at the same earthquake levels.

However, the model was incapable of accurately predicting the damage states reported in the experimental results of Ghith et al. (2019). Table 1 shows the earthquake levels (i.e. scale factors) at which different damage states were observed in the model and the experimental results, respectively. The table shows that the model could predict the macro response of the system.

4.9.   LIMITATIONS OF THE DYNAMIC MODEL

Experimental tests and the OpenSees model focused on the first mode, neglecting the effects of high modes, including the rocking response of individual batteries. Researchers have previously attempted to simulate the rocking response of rigid bodies. For example, Housner (1963).investigated the rocking motion of a rectangular-shaped rigid body block using the response of an inverted pendulum. Housner described the mathematical formulation of the equations of motion of the rocking block, neglecting the sliding motion. Housner suggested that the rocking motion prediction is dependent on describing the amount of energy dissipated through a reduction coefficient, later known as the coefficient of restitution, which is dependent on the ground motion properties.

Subsequently, Shenton and Jones (1991) implemented an impact model originally derived by Kimura and Iida (1934), to describe a mathematical model for the coefficient of restitution. Moreover, Shenton and Jones (1991) studied the mathematical simulation of a rigid body subjected to sliding only, rocking only, and rocking/sliding simultaneously. They described the sliding/rocking motion via two nonlinear coupled equations, that require significant computational effort to solve. However, they ignored more realistic response behaviors, such as changing from one mode to another, since the simulation of the initial conditions is highly complicated.

Nonetheless, Jeong et. al. (2003) predicted the free body rocking/sliding motion of a representative block using time-stepping functions presented by Shenton III and Jones (1991). Jeong et. al. described that initiation of sliding motion produces a more chaotic (i.e. non-periodic) rocking response. Later, Jeong and Yang (2012) verified the chaotic sliding/rocking response using experimental testing. Moreover, Jeong and Yang (2012) suggested that minute changes in the friction coefficient, between static and kinetic friction, affects the predicted rocking/sliding response of the model.

Change from static to dynamic friction could contribute to the large variation of the load-deformation relation of the sliding nuts, almost 35% in the friction force was noticed from the experimental results shown in Fig. 4.2. The model accounted for the sliding of the batteries on the supporting rails that were validated based on static results. However, some researchers (Brechet and Estrin,

1994; Zhao et al., 2001; Abdo and Tahat, 2008; Chowdhury et al., 2011) reported that the friction coefficient is speed-dependent, as the speed of the moving object increases the coefficient of friction decrease. As such, it is postulated that as during dynamic testing the friction between the batteries and the supporting rails is lower than the calibrated static friction.

Bachmann et. al. (2018) compared the predicted rocking motion of rigid block using Housner's model (Housner, 1963), against shake table test results. The authors used measured and theoretically computed coefficients of restitutions in the Housner's model to predict the energy dissipated during impact. It was found that the two models failed to predict the rocking motion of the rigid body, as the model could not predict the occurrence of overturning nor the maximum attained tilt angle. However, using a stochastic model with an ensemble of synthetic generated ground motion time histories using a target response spectrum, the tilt angle of the rocking body could be statistically predicted. Finally, Bachmann et al. (2018) suggested that the rocking response of rigid blocks subjected to earthquakes look chaotic, as the rocking response is highly sensitive to specimen imperfections, interface, and initial conditions.

ElGawady et al. (2010) also observed similar results regarding the sensitivity of the rocking response while performing experimental tests on rigid blocks. They performed experimental free rocking tests on rigid blocks to assess the effects of changing the interface material between concrete, steel, timber, and rubber. It was found that the coefficient of restitution depends not only on the

properties of the rocking body, as previously known but on the interface material. As such, rubber was found to help dissipate energy during impact by storing strain energy compared to other materials.

Vassiliou et al. (2014) attempted to simulate the rocking motion of rigid bodies using OpenSees. The presented OpenSees model doesn't directly model the rocking impact behavior, instead, the presented model employs a nonlinear elastic rotational spring in parallel with a viscous rotational damper to assess the response of flexible rocking bodies. The damper is calibrated to dissipate the same amount of energy in a single cycle. The model was validated against the Housner model (Housner, 1963), previously found to be inaccurate in describing the rocking motion of rigid bodies. Vassiliou et al. (2014) used the model to describe the rocking motion of rectangular bodies under several pulse-like earthquake excitations. However, results show that as the slenderness of the rocking body decreases, the model is unable to capture the response due to the highly nonlinear rocking problem. Moreover, this presented model doesn't account for any sliding motion as the presence of sliding will increase the complexity of the problem.

Finally, as mentioned previously, three rigid body motions have been observed, sliding/rocking/impact modes. The modeling of sliding/rocking/impact simultaneously is a highly nonlinear complex problem that, to the best of the authors' knowledge, has not been addressed to date. Current research has shown that the introduction of the rocking mode to any model increases the nonlinear complexity of that model, as such, research is still needed to develop a sufficient

model that accounts for rocking mode concurrently with other modes. Therefore, in the currently presented OpenSees model, the authors attempted to model the two modes sliding/impact simultaneously. As a result, the currently presented model is limited to static applications, and the model dynamic results are limited to describing the macro response of the system during service level earthquakes.

4.10. CONCLUSIONS

The current study presents the formulation of a detailed 3D model of the ABPS that was developed using OpenSees. The study discusses the modeling of different connections of the ABPS. The model also incorporated the buckling of braces. Furthermore, the model was validated using quasi-static test results on a 2-tier-EP1 ABPS. The same loading protocol used in the quasi-static testing was applied to the modeled ABPS, and good agreement between the model and the experimental results were found in terms of the initial stiffness and the ultimate capacity of the ABPS.

The model together with the experimental results showed that the L-shaped connection between the end rail and the side rail is susceptible to damage, thus limiting the capacity of the total system. As such, the potential to seismically upgrade the ABPS by the addition of extra bracing was investigated. The lateral performance of eight ABPS configurations having different tiers, lengths, and seismic categories was evaluated. The addition of braces enhanced the initial lateral

stiffness, however, different ABPS were shown to have almost the same yielding capacity governed by the use of the same L-shaped connection.

Subsequently, in an effort to validate the model results dynamically, dynamic shake table results performed on similar ABPS were considered. As such, an impact element model was developed to capture the dissipation of energy during the opening and closing of the gap between adjacent batteries. Discrepancies between the model output and experimental results remained in terms of the total response and the damage propagation. This was attributed to the contribution of higher mode effects including the rocking motion of individual batteries. However, modeling of the total rigid body motion of individual batteries in terms of rocking/sliding/impact is known to be a highly nonlinear complex problem which is challenging and hard to model. Finally, the above-presented model is limited to static applications, and further research is still needed in order to find new techniques to incorporate higher mode effects and help solve the high nonlinear complex problem of modeling rocking/sliding/impact simultaneously.

4.11. ACKNOWLEDGMENT

program. Special thanks go to the McMaster University Applied Dynamic Laboratory (ADL) staff.

4.12. REFERENCES

Abdo, J., & Tahat, M. (2008). The Effect of Frequency and Amplitude of Vibration on the Coefficient of Friction for Metals. *3*(7), 265-274.

Anagnostopoulos, S. (1988). Pounding of buildings in series during earthquakes. *16*, 443-456.

Avallone, E. a. (2017). *Mark's standard handbook for mechanical engineers.* McGraw-Hill.

Bachmann, J., Strand, M., Vassiliou, M., Broccardo, M., & Stojadinovic, B. (2018). Is rocking motion predictable? *Earthquake engineering and engineering structures, 47*, 535-552.

Batterman, R., & Bruce, G. (1967). Behavior and maximum strength of metal columns. *93*(2), 205-230.

Berak, E., & Marconi Communications. (2005). Modal testing and finite element analysis of a battery rack for seismic applications. *Journal of the IEST, 48*(1).

Brechet, Y., & Estrin, Y. (1994). The effect of strain rate sensitivity on dynamic friction of metals. *30*(11).

C&D Technologies Inc. (2017). Retrieved from http://www.cdtechno.com/

Choun, Y.-S., Choi, I.-K., & Seo, J.-M. (2008). Improvement of the seismic safety of existing nuclear power plants by an increase of the component seismic capacity: A case study. *Nuclear Engineering and Design, 238*(6), 1410-1420.

Chowdhury, M., Khalil, M., Nuruzzaman, D., & Rahaman, M. (2011). the effect of sliding speed and normal load on friction and wear property of aluminum. *11*(1), 53-57.

CSA S16-14. (2014). *Design of steel structures.* Toronto, ON, Canada: Canadian Standards Association (CSA) group.

ElGawady, M., Ma, Q., Butterworth, J., & Ingham, J. (2010). Effects of interface material on the performance of free rocking blocks. *Earthquake engineering and structural dynamics, 40*(4), 375-392.

Ellobody, E., & Young, B. (2006). Nonlinear analysis of concrete-filled steel SHS and RHS columns. *Thin Walled Structures*, 919-930.

EPRI. (1991). *Generic Seismic Ruggedness of Power Plant Equipment.* Oakland, CA: Electric Power Research Institute (EPRI) NP-5223-SL Revision 1.

FEMA 461. (2007). *Interim testing protocols for determining the seismic performance characteristics of structural and nonstructural components.* Federal Emergency Management Agency (FEMA).

Ghith, A., Ezzeldin, M., Tait, M., & El-Dakhakhni, W. (2019). Performance of battery rack auxiliary power systems under FEMA 461 Quasi-static seismic loading protocol, prepared for submission to Journal of structures.

Ghith, A., Ezzeldin, M., Tait, M., & El-Dakhakhni, W. (2019). Shake table seismic performance assessment of auxiliary battery power systems using FEMA 461 protocol. *Journal of Structural Engineering, 145*(8).

Gunnarsson, I. (2004). *Numerical performance evaluation of braced frame systems, MSc thesis.* Seattle: University of Washington.

Housner, G. (1963). The behavior of inverted pendulum structures during earthquakes. *Bulletin of the Seismological Society of America, 53*(2), 403-417.

Jeong, M., Suzuki, K., & Yim, S. (2003). Chaotic rocking behavior of freestanding objects with sliding motion. *Journal of sound and vibration, 262*, 1091-1112.

Jeong, M.-Y., & Yang, I.-Y. (2012). Characterization o the rocking vibration of rigid blocks under horizontal harmonic excitations. *International Journal of Precision engineering and manufacturing, 13*(2), 229-236.

Johnson, G., Sheppard, R., Quilici, M., Eder, S., & Scawthorn, C. (1999). *Seismic reliability assessment of critical facilities: a handbook, supporting documentation, and model code provisions.* Oakland, California: MCEER.

Kimura, H., & Iida, K. (1934). On rocking of rectangular columns (I). *Zisin, 6*(3), 125-149.

Kumar, V., Sinha, S., & Agarwal, A. (2014). *Tribology of Epoxy Composites (Graphene and Graphite) Coatings on Steel in Dry and Lubricated Conditions.*

Maison, B., & Kasai, K. (1990). Analysis for type of structural pounding. *116*(4), 957-975.

McFadden, P., & Smith, J. (1984). Vibration monitoring of rolling element bearings by the high frequency resonance technique - a review. *Tribology International, 17*(1), 3-10.

McKenna, F. F. (2016). Open System for Earthquake Engineering Simulation. *Version 2.5.0*. University of California, Berkeley, CA,2000. Retrieved from http://opensees.berkeley.edu

Mihu, G., Mihalache, I., Graur, I., Ungureanu, C., & Bria, V. (2017). Comparative study regarding friction coefficient for three epoxy resins. *13th International Conference on Tribology.*

Muthukumar, S. (2003). *A contact element approach with hysteresis damping for the analysis and design of pounding in bridges, Ph.D. thesis.* Georgia Institute of Technology.

NAIIC, T. F. (2011). The National Diet of Japan.

Porter, K. (2009). *Fragility of Battery Racks.* Washington, D.C.: Federal Emergency Management Agency (FEMA) FEMA P-58 /BD-3.9.26.

Sabino-Netto, A., Salmoria, G., Ahrens, C., & Pouzada, A. (2008). Friction Properties of Steel Fiber Reinforced Epoxy Composites Used in Molding Blocks of Hybrid Molds. *Materials Science Forum*, 217-221.

Salmon, C., Johnson, J., & Malhas, F. (2008). *Steel Structures: Design and Behavior.* Pearson Higher Ed USA.

Shenton III, H., & Jones, N. (1991). Base excitation of rigid bodies I: Formulation. *117*(10), 2286-2306.

Shi, Z., & Fan, J. (2018). Analytical investigation on effective elastic stiffness of eccentric steel beam-column joints. *Advances in Structural Engineering*, 125-137.

SQUG. (2017). Retrieved from http://www.squg.mpr.com

Terzic, V. (2013). Modeling SCB frames using beam-column elements. Seminar OpenSees. http://opensees.Berkeley.edu.

Vassiliou, M., Mackie, K., & Stojadinovic, B. (2014). Dynamic response analysis of solitary flexible rocking bodies: modeling and behavior under pulse-like ground excitation. *Earthquake engineering and structural dynamics, 43*, 1463-1481.

Zhao, H., Barber, G., & Liu, J. (2001). Friction and wear in high speed sliding with and without electrical current. *249*(5-6).

Table 4.1. Damage states for experimental and model results

Damage states	Experimental tests SF (PGA)	Model
DS1 (sliding of t-nuts)	1.53 (0.56g)	N/A
DS2 yielding of braces	1.53 (0.56g)	5.82 (3.28g)
DS3 breakage of conductor	1.91 (0.7g)	N/A
DS4 maximum response	4.66 (2.27g)	3.73 (1.3g)

Figure 4.1: Quasi-static testing of 2-tier-1-step ABPS configuration.

(a)

(b)

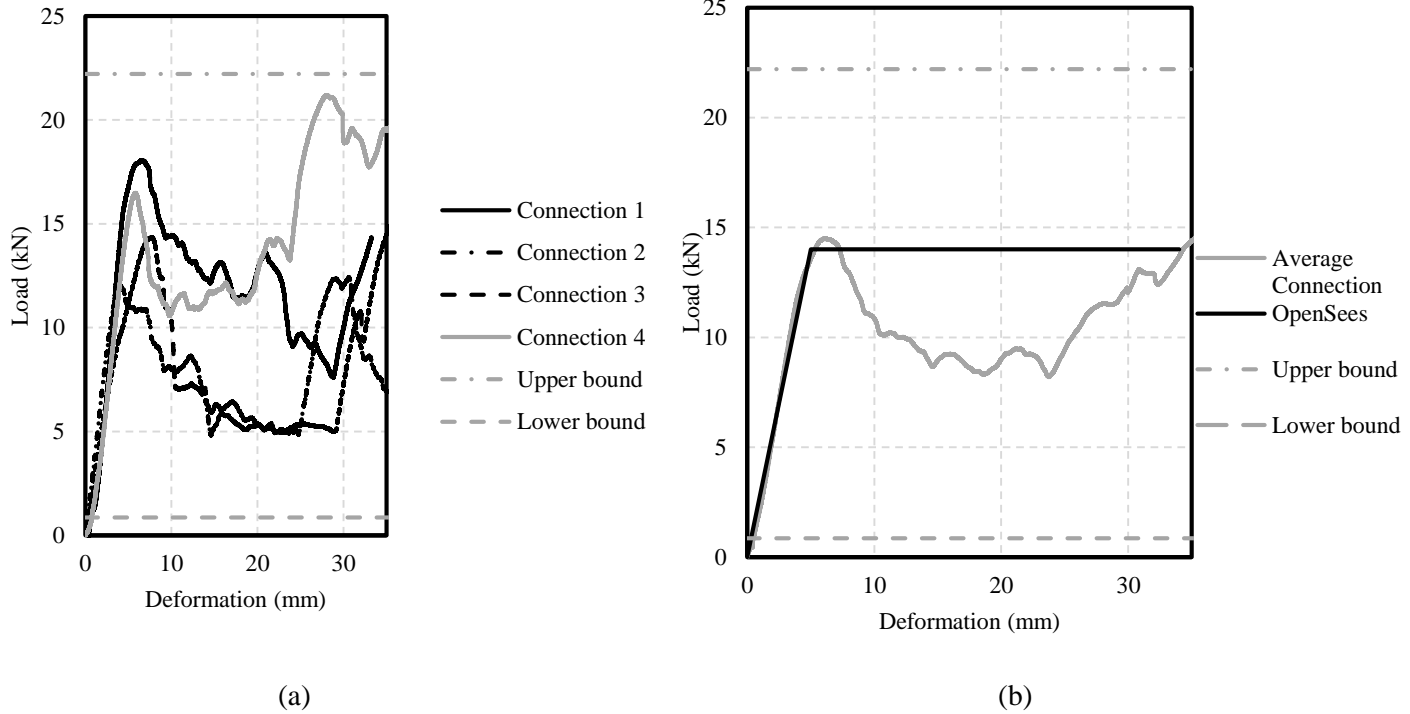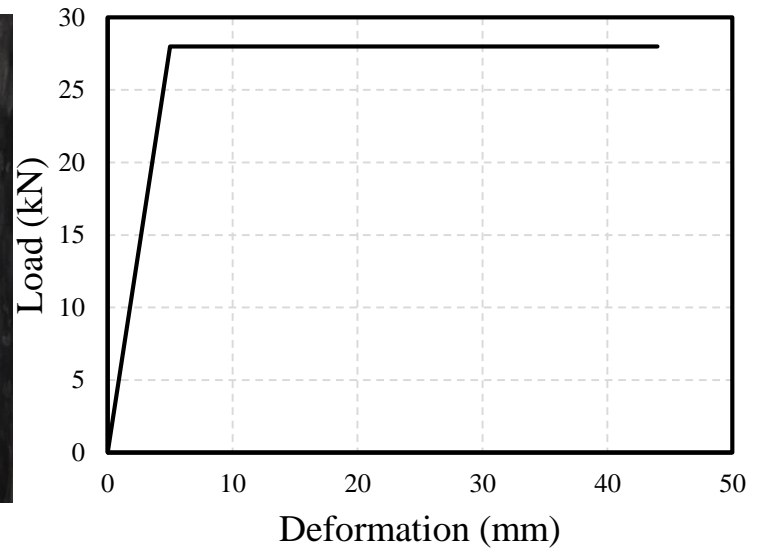Figure 4.2: T-sliding nut behavior; (a) results of the experimental test; (b) average of the experimental tests and the idealized response.

(a)   (b)

Figure 4.3: L-shaped connection behavior: (a) connection between the side rail to L-shaped connection; (b) idealized response of the L-shaped connection.
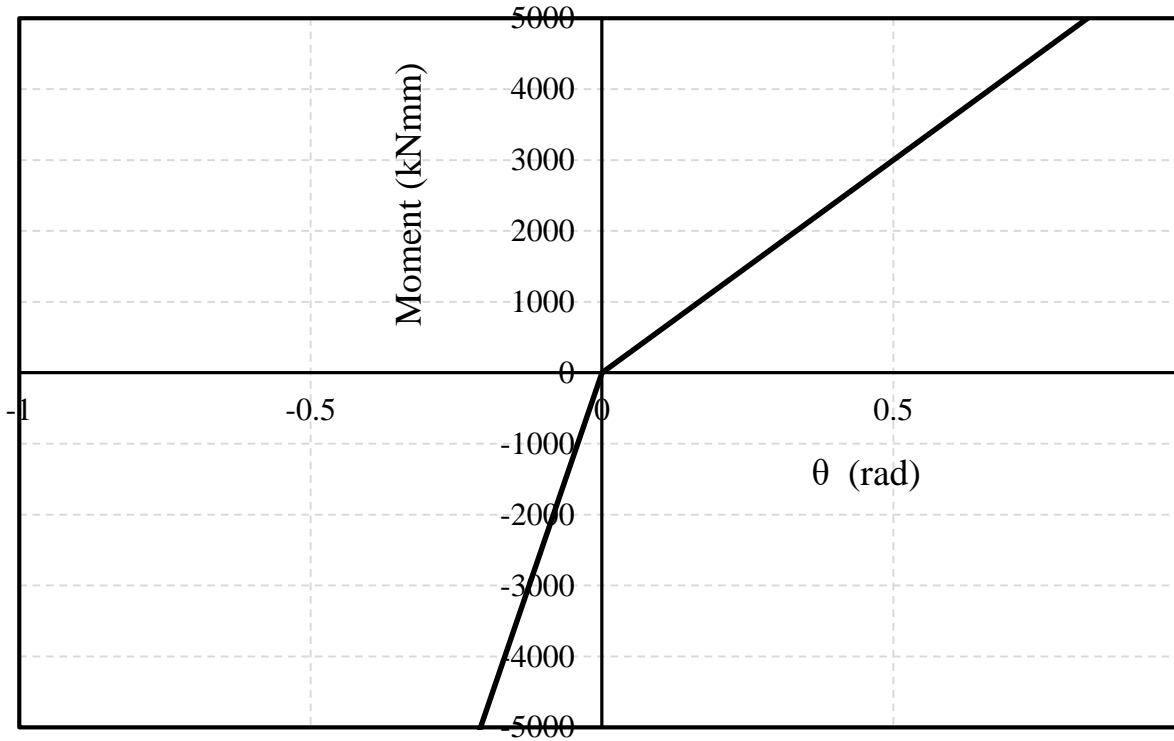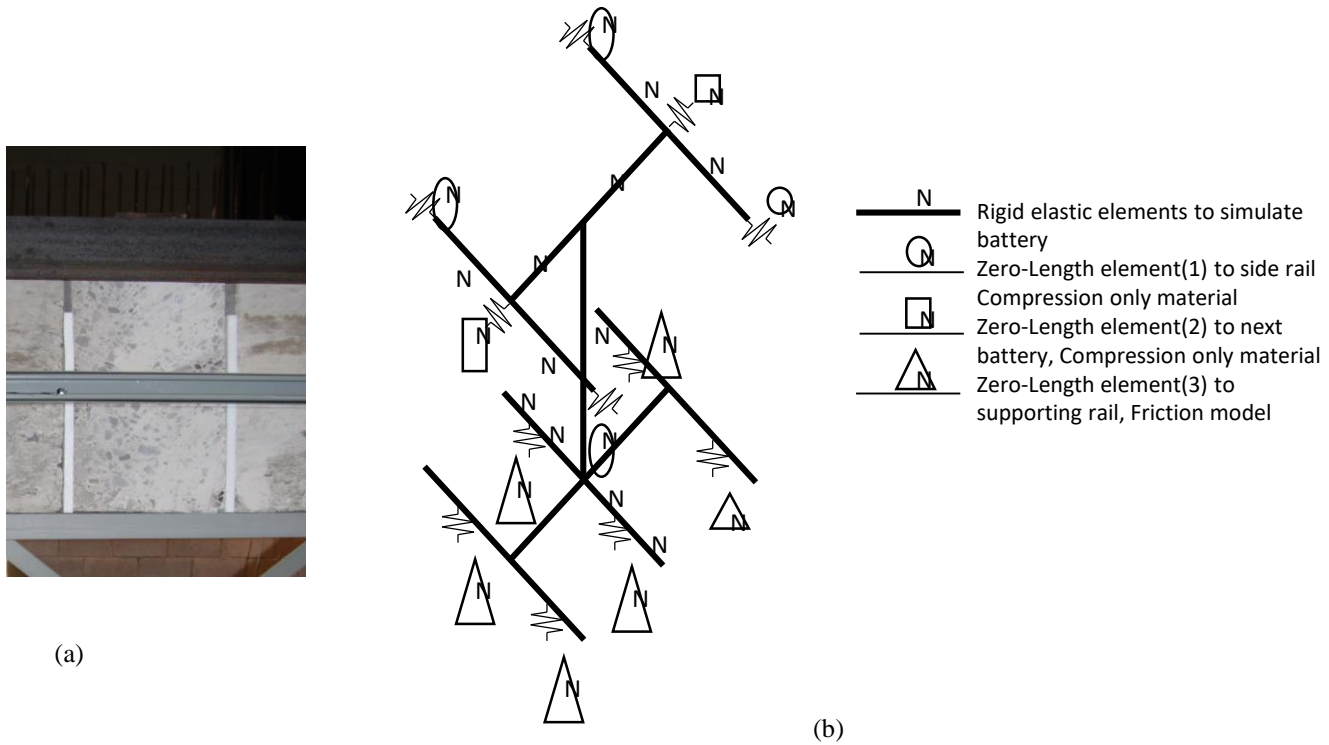
Figure 4.4: Support behavior.

Figure 4.5: Battery simulation: (a) intermediate batter; (b) battery model.
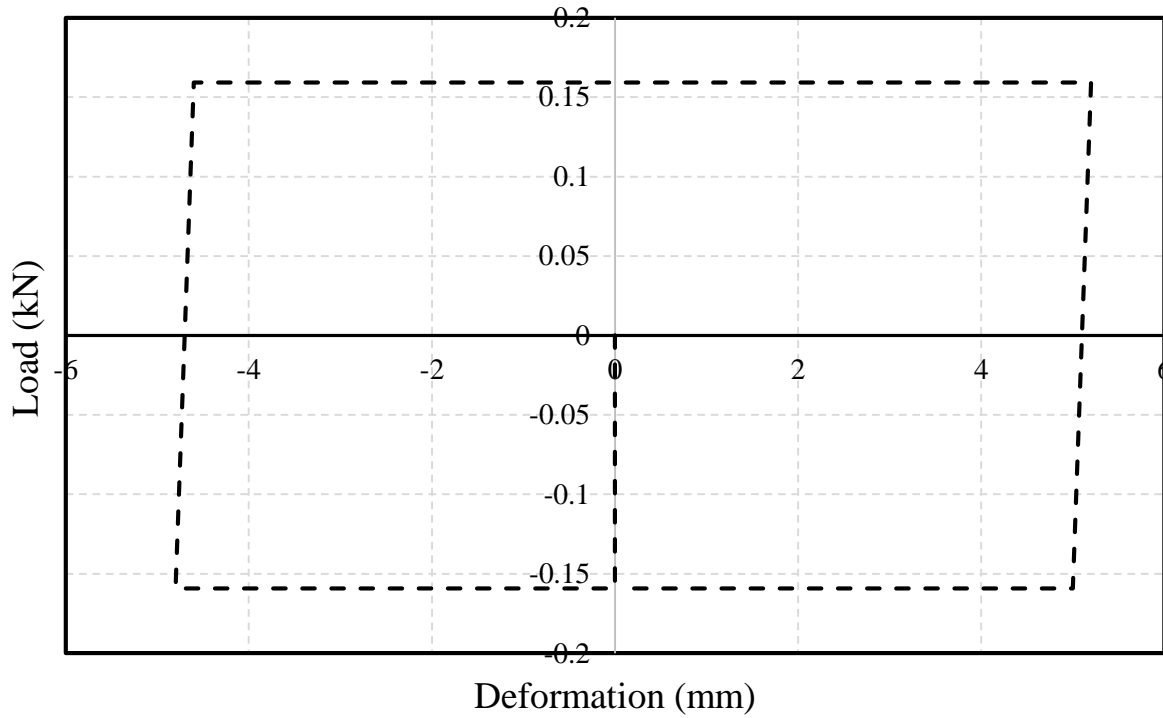
Figure 4.6: Friction model.
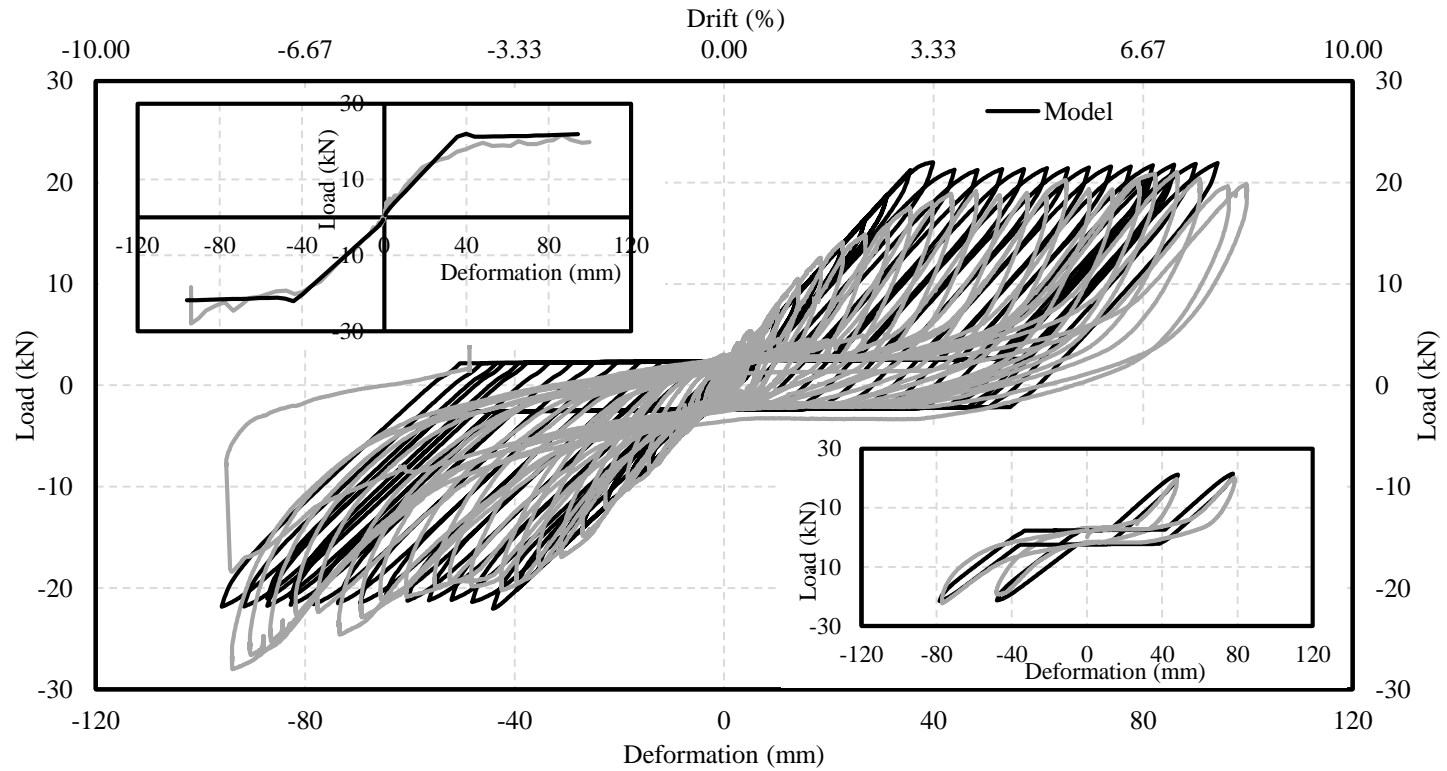
Figure 4.7: Model cyclic response vs experimental hysteretic behavior.
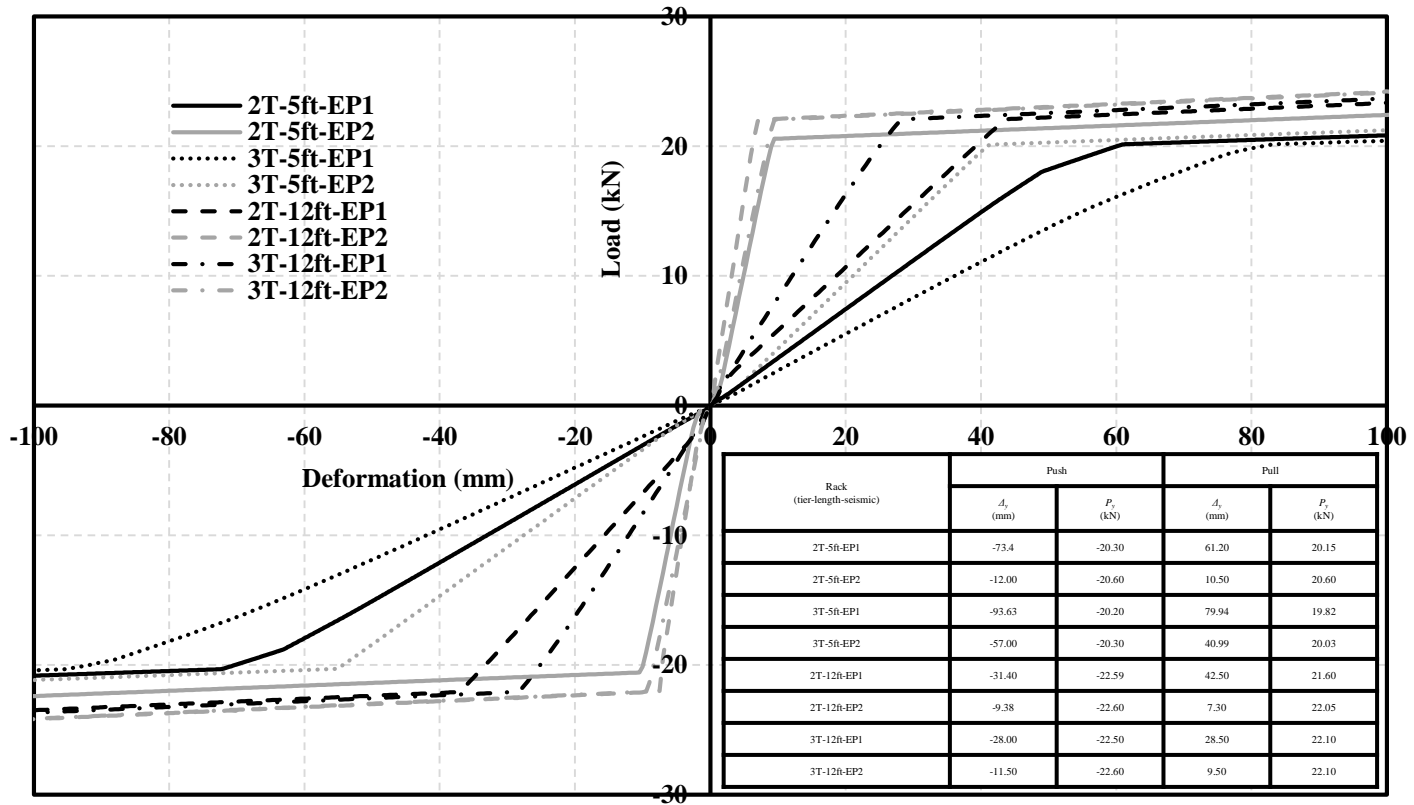
Figure 4.8: Load-displacement relation for different racks.

Rack (tier-length-seismic)	Push		Pull	
	Δ_y (mm)	P_y (kN)	Δ_y (mm)	P_y (kN)
2T-5ft-EP1	-73.4	-20.30	61.20	20.15
2T-5ft-EP2	-12.00	-20.60	10.50	20.60
3T-5ft-EP1	-93.63	-20.20	79.94	19.82
3T-5ft-EP2	-57.00	-20.30	40.99	20.03
2T-12ft-EP1	-31.40	-22.59	42.50	21.60
2T-12ft-EP2	-9.38	-22.60	7.30	22.05
3T-12ft-EP1	-28.00	-22.50	28.50	22.10
3T-12ft-EP2	-11.50	-22.60	9.50	22.10
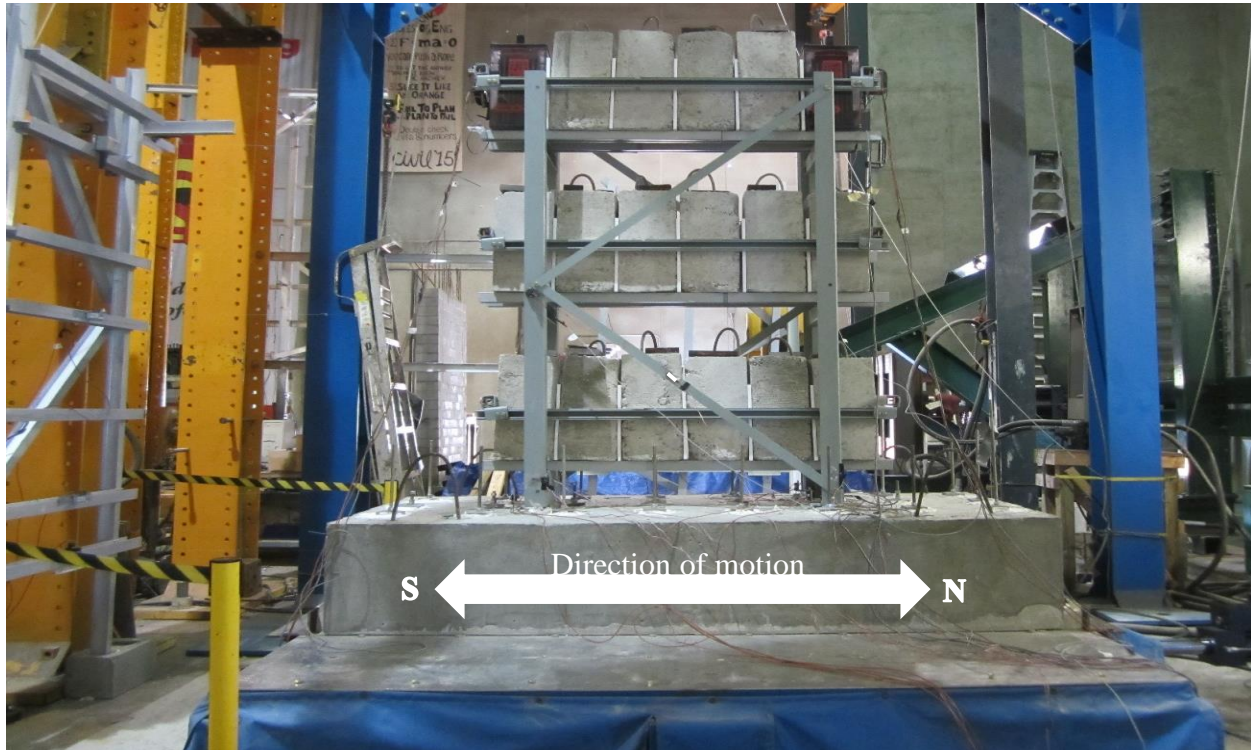
Figure 4.9: Shake table test of 3-tier-1-step ABPS configurations (Ghith et. al. 2019).
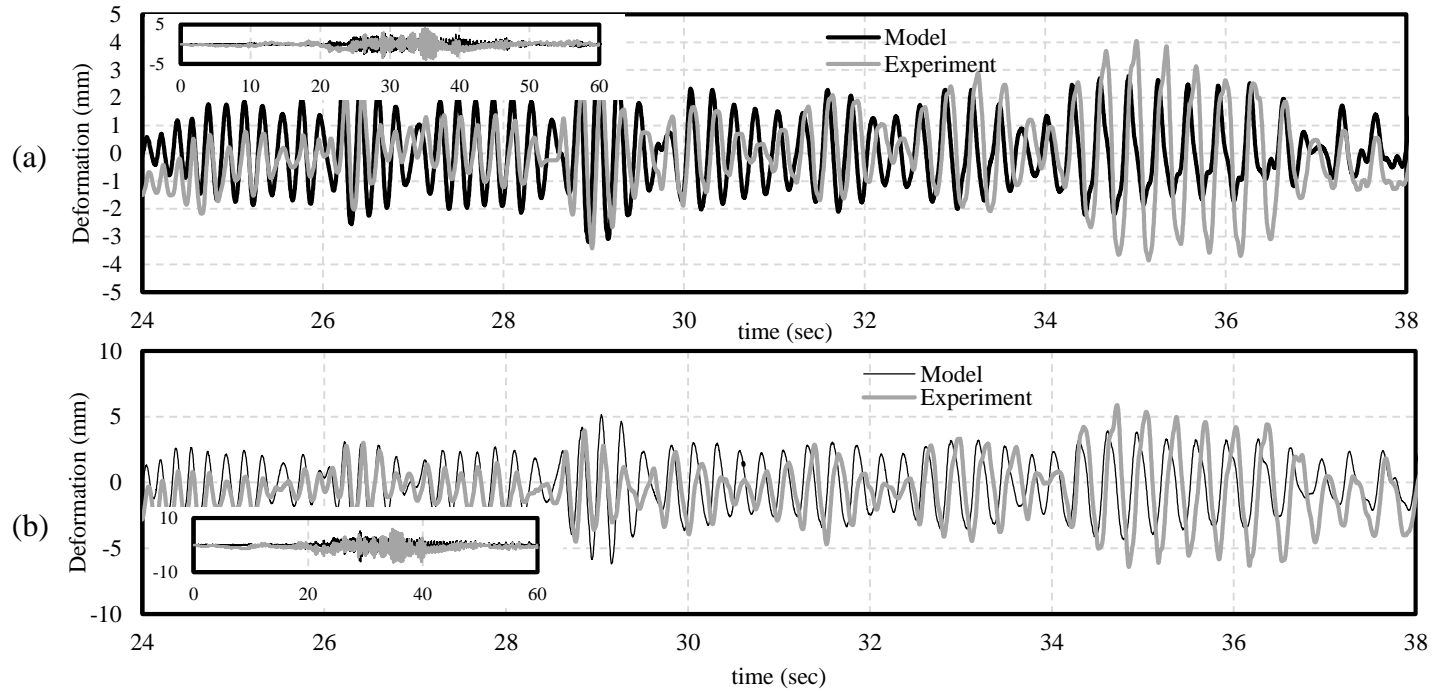
Figure 4.10: Original model: (a) SF=0.625; (b) SF=1.22.
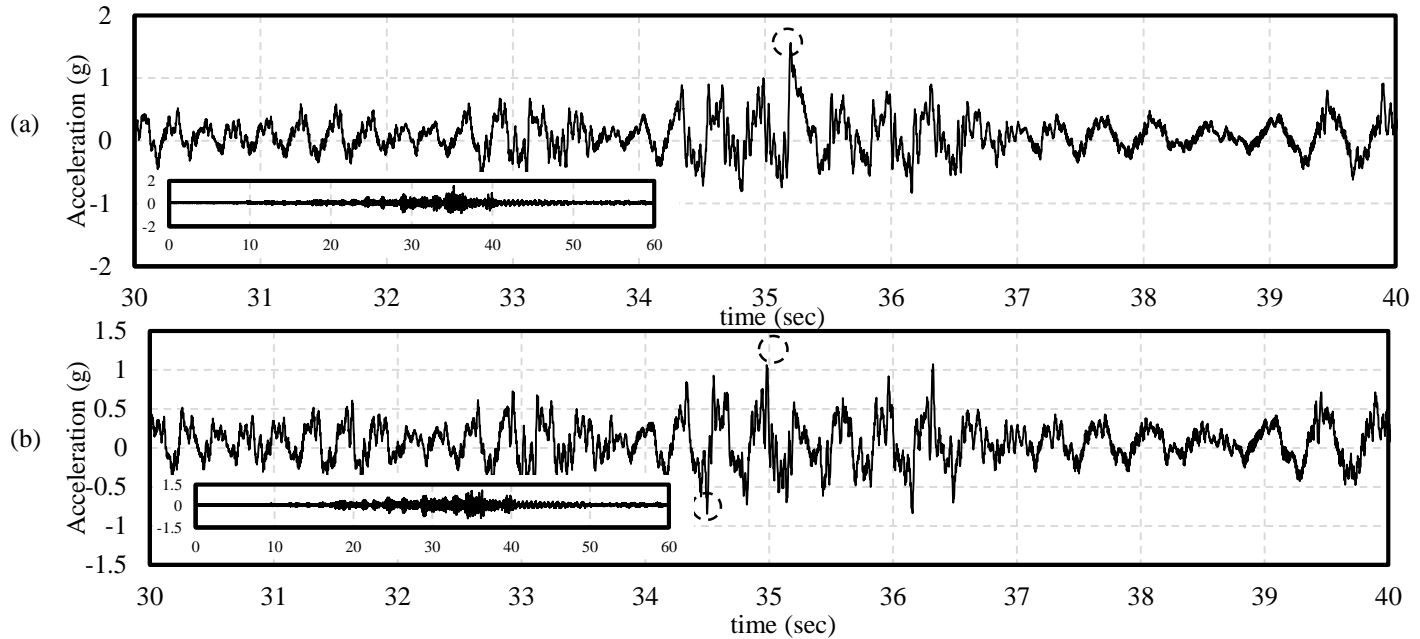
Figure 4.11 : Recorded acceleration for SF = 1.526 showing spikes indicating impact response (spikes are shown in circles): (a) third floor; (b) second floor.
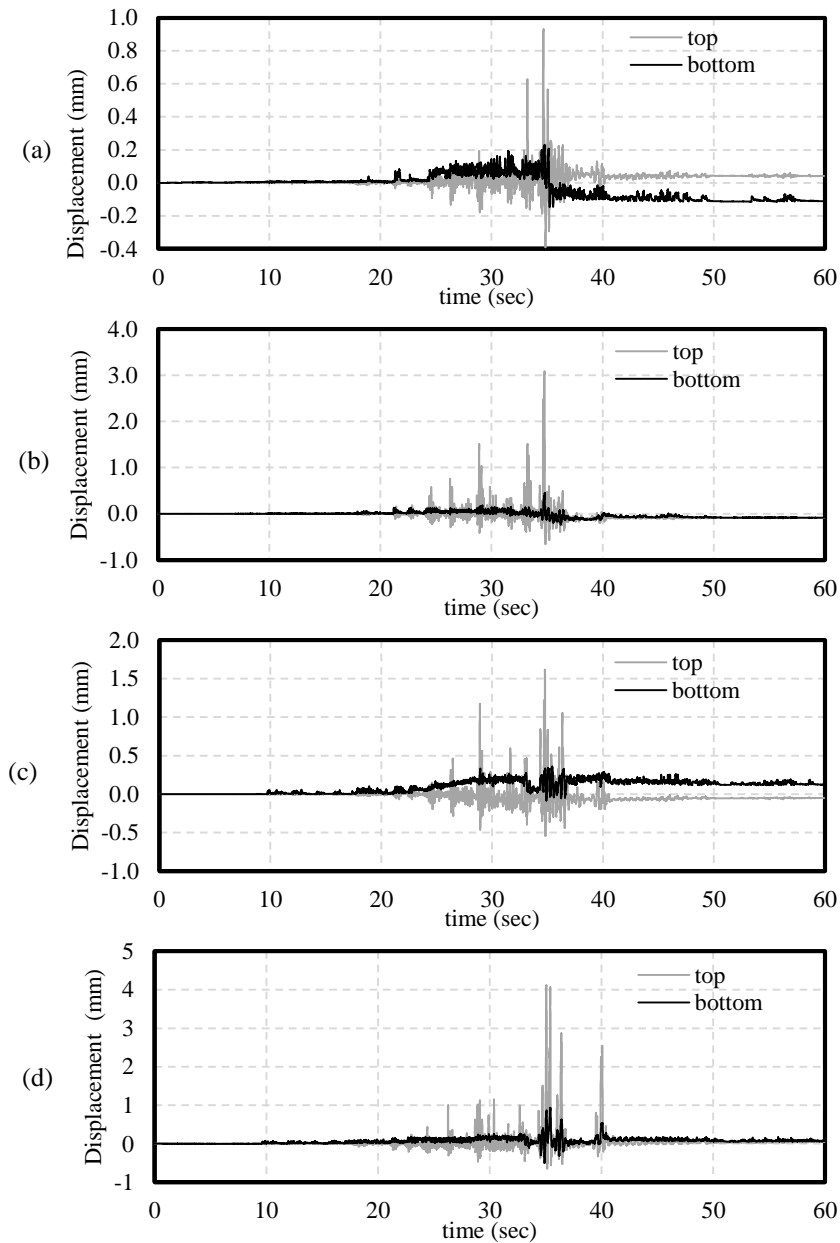
Figure 4.12: Response of the left battery relative to the rack: (a) SF= 0.79; (b) SF= 0.97; (c) SF= 1.22; (d) SF= 1.53.
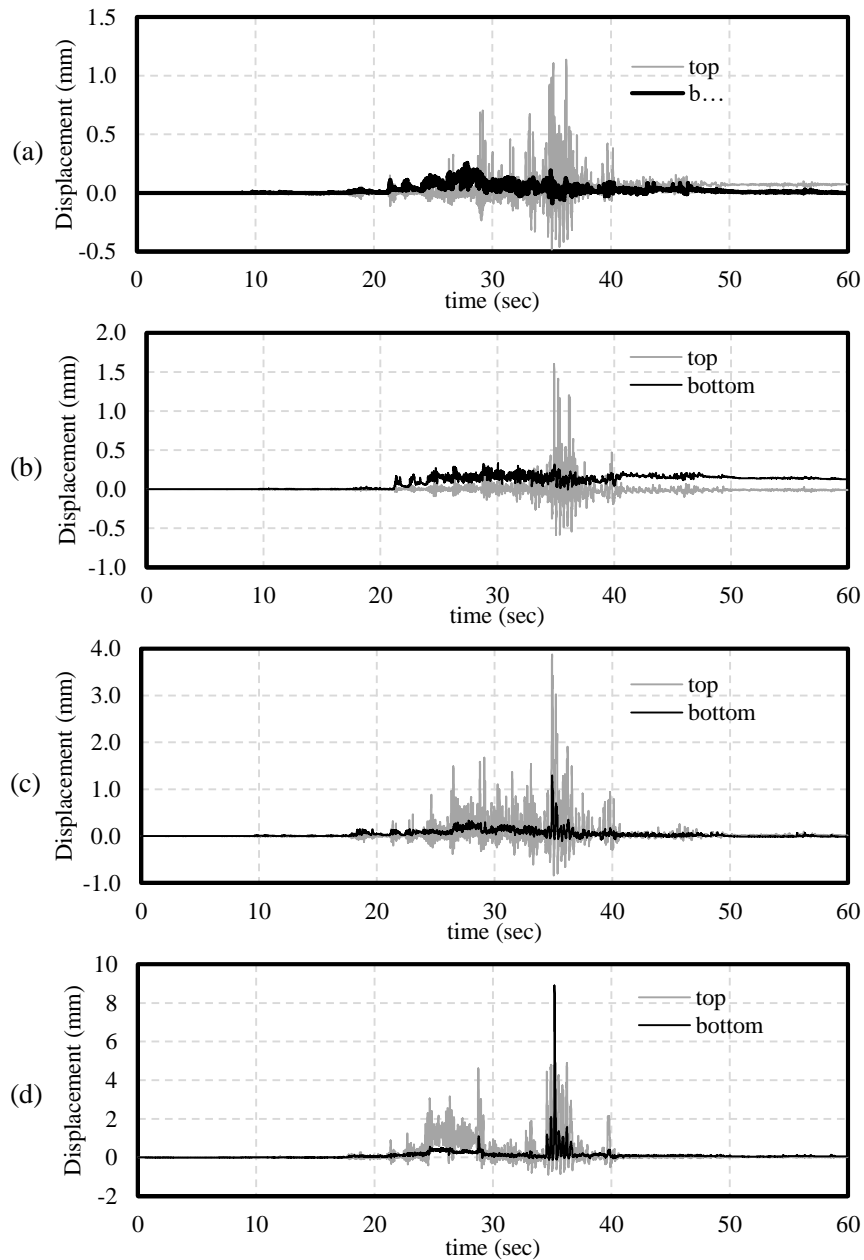
Figure 4.13: Response of the right battery relative to the rack:
(a) SF= 0.79; (b) SF= 0.97; (c) SF= 1.22; (d) SF= 1.53.

Figure 4.14: Movement of the batteries in the top tier on the rack showing rocking motion.
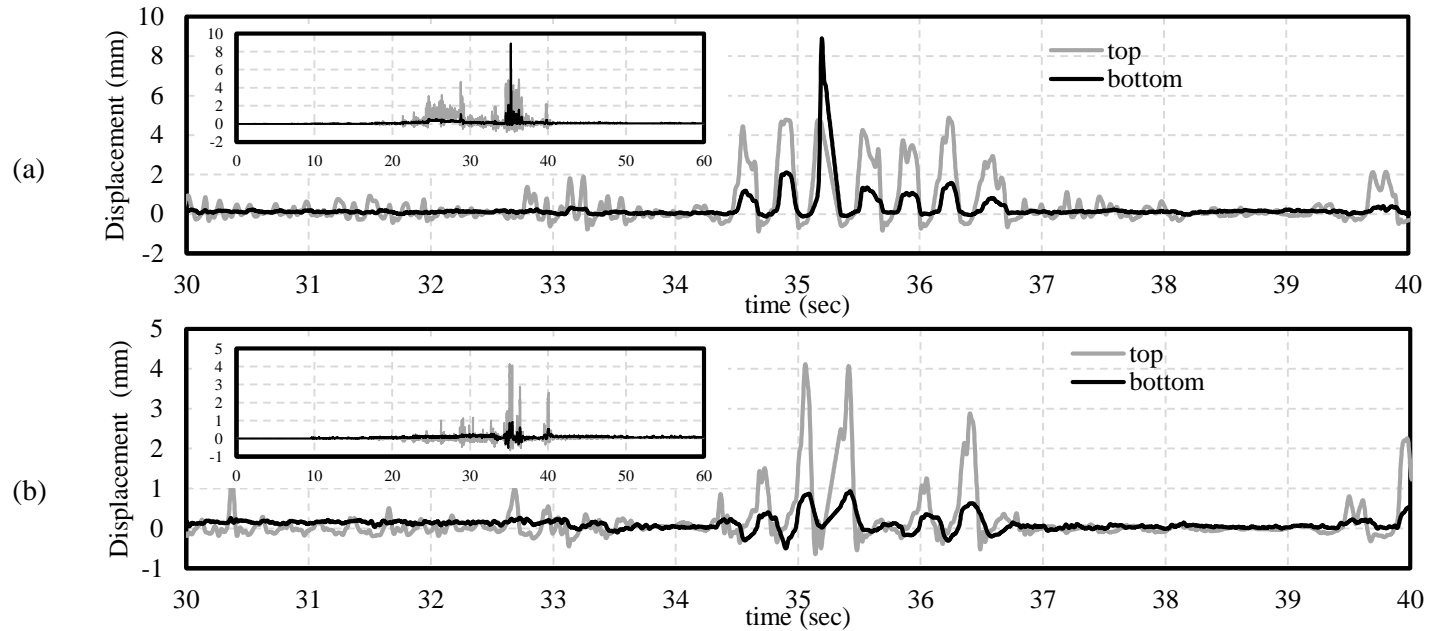
Figure 4.15: LVDT response of the batteries relative to the rack respectively showing rocking for SF 1.526: (a) left; (b) right.
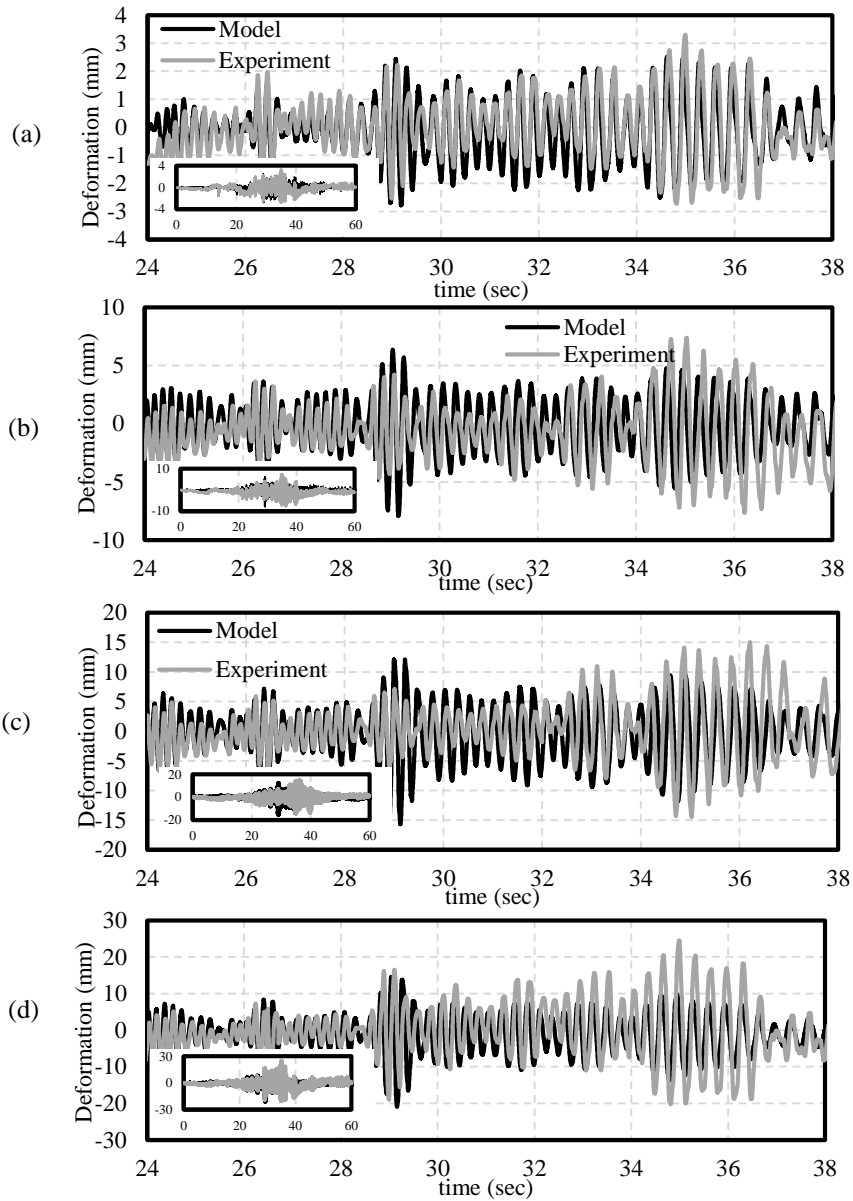
Figure 4.16: Model response with impact element vs experimental response: (a) SF = 0.5; (b) SF = 1.526, (c) SF = 2.98; (d) SF = 3.73.
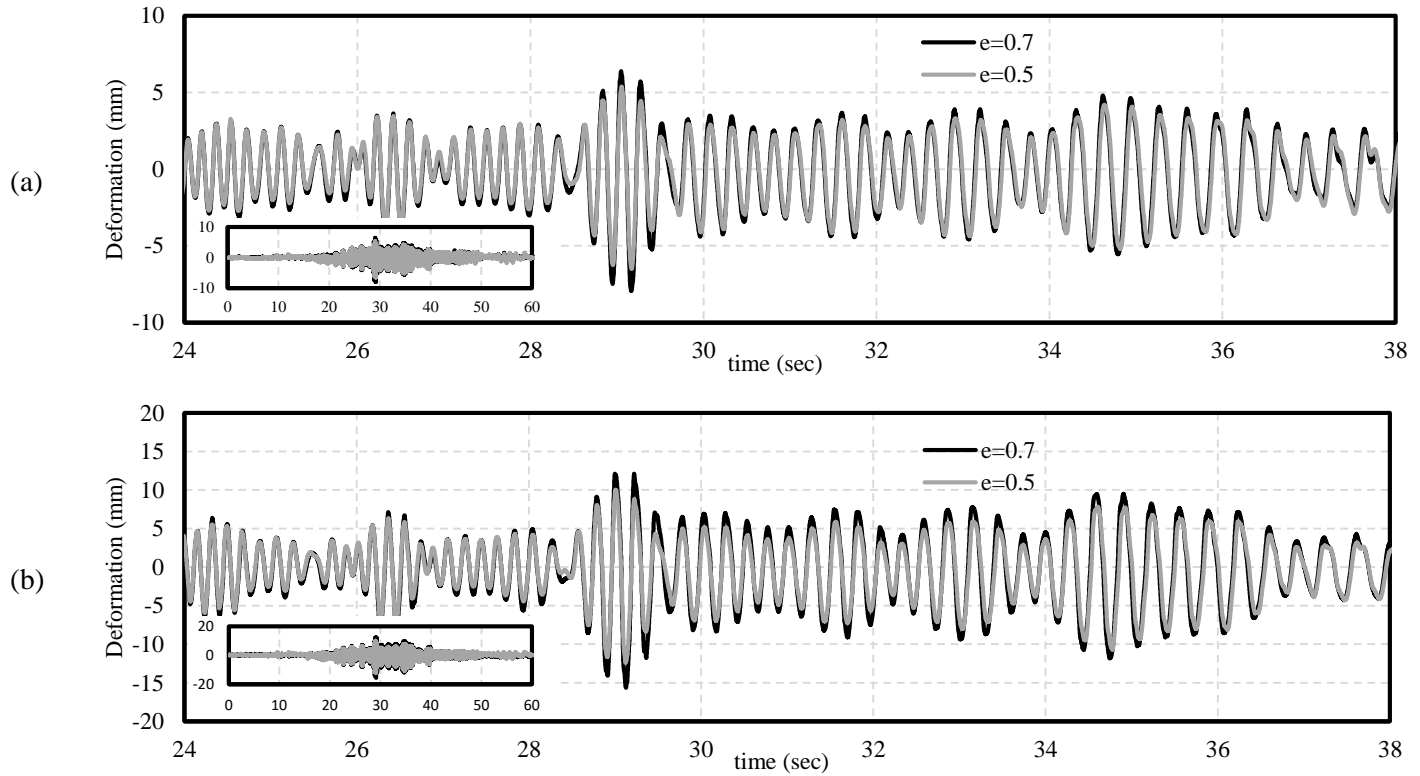
Figure 4.17: model response with different e: (a) SF= 1.526; (b) SF= 2.98.

CHAPTER 5

5. SUMMARY, CONCLUSIONS, AND RECOMMENDATIONS

5.1. SUMMARY

There is an increasing need to evaluate the possible failure modes for safety-related components in Nuclear Power Plants (NPPs) to be incorporated in the post-Fukushima Beyond Design Basis Events (BDBE) design requirements. As such, this study presents the results of the investigation of the failure behavior of commercially available Auxiliary Battery Power System (ABPS). The ABPS was tested in a fully reversed cyclic displacement control quasi-static manner to describe the hysteretic behavior of the system and different elements' performance. Using first principles, a mechanistic model of the ABPS was calibrated to assess the use of new formulation techniques for ABPS. Furthermore, due to the presence of freely moving batteries, the ABPS was tested under increasing dynamic shake table loading. Battery movement, as well as the rack overall response, were monitored during testing. Possible different damage states were carefully observed, and the corresponding demands were documented. Finally, an OpenSees 3D model of the ABPS was developed and validated using the experimental results. The model was used to assess the lateral performance of several ABPS supplied by the same manufacturer. Finally, the limitations of the model are presented.

5.2. CONCLUSIONS

The results in this dissertation highlight the difference between the observed performance of laboratory-controlled lateral performance tests of ABPSs operational/existing in NPPs and literature. Moreover, an underlying conclusion of this study is the need to investigate the failure modes of other safety-related components and ensure their compliance with the BDBE design requirements. In this context, the following conclusions are drawn:

- The results of a fully reversed quasi-static displacement control test of a two-tier-one-step ABPS configuration showed that the braces buckled under lower lateral loads, as expected to dissipate energy. The lateral hysteretic behavior of the ABPS showed that the later capacity was largely dependent on the behavior of the L-shaped connection. This L-shaped connection transfers the bearing load of the batteries on the end rails to the side rails.

- A mechanistic model of the Quasi-static tested rack, based on the first principles, was developed. The results of this mechanistic model confirmed that the lateral performance of the ABPS was largely dependent on the performance of the L-shaped connection. Hence, increasing the thickness of the L-shaped connection can enhance the total lateral performance of the ABPS.

- The results of this mechanistic model have also shown that the use of C-channeled cross-sectional elements with eccentric sliding nuts, to ease the in-situ installation, lowered the lateral stiffness of the whole ABPS.

- Due to the presence of free moving batteries in the ABPS, the ABPS was tested dynamically to observe the movement of the batteries and possible dynamic damage states. The results of the dynamic shake table test have shown that the use of sliding nuts was the dominant failure mechanism. The slip of these nuts directly affected the configuration of the ABPS resulting in permanent buckling of the braces. Excessive buckling of these braces at higher intensities resulted in their yielding. Moreover, the sliding of the batteries and impact against the end rail caused the slip of the sliding nuts between the L-shaped connection and the side rail.

- The results of this dynamic testing were incorporated with the EPRI 2002 "*Seismic fragility application guide*" to perform fragility analysis. Hence, four damage states were observed from the experimental results; the slippage of sliding nuts, the yielding of the braces, the excess movement of the batteries that led to conductor breakage, and the exceedance in lateral response relative to the allowable limits. These damage states and their corresponding fragility curves were presented and compared to fragility curves found in the literature. This comparison showed that fragility curves in literature were unconservative and need further investigation.

- A detailed 3D OpenSees model was developed to be used to assess the lateral performance of ABPS. The comprehensive model incorporated the different connections' simulations; the translation and rotational behavior of the sliding

nut connections, and the rotational behavior at the support at the bottom of the columns. The model was in good agreement with the quasi-static results, the model was able to capture the initial stiffness, the yielding displacement, and the ultimate capacity of the ABPS.

• The manufacturer indicated that the seismic upgradability of the ABPS is performed by adding additional bracing while reserving the main frame elements. This upgrade was investigated and the lateral capacity of the ABPS was determined to be limited by the behavior of a main frame element (i.e. the L-shaped connection). Pushover analysis of eight different configurations of ABPS with different seismic categories was performed. The results of the pushover simulations showed that the different ABPSs had nearly the same ultimate capacity which was dependent on the L-shaped connection, however additional bracing resulted in an increase in the initial stiffness of the system.

• In an effort to validate the model against the dynamic results, the 3D rigid body motion of the batteries (i.e. rocking/sliding/impact) was modeled. The modified model incorporating sliding/impact showed good agreement to the experimental results in terms of the lateral response at service level earthquakes. However, the modified model was not able to capture the response of the ABPS at higher earthquake levels. The model was not able to capture all the damage states from the dynamic experimental results. The rocking/sliding/impact behavior of the batteries is characterized as being chaotic and hard to predict.

As such, the results of the presented model are limited to static evaluation of the lateral performance of ABPS.

5.3. RECOMMENDATIONS

This section presents the proposed future research to continue on the assessment of failure modes of safety-related components in NPPs:

1. The results of this dissertation showed that there is a real need to even further investigate other safety-related components and assess their compliance with new BDBE design requirements.

2. The results of this experimental study were limited to one type of racks, further research is still needed to assess the behavior of other rack types that can house different types of nuclear grade batteries.

3. The results of this study have shown that fragility curves found in literature could be unreliable in assessing the failure modes of ABPS and further research is still needed to develop more robust fragility curves.

4. Model results have shown that different types of ABPS had almost the same ultimate capacity, and the addition of extra braces did not affect the ultimate capacity. As such, experimental research is still needed to confirm these results, and accordingly, further investigation of the design procedure of these ABPS must be performed.

5. The chaotic behavior of the rocking/sliding/impact mode of the batteries needs further investigation, since accurate modeling of this performance will contribute to the accurate simulation of the different damage states.

6. Further investigation of the effects of the higher modes is still needed. The experimental tests performed focused on the natural modes and ignored the contributions of higher modes.

6. APPENDIX A

This appendix describes the instrumentation used during experimental testing.

1) Data acquisition:

   - Dynamic test: National Instrument compact DAQ type data acquisition system. Data measured were then filtered using a digital low-pass Butterworth filter implemented in Matlab, having a corner frequency of 30 Hz, as recommended by the FEMA 461.

   - Quasi-Static test: 2 Agilent 34970A data logger with 4 34901A – 20 channel Multiplexer cards.

2) A 10-volt power supply was used during both testing

3) Instrumentation used in dynamic testing

Instrumentation	type	Gauge length
D1	String Pot	500 mm
D2	String Pot	500 mm
D3	String Pot	500 mm
D4	String Pot	500 mm
D5	Linear potentiometer	1 in
D6	Linear potentiometer	1 in
D7	Linear potentiometer	1 in
D8	Linear potentiometer	1 in

D9	String Pot	250 mm
D10	String Pot	250 mm
D11	Linear potentiometer	1 in
D12	Linear potentiometer	1 in
D13	Linear potentiometer	1 in
D14	Linear potentiometer	1 in
D15	Linear potentiometer	1 in
D16	Linear potentiometer	1 in
D17	String Pot	100 mm
A1	Accelerometer	±5g
A2	Accelerometer	±5g
A3	Accelerometer	±5g
S1	Strain gauge	10 mm
S2	Strain gauge	10 mm
S3	Strain gauge	10 mm
S4	Strain gauge	10 mm
S5	Strain gauge	10 mm
S5	Strain gauge	10 mm
S6	Strain gauge	10 mm
S7	Strain gauge	10 mm

S8	Strain gauge	10 mm
S9	Strain gauge	10 mm
S10	Strain gauge	10 mm
S11	Strain gauge	10 mm

4) Instrumentation used in Static testing

Instrumentation	type	Gauge length
D1	String Pot	250 mm
D2	String Pot	250 mm
D3	String Pot	250 mm
D4	String Pot	250 mm
D5	String Pot	250 mm
D6	String Pot	250 mm
D7	String Pot	250 mm
D8	String Pot	250 mm
D9	String Pot	5 in
D10	String Pot	5 in
D11	String Pot	5 in
D12	String Pot	5 in
D13	String Pot	5 in

D14	String Pot	5 in
D15	String Pot	5 in
D16	String Pot	5 in
D17	String Pot	5 in
D18	String Pot	5 in
D19	String Pot	5 in
D20	String Pot	5 in
D21	String Pot	5 in
D22	Strain gauge	5 in
D23	Strain gauge	5 in
D24	Strain gauge	5 in
D25	Strain gauge	5 in
D26	Strain gauge	5 in
D27	Strain gauge	5 in
D28	Strain gauge	5 in
D29	Strain gauge	5 in
D30	Strain gauge	5 in
D31	Strain gauge	5 in
D32	Strain gauge	5 in
D33	String Pot	5 in

D34	String Pot	5 in
D35	String Pot	5 in
D36	String Pot	5 in
D37	Linear Potentiometer	2 in
D38	Linear Potentiometer	2 in
D39	Linear Potentiometer	2 in
D40	Linear Potentiometer	2 in
D41	Linear Potentiometer	2 in
D42	Linear Potentiometer	2 in
D43	Linear Potentiometer	2 in
D44	Linear Potentiometer	2 in
D45	String Pot	2 in
D46	String Pot	2 in
D47	String Pot	2 in
D48	String Pot	2 in
D49	String Pot	2 in
D50	String Pot	2 in
D51	String Pot	2 in
D52	String Pot	2 in
D53	Linear Potentiometer	4 in

D54	Linear Potentiometer	4 in
D55	Linear Potentiometer	4 in
D56	Linear Potentiometer	4 in
S1	Strain gauge	10 mm
S2	Strain gauge	10 mm
S3	Strain gauge	10 mm
S4	Strain gauge	10 mm
S5	Strain gauge	10 mm
S6	Strain gauge	10 mm
S7	Strain gauge	10 mm
S8	Strain gauge	10 mm
S9	Strain gauge	10 mm
S10	Strain gauge	10 mm
S11	Strain gauge	10 mm
S12	Strain gauge	10 mm
S13	Strain gauge	10 mm
S14	Strain gauge	10 mm
S15	Strain gauge	10 mm
S16	Strain gauge	10 mm
S17	Strain gauge	10 mm

S18	Strain gauge	10 mm
S19	Strain gauge	10 mm
S20	Strain gauge	10 mm
S21	Strain gauge	10 mm
S22	Strain gauge	10 mm
S23	Strain gauge	10 mm
S24	Strain gauge	10 mm